

Investigations on the transverse phase space at a photo injector for minimized emittance

Dissertation

zur Erlangung des akademischen Grades

doctor rerum naturalium
(Dr. rer. nat.)

im Fach Physik

eingereicht an der

Mathematisch-Naturwissenschaftlichen Fakultät I
der Humboldt-Universität zu Berlin

von

Magister
Velizar Miltchev
geboren am 02.05.1970 in Sofia

Präsident der Humboldt-Universität zu Berlin
Prof. Dr. Christoph Marksches

Dekan der Mathematisch-Naturwissenschaftlichen Fakultät I
Prof. Thomas Buckhout, PhD

Gutachter/innen:

1. Prof. Dr. Eberhard Jaeschke
2. Prof. Dr. Thomas Lohse
3. Prof. Dr. Jörg Rossbach

Tag der mündlichen Prüfung: 02.03.2006

Abstract

Radio frequency photoinjectors are electron sources able to generate beams of extremely high brightness, which are applicable to linac driven Free Electron Lasers (FEL). Because of the high phase space density, the dynamics of the electron beam is dominated by space charge interactions between the particles. This thesis studies the transverse phase space of space charge dominated electron beams produced by the Photo Injector Test Facility in Zeuthen (PITZ). The operation conditions for minimizing the transverse emittance are studied experimentally, theoretically and in simulations. The influence of the longitudinal profile of the driving UV laser pulse on the transverse emittance is investigated. Emphasis is placed on the experimental study of the emittance as a function of different machine parameters like the laser beam spot size, the amplitude of the focusing magnetic field, the rf phase and the electron bunch charge. First investigations on the thermal emittance for Cs₂Te photocathodes under rf operating conditions are presented. Measurements of the thermal emittance scaling with the photocathode laser spot size are analyzed. The significance of the applied rf field in the emittance formation process is discussed.

Zusammenfassung

Hochfrequenz-Photoinjektoren sind Quellen, mit denen leuchtstarke Elektronenstrahlen generiert werden können, wie sie in von Linearbeschleunigern gespeisten Frei-Elektronen-Lasern (FEL) zur Anwendung kommen. Aufgrund der hohen Phasenraumdichte der Elektronenstrahlen wird deren Dynamik von Raumladungseffekten zwischen den Teilchen dominiert. Diese Arbeit beschäftigt sich mit dem Phasenraum der von Raumladungseffekten dominierten Elektronenstrahlen, wie sie am Photo-Injektor Teststand in Zeuthen (PITZ) produziert werden. Betriebsbedingungen, die zur Minimierung der transversalen Emittanz führen, werden experimentell, theoretisch und mittels Simulationen ermittelt. Der Einfluss des longitudinalen Profils des Photokathoden-Laserpulses auf die transversale Emittanz wird studiert. Der Schwerpunkt wird dabei auf experimentelle Studien der Emittanz als Funktion verschiedener Maschinenparameter gelegt, wie z. B. den Durchmesser des Laserstrahles auf der Photokathode, der Amplitude des fokussierenden Magnetfeldes, der Phase des Hochfrequenzfeldes und der Ladung des Elektronenpaketes. Erste Untersuchungen zur thermischen Emittanz von Cs₂Te-Photokathoden unter HF-Bedingungen werden vorgestellt und Messungen der Abhängigkeit der thermischen Emittanz vom Strahldurchmesser

des Photokathodenlasers analysiert. Der Einfluss des verwendeten Hochfrequenzfeldes auf die Emittanzentwicklung wird diskutiert.

Contents

Introduction	9
1 The Photo Injector Test Facility	11
1.1 Overview	11
1.2 Laser system	12
1.3 RF system, rf cavity	14
2 Fundamental concepts of beam dynamics	17
2.1 Phase space, emittance, brightness	17
2.2 Emittance growth and compensation	21
2.2.1 RF emittance	22
2.2.2 Space charge emittance	23
2.2.3 Emittance compensation	24
3 Methods for transverse emittance measurements	27
3.1 Quadrupole scan	27
3.1.1 Quadrupole scan without space charge	27
3.1.2 Quadrupole scan including space charge	29
3.1.3 Example, applicability limitations	31
3.2 Multi slit-Pepper Pot technique	31
3.3 Emittance measurement system at PITZ	34
3.3.1 Accuracy of angular alignment	34
3.3.2 Accuracy of spatial positioning	34
3.3.3 Distance to screen of observation	35
3.3.4 Layout of the masks	36
3.3.4.1 Slit width	36
3.3.4.2 Mask material and thickness	37
3.3.5 Error calculations	38
3.3.5.1 Error in momentum measurement - $\delta\bar{p}_z$	38
3.3.5.2 Errors in beam size measurement - $\delta\sigma_x$	39
3.3.5.3 Errors in beam divergence measurement - $\delta\tilde{\sigma}'_x$	40

4	Thermal emittance measurements	41
4.1	Introduction	41
4.2	Photoemission model for Cs ₂ Te. Emittance calculation	43
4.2.1	Photoemission model	43
4.2.2	Thermal emittance calculation	45
4.3	Operation parameters	47
4.4	Emittance scaling with laser spot size	49
4.5	Thermal emittance dependence on electric rf field	54
4.5.1	Introduction.	54
4.5.2	Measurements of thermal emittance vs. electric field	55
4.5.3	Summary	59
5	Transverse emittance study with flat top temporal laser pulse shape	61
5.1	Impact of the laser pulse temporal profile on the emittance . .	61
5.1.1	Introduction	61
5.1.2	Simulation studies	65
5.1.3	Experimental validation	66
5.2	Simulation study to determine the most sensitive parameters .	67
5.3	Optimisation strategy	70
5.4	Results of the transverse emittance measurements. Comparison with simulations	72
5.4.1	Variation of the transverse laser beam size	72
5.4.1.1	Invariant envelope analysis. Operating diagram	72
5.4.1.2	Measurements and numerical simulations	75
5.4.2	Variation of the focussing solenoid field	79
5.4.2.1	Introduction	79
5.4.2.2	Invariant envelope analysis of the PITZ set up	80
5.4.2.3	Measurement results and numerical simulations with cavity prototype N°2	83
5.4.2.4	Measurement results and numerical simulations with cavity prototype N°1	89
5.4.3	Variation of the rf phase	94
5.4.3.1	Introduction	94
5.4.3.2	Measurement results and numerical simulations	99
5.4.4	Variation of the compensating magnetic field at the photocathode	103
5.4.4.1	Measurements of zero field conditions with the use of He-Ne alignment laser	103
5.4.5	Variation of the electron bunch charge	107
5.4.5.1	Introduction	107

5.4.5.2	Measurements and simulations	109
5.5	Influence of the in-vacuum components	112
Summary		115
Apendix A		117
Magnetic emittance formula		117
Appendix B		119
Operation conditions for the characterization of gun cavity№2		119
Operation conditions for the characterization of gun cavity№1		120
Acknowledgments		129
Erklärung		131

Introduction

The advent of synchrotron radiation[1] in 1947 has revolutionized the research in various areas of fundamental and applied science like solid state physics, material science, biology and medicine. Later on, the use of X-rays has enabled studies of structural and electronic properties of matter on molecular and atomic scale. The driving power behind the progress of the light sources is the increase of their brilliance, which is the figure of merit of many experiments and quantifies the phase space density of photons.

The brilliance of the synchrotron light sources has been growing very rapidly in the last decades. The research community has become accustomed to exponential increases in performance parameters of synchrotron sources since the construction of the first dedicated facilities. By convention the development of synchrotron radiation sources is described in terms of various "generations". The machines, which are nowadays referred to as "first generation light sources", were designed and built for research in the area of high energy physics and started to be used in parallel, for some fraction of the time, as sources of photons for experiments in atomic, molecular and solid state physics.

The importance of the obtained experimental results stimulated the construction of dedicated rings, designed and optimized from the outset as synchrotron light sources. Examples of these "second generation" machines are the BESSY I ring in Berlin and the two National Synchrotron Light Source rings in Brookhaven.

The "third generation" are newer dedicated rings with lower beam emittance and with many long straight sections into which insertion devices can be placed. The synchrotrons of this generation are characterized by the extensive use of undulators as radiation sources and with a further increase of the brilliance by several orders of magnitude. Examples of such third generation rings are BESSY II and the Advanced Light Source in Berkeley. However, there is a fundamental limitation for the lowest beam emittance reachable in a storage ring, which is determined by the equilibrium between quantum excitation that causes individual particles to oscillate transversely and the damp-

ing of the betatron oscillations. This is the reason why the development of the "fourth generation" light sources has oriented itself to "single-pass" machines, where the beam quality is bounded by the thermal emittance of the electron source. The linear accelerator driven Free Electron Lasers (FEL) using the principle of self-amplified spontaneous emission (SASE) appear to be the most promising approach to produce laser-like radiation of extremely high peak brilliance in the order of 10^{33} photons/s/mm²/mrad²/0.1%BW, (to be compared with $\sim 10^{21}$ for third generation undulators). Some facilities of this type were already proposed like LCLS at SLAC (now under construction[2]) and XFEL, which will start at DESY in Hamburg and will be based on superconducting rf technology[3].

The electron beam quality and stability required by the SASE process presents considerable challenges to the linear accelerator community: the electron bunches of the beam must be very short and at the same time have an extremely small transverse emittance. Therefore DESY runs an intensive development program, within the framework of which the Photo Injector Test Facility at Zeuthen (PITZ) was built. The main goal of PITZ is to study the production of minimum transverse emittance electron beams for Free Electron Lasers and future Linear Colliders[4].

This thesis examines the process of transverse emittance characterization and optimization of the PITZ rf gun as an electron source meeting the requirements of VUV-FEL and XFEL. In Chapter 1 the essential systems and components of the PITZ photoinjector are described. In Chapter 2 some important concepts of the beam dynamics are introduced. Chapter 3 is dedicated to the methods for emittance measurement as well as to their applicability limitations. In Chapter 4 the lower emittance limit imposed by the thermal emittance is investigated. The thermal emittance measurements were performed under rf operation conditions for various Cs₂Te cathodes and different accelerating gradients. Measurements of thermal emittance scaling with laser spot rms size are presented and analyzed. The significance of the Schottky effect in the emittance formation is discussed.

The impact of the temporal profile of the UV laser pulse on the emittance was studied in Chapter 5, where measurements and simulations demonstrate that flat top pulses yield about two times smaller emittance than gaussian profile. The development of experimental procedures to determine the optimal gun operating conditions is discussed. A systematic experimental scan of emittance as a function of a wide range of machine parameters (e.g. laser spot rms size, bunch charge, focusing field etc.) is presented and analyzed from the point of view of theoretical models and multiparticle simulations. In the closing part of the thesis, the ways to further improve the beam quality and produce ultra low emittance bunches are outlined.

Chapter 1

The Photo Injector Test Facility

1.1 Overview

The Photo Injector Test Facility at Zeuthen (PITZ) was build for the development of electron sources with minimized transverse emittance like they are required for the successful operation of Free Electron Lasers and future linear colliders[5]. The photoinjector consists of one and a half cell L-band RF gun with a Cs_2Te photo-cathode, a solenoid system for compensating space charge induced emittance growth, a photo-cathode laser system capable to generate long pulse trains with variable temporal and spatial micro pulse shape and an extensive diagnostics section. A schematic of the set up is shown in Fig. 1.1. The UV laser beam is fed through the laser input

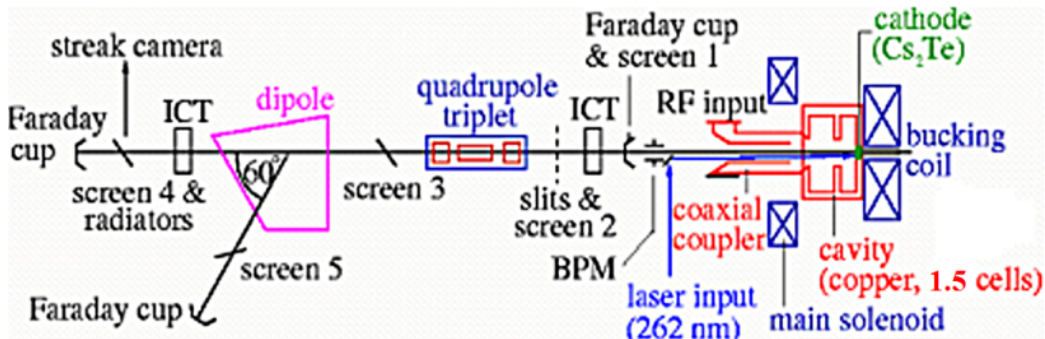


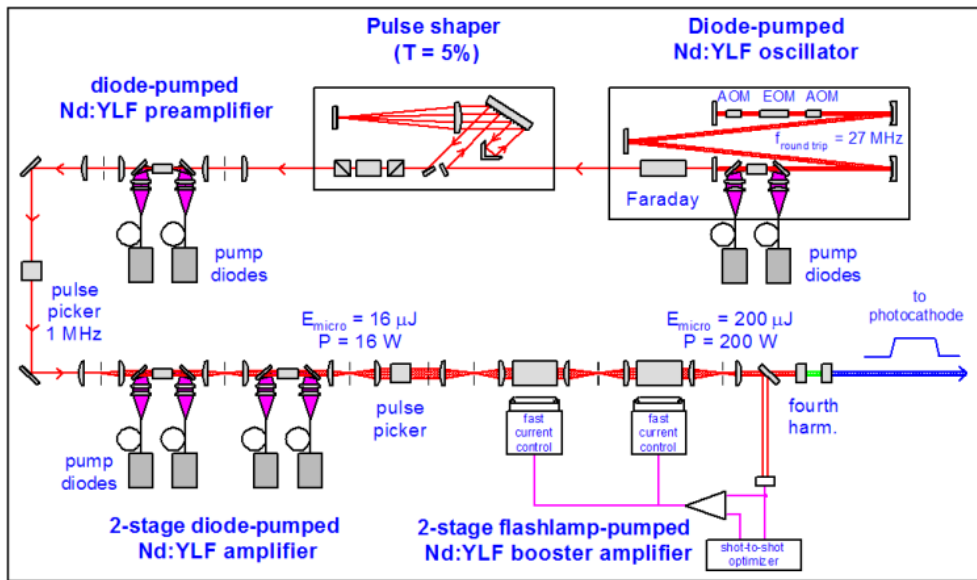
Figure 1.1: Schematic layout of PITZ.

port and then, by a mirror located inside the vacuum tube, directed towards the cathode. As the laser illuminates the Cs_2Te photocathode it provokes

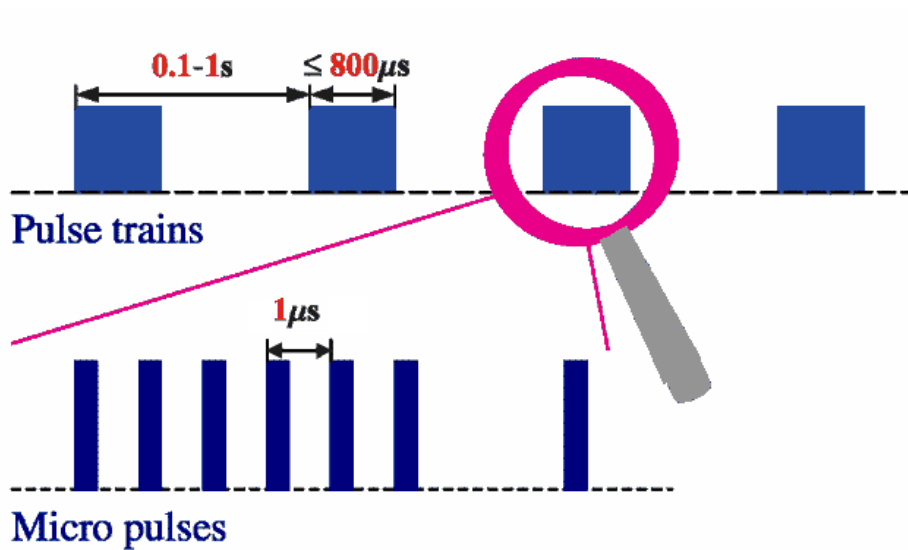
photoemission. The emitted electrons are instantaneously accelerated in the rf cavity, thus forming an electron beam. The rf power for the acceleration is produced by a 5MW klystron and transmitted through a waveguide system and a coaxial rf coupler into the cavity. During the acceleration the beam experiences a focusing from the magnetic field generated by the main solenoid. The bucking coil compensates the magnetic field at the photocathode position ($z=0$ m) in order to minimize the residual angular momentum of the photoelectrons. The Faraday cup and integrated current transformer (ICT) are used for bunch charge measurements. The emittance measurement system (EMSY), situated at $z=1.618$ m downstream of the photocathode, consists of two sets of masks for sampling the trace space distribution in both transverse directions and a screen for beam size measurements. After a drift of $L=1.01$ m from EMSY follows a screen (denoted as screen 3 in Fig. 1.1), which is used for observation of the beamlet profiles produced by a slit or pepper pot mask. The dipole spectrometer is used for momentum and momentum spread measurements as well as in the system for longitudinal phase space reconstruction[6, 7].

1.2 Laser system

The photons necessary to initiate the photoemission are produced by a laser system, which has been developed at Max-Born-Institute [8, 9]. The laser system consists of a Nd:YLF oscillator (see Fig. 1.2 (a)), longitudinal pulse shaper, numerous amplifier stages and conversion crystals. The laser emits photons in portions, so-called micropulses, which have duration of some picoseconds (see Fig. 1.2 (b)). The micropulses are being generated in groups - pulse trains of tuneable length of up to $800 \mu\text{s}$ and repetition rate in the range 1-10 Hz. Within the pulse train the individual micropulses are separated by a time interval of $1 \mu\text{s}$. The initial longitudinal distribution of the micropulses is gaussian of $\sigma_t \simeq 3$ ps. The pulse shaper transforms the longitudinal distribution to flat top of 18-23 ps FWHM, with rise/fall time corresponding to σ_t . The pulse shaping is accomplished through a frequency domain manipulation using diffraction gratings[10]. Since the photocathode material (Cs_2Te) is a semiconductor with a band gap of 3.3 eV, the required output wavelength is in the UV range. Therefore with the help of frequency conversion crystals the fourth harmonic (262 nm) of the fundamental 1047 nm is generated. The output energy of the UV micropulse can reach values up to $20 \mu\text{J}$. Finally by the usage of an optical beamline of more than 20 m total length the laser beam is imaged onto the photocathode.



(a) Sketch of the laser system.



(b) Pulse trains and micropulses.

Figure 1.2: Schematic layout of the PITZ laser system and time structure of the laser output.

1.3 RF system, rf cavity

For acceleration of the emitted photoelectrons to a final energy of several MeV one needs an electric field of high amplitude in the rf cavity (see Fig. 1.3), which resonates in a $TM_{010,\pi}$ mode at a frequency of 1.3 GHz. Since the relation between the peak electric field E_0 and the peak forwarded power P_f in the gun is given by[11]:

$$E_0[MVm^{-1}] \simeq 23.336\sqrt{P_f[MW]} \quad (1.1)$$

it follows that in order to transmit sufficient energy of the standing electro-

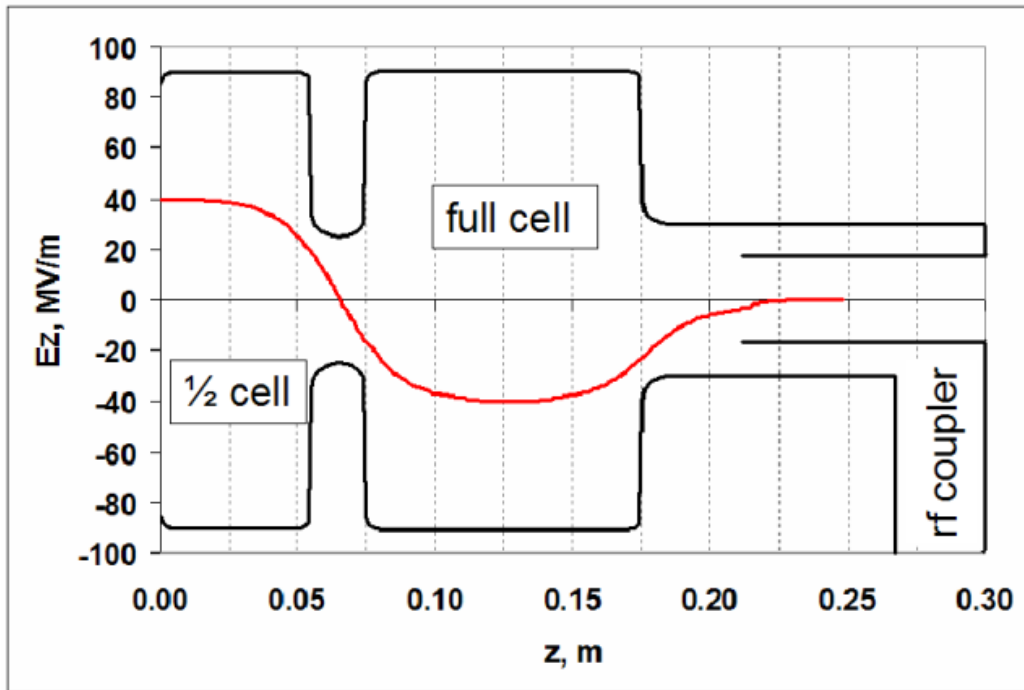


Figure 1.3: Sketch of rf cavity with coaxial rf coupler and longitudinal distribution of electric field amplitude.

magnetic wave in the cavity to the electron bunch over a distance of about 0.18 m, a peak power in the order of 3-4 MW is required. On the other hand a high average rf power is needed as well, so that the high accelerating gradient is kept constant during the entire laser pulse train of some hundreds of microseconds. The necessary high power microwave is produced by a 5 MW klystron, with thermo cathode. After being accelerated by the applied 120 kV DC voltage between cathode and anode, the thermo electrons initially drift

with constant velocity. When they traverse a pair of closely spaced grids, their velocity is modulated by a sinusoidal 1.3 GHz signal. The velocity modulation of the beam forms bunches because of the modified momentum distribution among the electrons. The result is a current density modulated beam that varies at the same rate as the original 1.3 GHz frequency. This alternating current is fed into a five cell klystron resonator tube, where it induces an electromagnetic wave, which then by waveguides is forwarded towards the gun. The wave is coupled from the rectangular waveguide via an rf window and through a symmetric input coupler into the cavity [12]. The forwarded rf power dissipates in the cavity due to the finite conductivity of the copper walls and thus increases the cavity temperature. Because of thermal expansion, the temperature changes the radius of the cavity and hence the resonant frequency. An increase of the temperature of the gun will decrease the resonant frequency by about 22 kHz/°C. Therefore the gun temperature is being stabilized by a dedicated water cooling system so that it fluctuates not more than 0.05 °C peak-to-peak [11]. Assuming operation with 3 MW peak power and duty cycle of 1% it follows that for keeping the gun frequency constant an average power of 30 kW has to be removed by the water cooling system.

Two gun cavities of the same type were successively installed and characterized at PITZ. The first cavity is referred to as cavity prototype №2 because it was the second rf gun cavity produced at DESY. After it has been characterized at PITZ, this cavity has been installed at the VUV-FEL at TTF2 in Hamburg and went smoothly into operation [13]. After moving the prototype №2 to Hamburg, another gun cavity, prototype №1, was installed at PITZ. The measurements performed with these two cavities together with electron beam dynamics simulations will be summarized in the next Chapters of the thesis.

Chapter 2

Fundamental concepts of beam dynamics

2.1 Phase space, emittance, brightness

A beam consisting of N particles can be represented by a set of N points in the 6-dimensional phase space. The distribution of the particles in phase space is described by a phase space density $f_6(\vec{r}, \vec{p})$, defined in such a way that:

$$dN = f_6(\vec{r}, \vec{p})dV_6 \quad (2.1)$$

Here dN denotes the number of particles in the infinitesimal phase space volume dV_6 . One can interpret the phase space density as a probability density distribution in the phase space. Neglecting the coupling between the three coordinates of a particle it is possible to split the 6-dimensional phase space into a 2-dimensional longitudinal phase space $\{z, p_z\}$ and two 2-dimensional transverse phase spaces $\{x, p_x\}$, $\{y, p_y\}$. When a particle propagates along the Z direction one denotes $f_4(x, p_x, y, p_y)$ as the distribution function in the 4-dimensional transverse phase space. In the paraxial approximation where p_z is much larger than p_x and p_y the distribution function is described as $f_4(x, x', y, y')$, with $x' = p_x/p_z$ and $y' = p_y/p_z$ denoting the horizontal and vertical divergence angles. By splitting the 4-dimensional transverse phase space $\{x, x', y, y'\}$ into two 2-dimensional ones $\{x, x'\}$ and $\{y, y'\}$, distributions for each of the spaces: $f_2(x, x')$ and $f_2(y, y')$ are defined. Here $f_2(x, x')$ is given by:

$$f_2(x, x') = \frac{1}{\int dV_6 f_6(\vec{r}, \vec{p})} \int dz \int dp_z \int dy \int dy' f_6(\vec{r}, \vec{p}) \quad (2.2)$$

and an analogous equation exists for $f_2(y, y')$. The area A_x occupied by the particles in the $\{x, x'\}$ phase space plane[14]

$$A_x = \int \int dx dx' = \frac{1}{p} \int \int dx dp_x \quad (2.3)$$

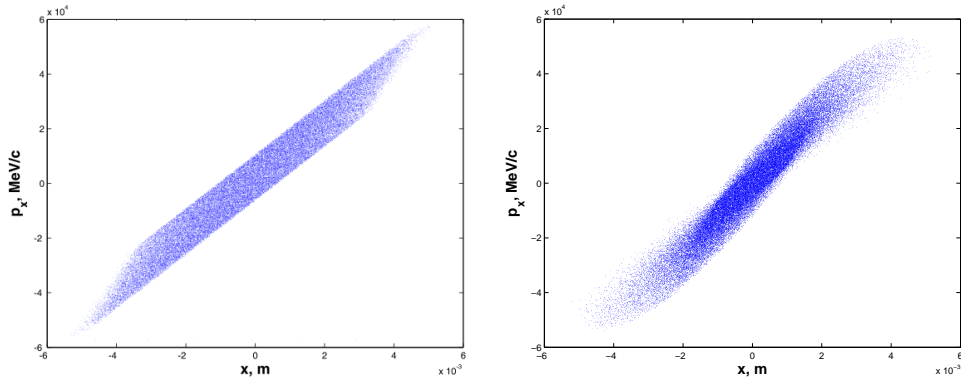
is related to the emittance ϵ_x of the beam. There is no unique definition of emittance. Some authors define the emittance as the phase space area:

$$\epsilon_x = A_x \quad (2.4)$$

Often the emittance is defined as the phase space area A_x divided by π :

$$\epsilon_x = \frac{A_x}{\pi} \quad (2.5)$$

The definition of transverse emittance described with Eqs. 2.4 and 2.5 does not distinguish between beams with equal transverse phase space areas A_x , but with different transverse phase space area shapes. The shape of the transverse phase space could be distorted e.g. due to space charge interactions or nonlinear forces in the focusing system. Such a distortion is illustrated in Fig. 2.1. It is clear from this figure that the beam transverse properties are



(a) Phase space without space charge interactions.

(b) Phase space with included space charge forces.

Figure 2.1: ASTRA[15] simulations to illustrate phase space distortion due to space charge force.

different for the two cases, despite of the fact that the transverse space area A_x remains the same. There is another definition for the beam emittance, which gives more complete description of the transverse phase space: using

the moments of the particle distribution in transverse phase space (e.g. in $\{x, x'\}$ plane) one can define an rms emittance $\epsilon_{x,rms}$ by

$$\epsilon_{x,rms} = \sqrt{\langle x^2 \rangle \langle x'^2 \rangle - \langle xx' \rangle^2} \quad (2.6)$$

where $\langle x^2 \rangle$, $\langle x'^2 \rangle$, $\langle xx' \rangle$ are given by:

$$\langle x^2 \rangle = \int \int dx dx' f_2(x, x') x^2 \quad (2.7)$$

$$\langle x'^2 \rangle = \int \int dx dx' f_2(x, x') x'^2 \quad (2.8)$$

$$\langle xx' \rangle = \int \int dx dx' f_2(x, x') xx' \quad (2.9)$$

In the emittance definition above one assumes that $\langle x \rangle = 0$ and $\langle x' \rangle = 0$. Formally the rms emittance defined by Eq. 2.6 can be expressed through the determinant of the so-called sigma matrix:

$$\Sigma_x = \begin{pmatrix} \langle xx \rangle & \langle xx' \rangle \\ \langle xx' \rangle & \langle x'x' \rangle \end{pmatrix} \quad (2.10)$$

The rms emittance is equal to:

$$\epsilon_{x,rms} = \sqrt{\det \Sigma_x} \quad (2.11)$$

The rms emittance provides the desired quantitative description of the beam quality. Thus in the examples illustrated with Fig. 2.1, the rms emittance is higher in the case of a distortion of the transverse phase space (right part). Emittance defined by Eq. 2.6 gives more weight to the particles in the outer region of the transverse space area than to those at the beam center. Therefore one could significantly improve the rms emittance by removing such particles, while the beam intensity remains without considerable change.

The unit of the transverse emittance is [m·rad]. But as the typical sizes and divergence angles are in the order of mm and mrad, it is more convenient to use the unit [mm·mrad]. When the transverse emittance is defined according to Eq.2.5, the factor π is often included within the units e.g. $\epsilon_x = 10 \pi \text{mm} \cdot \text{mrad}$.

One defines the emittance of each degree of freedom: the horizontal emittance $\epsilon_{x,rms}$, the vertical emittance $\epsilon_{y,rms}$ and the longitudinal emittance $\epsilon_{z,rms}$. For axially symmetric beams it is sufficient to consider only one of the two transverse phase planes $\{x, x'\}$ and $\{y, y'\}$. Respectively, it is enough to determine either $\epsilon_{x,rms}$ or $\epsilon_{y,rms}$. In many cases the beams have two planes of symmetry

(asymmetric beams). Then one needs to determine the transverse emittance for both transverse directions and even to consider the 4D emittance:

$$\epsilon_{4d} = \sqrt{\det \Sigma_{4d}} \quad (2.12)$$

with the 4-dimensional sigma matrix given by:

$$\Sigma_{4d} = \begin{pmatrix} \langle xx \rangle & \langle xx' \rangle & \langle xy \rangle & \langle xy' \rangle \\ \langle xx' \rangle & \langle x'x' \rangle & \langle yx' \rangle & \langle x'y' \rangle \\ \langle xy \rangle & \langle yx' \rangle & \langle yy \rangle & \langle yy' \rangle \\ \langle xy' \rangle & \langle y'x' \rangle & \langle yy' \rangle & \langle y'y' \rangle \end{pmatrix} \quad (2.13)$$

In cases when the coupling between both transverse directions is negligible then Eq. 2.12 transforms to [16]:

$$\epsilon_{4d} = \epsilon_{x,rms} \epsilon_{y,rms} \quad (2.14)$$

The emittance defined by the formulae Eq. 2.5 and Eq. 2.6 depends on the momentum of the particles since the slope $x' = p_x/p_z$ is inversely proportional to the momentum p_z . Hence as the beam is accelerated, the area in the transverse phase space decreases. Therefore, in order to compare beams of different energies, one defines the so-called normalized rms emittance:

$$\epsilon_{nx,rms} = \beta \gamma \epsilon_{x,rms} \quad (2.15)$$

Here $\beta = v/c$ and $\gamma = 1/\sqrt{1 - \beta^2}$ are the usual relativistic parameters. The normalized emittance is a conserved quantity with respect to the changes in p_z . From the point of view of the practical applications, it is important to know the total beam current corresponding to a given emittance. Therefore a quantity known as the brightness B of a beam is defined[16]:

$$B = \frac{2I}{\epsilon_{x,rms} \epsilon_{y,rms}} \quad (2.16)$$

Here I denotes the beam current. Since the beam brightness depends on the momentum, one has also to define a normalized brightness B_n . The normalized brightness is given by:

$$B_n = \frac{B}{\beta^2 \gamma^2} \quad (2.17)$$

So defined, B_n is an invariant with respect to different energies. Often one considers a quantity called slice emittance. The slice emittance

is the transverse emittance of the beam particles confined in a thin longitudinal slice of the beam: $[z, z + \delta z]$. It is defined again by Eq. 2.6, but this time the integration over z in Eq. 2.2 is replaced by multiplication by δz . As opposed to the slice emittance, the emittance obtained by integration in Eq. 2.2 over the entire bunch length is called projected emittance, since it characterizes the common projection of the phase spaces of all slices. Due to space charge interactions, the projected beam emittance can be significantly larger than the emittance of a single bunch slice, as illustrated in Fig. 5.3 b (see discussion in Chapter 5).

Another important photoinjector characteristic is the thermal emittance. The transverse thermal emittance of the electron beam depends on the transverse momenta of the emitted photoelectrons and the laser rms spot size at the cathode. It is essentially independent of charge and imposes the lower emittance limit achievable directly from the source. In the case of a photocathode gun with semiconductor photocathode the thermal emittance is determined by the laser spot size and the mean kinetic energy of the emitted photoelectrons, which is a function of the driving laser photon energy, the photocathode material band gap and electron affinity (see Chapter 4 for details on thermal emittance calculation and experimental data).

In order to describe the propagation of the beam particles along the beamline one applies the formalism of transfer matrices. The action of each accelerator component (e.g. drift, solenoid, quadrupole etc.) is described to a first order by a square transfer matrix R . The transfer matrix gives a mapping of the initial phase space coordinates to the final state:

$$\begin{pmatrix} x \\ x' \\ y \\ y' \\ \delta z \\ \delta p_z \end{pmatrix}_1 = R \cdot \begin{pmatrix} x \\ x' \\ y \\ y' \\ \delta z \\ \delta p_z \end{pmatrix}_0 \quad (2.18)$$

This formalism can be applied to all or part of the phase space coordinates as well as for transforming the moments of the phase space distribution defined with Eqs. 2.7-2.9 and Eq. 2.10:

$$\Sigma_x(1) = R_x \cdot \Sigma_x(0) \cdot R_x^T \quad (2.19)$$

2.2 Emittance growth and compensation

The evolution of a physical system consisting of N particles could be regarded as a mapping of the 6-dimensional phase space onto itself [17]. If a

Hamiltonian H could be defined and if a system of non-interacting particles is considered, one can show that there are quantities, which are left invariant by the mapping, such as the phase space volume V_6 and the local phase space density $f_6(\vec{r}, \vec{p})$ [18]. This result is termed Liouville's theorem, which strictly speaking applies only to the 6-dimensional phase space. One has to point out, that even if the 6-dimensional phase space volume remains constant, in general, the shape does not. Liouville's theorem can also be applied to the 2-dimensional transverse phase space. Consider the area A_x , which is a projection of the phase space volume onto the $\{x, x'\}$ plane. A_x is defined by the integral 2.3. If there is no coupling between the motions along the three coordinate axes and there is no change in momentum, the integral remains constant. Respectively, the area A_x and the emittance are also conserved.

2.2.1 RF emittance

However in many practical cases the Liouville's theorem does not hold and one observes an increasing transverse emittance. This emittance growth is mainly introduced by two mechanisms: transverse focusing kick from rf field due to field termination at the gun exit and by space charge interactions. An estimation for rf emittance growth can be derived by representing the longitudinal rf field in the form [19, 20]:

$$E_z(z, t) = E(z) \sin(\omega t + \phi_0) \cos(kz) \quad (2.20)$$

where ϕ_0 is the launching rf phase, $\omega = 2\pi\nu$ is the rf angular frequency, k is the rf wavenumber and $E(z)$ is a function introduced to describe the termination of rf field at gun exit z_{exit} , which has the form of Heaviside step function:

$$E(z) = E_0(1 - \Theta(z - z_{exit})) \quad (2.21)$$

Maxwells equations yield for the radial electric field E_r and for the azimuthal magnetic field B_θ :

$$E_r(z, t) = -\frac{r}{2} \frac{\partial E_z(z, t)}{\partial z} \quad cB_\theta(z, t) = \frac{r}{2c} \frac{\partial E_z(z, t)}{\partial t} \quad (2.22)$$

$$F_r = e(E_r - \beta c B_\theta) \quad (2.23)$$

An expression for the radial Lorenz force can be obtained by differentiation of Eq. 2.20 and replacement in Eq. 2.23. The integration of F_r with respect to the time yields the transverse momentum induced by the rf field:

$$p_x = m_e c \cdot \alpha \cdot k \cdot x \cdot \sin(\phi_{exit}) \quad (2.24)$$

where ϕ_{exit} denotes the rf phase at the cavity exit and $\alpha = eE_0/2mc^2k$ gives the normalized rf field strength. By performing the integrals for $\langle p_x^2 \rangle$ and $\langle p_x \cdot x \rangle$ and plugging the results into Eq. 2.6 one obtains the rf emittance for gaussian and flat top longitudinal distribution respectively[19]:

$$\epsilon_{nx,rms}^{rf} = \frac{\alpha k^3 \sigma_x^2 \sigma_z^2}{\sqrt{2}} \quad \epsilon_{nx,rms}^{rf} = \frac{\alpha k^3 a^2 L^2}{4\sqrt{6!}} \quad (2.25)$$

In the first relation σ_x, σ_z are the transverse and longitudinal bunch size for the gaussian case. In the second expression a and L denote respectively the radius and the length of a cylindrical bunch.

2.2.2 Space charge emittance

At high space charge densities the self field interactions between the particles of the electron beam become the major contribution to transverse emittance. In general the self fields distort the phase space distribution and introduce couplings between motions along the coordinate axes. Due to the finite bunch length the differences in space charge forces between beam edges and core start to play a role in the formation of the projected emittance. The emittance growth caused by space charge interactions is of great importance at low energies, since as the beam accelerates the space charge forces are diminished by the relativistic effects. An estimate for the emittance growth induced by space charge forces can be given following the arguments in [19], where the space charge force is represented in the form:

$$\vec{F}_{sc}(\gamma, \vec{r}) \approx \frac{e}{\gamma^2} \vec{E}_{sc}(\vec{r}) \equiv \frac{e}{\gamma^2} \frac{n_0}{4\pi\epsilon_0} \vec{\Upsilon}(\vec{r}) \quad (2.26)$$

with $n_0 = \int \rho(x, y, 0) dx dy$ denoting the line density in the center of the bunch and $\vec{\Upsilon}$ is a normalized space charge field. Eq. 2.26 can be integrated considering that near the cathode surface:

$$\frac{d\gamma}{dz} = \frac{eE_0}{m_e c^2} \sin(\phi_0) \Rightarrow dz = \frac{d\gamma \cdot m_e c^2}{eE_0 \sin(\phi_0)} \Rightarrow dt = \frac{d\gamma}{c\beta} \frac{m_e c^2}{eE_0 \sin(\phi_0)} \quad (2.27)$$

and since at the final state of acceleration $\gamma_{final} \gg 1$ it follows:

$$\vec{p} = \int \vec{F}_{sc} dt = \frac{m_e c \vec{E}_{sc}}{E_0 \sin(\phi_0)} \int_1^{\gamma_{final}} \frac{d\gamma}{\gamma^2 \sqrt{1 - \frac{1}{\gamma^2}}} \approx \frac{\pi}{2} \frac{m_e c \vec{E}_{sc}}{E_0 \sin(\phi_0)} \quad (2.28)$$

Calculating with the help of Eq. 2.26 and Eq. 2.28 the integrals for $\langle p_x^2 \rangle$ and $\langle p_x \cdot x \rangle$ one obtains the following expression for the normalized transverse emittance due to space charge:

$$\epsilon_{nx,rms}^{sc} = \frac{\pi}{4} \frac{1}{\alpha k} \frac{1}{\sin \phi_0} \frac{I}{I_A} \mu_x(A) \quad (2.29)$$

where $I_A = 4\pi\epsilon_0 m_e c^3 / e = 17 \text{ kA}$, $A = \sigma_x / \sigma_z$ is the bunch aspect ratio in the laboratory frame and:

$$\mu_x = \sqrt{\langle \Upsilon_x^2 \rangle \langle x^2 \rangle - \langle \Upsilon_x x \rangle^2} \quad (2.30)$$

is a geometric form factor depending on the form of the charge distribution and bunch aspect ratio. An approximate numerical representation of μ_x for gaussian bunch can be given [19]:

$$\mu_x \approx \frac{1}{3A + 5} \quad (2.31)$$

2.2.3 Emittance compensation

From the result in Eq. 2.29 it follows that the space charge emittance growth can be reduced by launching at ϕ_0 close to $\pi/2$ as well as by increasing the accelerating field gradient E_0 .

However if one considers the emittance as originating from the superposition of the phase spaces of all longitudinal bunch slices, then it would be possible to apply another mechanism to counteract the influence of space charge forces. In this so called emittance compensation technique introduced by Carlsten[21], one tries to correct the correlation between $\{x, x'\}$ and the longitudinal position inside the bunch. Since the space charge forces are stronger at the bunch core and weaker at the head and the tail, the phase space angle $\tan^{-1}(x'/x)$ is different for each longitudinal slice. Subsequently the projected emittance increases. By placing a focusing lens F (e.g. a solenoid) in the vicinity of the rf gun and by setting a proper focussing current one can compensate this spread of phase space angles. In the PITZ set up (see Fig. 1.1) the focusing solenoid is located at a distance of about 0.27 m downstream the photocathode.

The principle of the emittance compensation, illustrated in Fig. 2.2 and Fig. 2.3, can be understood by representing the action of the space charge forces as a defocusing lens 'SC' of a given focal length, different for each of the particles A and B. One can assign to the initial states of A and B (Fig. 2.3 a) the phase space vectors \vec{A}_0 and \vec{B}_0 . Then the entire emittance compensation sequence in Fig. 2.3 can be described with the following transformations:

$$\vec{A}_{final} = L_2 \cdot SC_{A,2} \cdot F \cdot L_1 \cdot SC_{A,1} \cdot \vec{A}_0 \quad (2.32)$$

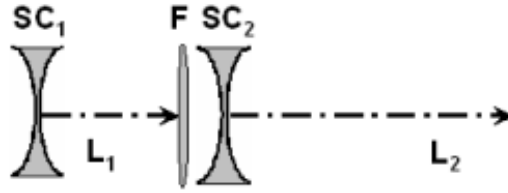


Figure 2.2: Schematic of the emittance compensation set up. The action of the space charge forces is represented with the defocusing lenses SC_1 and SC_2 . The emittance compensation is achieved at the end of the second drift.

$$\vec{B}_{final} = L_2 \cdot SC_{B,2} \cdot F \cdot L_1 \cdot SC_{B,1} \cdot \vec{B}_0 \quad (2.33)$$

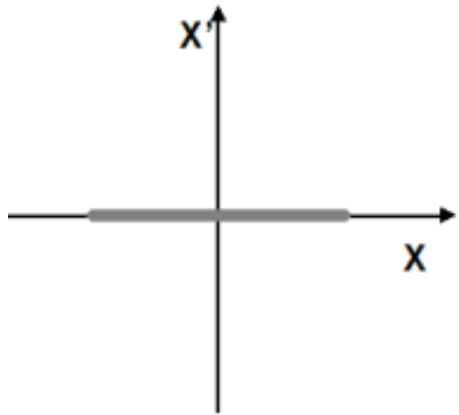
Here \vec{A}_{final} , \vec{B}_{final} are the phase space vectors corresponding to the end of the second drift. The transfer matrices L_1, L_2 describe the drift space before and after the focusing lens F respectively. The transfer matrices of the 'space charge' defocusing lenses, before and after F , are denoted with SC_1, SC_2 and they are different for A and B.

The emittance compensation condition corresponds to vanishing phase space area (see Fig. 2.3 d) and hence:

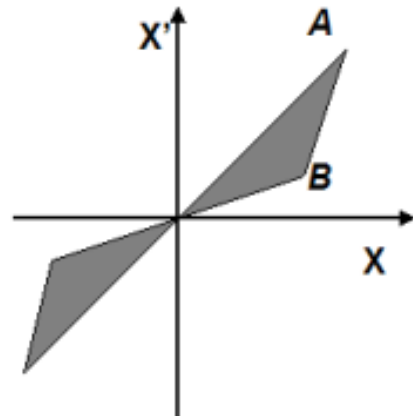
$$\vec{A}_{final} \times \vec{B}_{final} = 0 \quad (2.34)$$

Assuming that all transfer matrices $\{L\}$ and $\{SC\}$ are known then Eq. 2.34 determines the necessary focal length of the lens F (resp. solenoid current) needed to achieve emittance compensation at the end of the second drift.

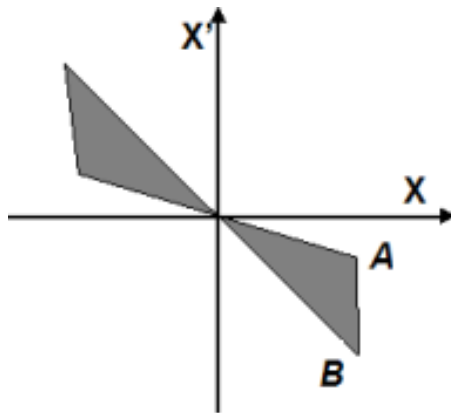
One has to note that emittance compensation acts on the projection of the 6D phase space onto 2D transverse phase space planes, but it does not change the full phase space volume.



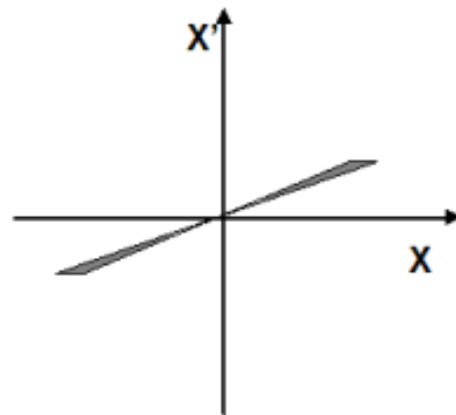
(a) Initial phase space with a vanishing emittance.



(b) Phase-space after drift before the focusing lens, showing increased phase space area due to different transverse momenta between A and B.



(c) Phase space immediately after the lens showing the rotation due to the lens.



(d) Phase space after a drift behind the lens, showing the phase space area reduction due to the different transverse momenta of A and B.

Figure 2.3: A sequence of transverse phase space plots showing growth of the projected transverse emittance due to space charge forces and its subsequent reduction due to the emittance compensation technique[21].

Chapter 3

Methods for transverse emittance measurements

3.1 Quadrupole scan

The methods for emittance measurement can be classified into two general categories [20]:

- Methods which sample the initial phase space distribution and allow a drifting of the beam to convert the relevant rms angular spreads into measurable transverse size quantities.
- Methods which presume that linear optics can be applied to the entire beam. Spot size information is taken at different locations or at one single location under different focusing conditions.

Into the latter category fall the multiple screen method as well as the quadrupole scan technique.

3.1.1 Quadrupole scan without space charge

Often the only available tool for transverse beam diagnostics is a phosphorescent screen inserted into the electron beam that emits optical radiation, which can be viewed by a CCD camera. By calculating the first and second moments of the observed light intensity distribution one obtains electron beams centroid position and rms size σ . From Eq. 2.10 one notes that σ^2 is by definition equal to the matrix element Σ_{11} . With account of Eq. 2.11, it follows that one has to determine also the other two matrix elements: Σ_{12} and Σ_{22} in order to find the emittance. From Eq. 2.19 it follows that after a

propagation from the screen position, denoted as '0', to position '1' further downstream, over a total length l_1 , the matrix element Σ_{11} transforms as:

$$\Sigma_{11}(1) = L_{1,11}^2 \Sigma_{11}(0) + 2L_{1,11}L_{1,12} \Sigma_{12}(0) + L_{1,12}^2 \Sigma_{22}(0) \quad (3.1)$$

where the matrix L_1 represents the drift of length l_1 and the optical elements (e.g. quadrupoles etc.) between '0' and '1'. If the beam size can be measured at screens corresponding to drift lengths $l_1, l_2..l_n$ described by the transfer matrices $L_1, L_2..L_n$, then the Eq. 3.1 can be rewritten in the following general form:

$$\begin{pmatrix} \Sigma_{11}(1) \\ \Sigma_{11}(2) \\ \dots \\ \Sigma_{11}(n) \end{pmatrix} = \begin{pmatrix} L_{1,11}^2 & 2L_{1,11}L_{1,12} & L_{1,12}^2 \\ L_{2,11}^2 & 2L_{2,11}L_{2,12} & L_{2,12}^2 \\ \dots & \dots & \dots \\ L_{n,11}^2 & 2L_{n,11}L_{n,12} & L_{n,12}^2 \end{pmatrix} \begin{pmatrix} \Sigma_{11}(0) \\ \Sigma_{12}(0) \\ \Sigma_{22}(0) \end{pmatrix} \quad (3.2)$$

Since $\Sigma_{11}(0) = \sigma^2(0)$ corresponds to the rms beam size at the first screen, which has been already measured, for $n=2$ the system above has exact solutions¹ for the unknown $\Sigma_{12}(0), \Sigma_{22}(0)$. Thus with three beam size measurements at different locations one can determine the transverse emittance at the position of the first screen (position '0'). The above described method is termed the 'three screen' method. In the cases when $n \geq 3$ (the 'multiple screen' case), the system 3.2 is over determined and one looks for a solution in χ^2 or in least squares sense.

The quadrupole scan is a widely used method for emittance measurement. In fact it is a modification of the multiple screen method. The usage of the multiple screen method requires at least three screens situated at appropriate locations. The basic set-up for a quadrupole scan, as it is shown in Fig. 3.1, consists of a single quadrupole and a screen situated at a distance L_d after the quadrupole. One varies the strength of the quadrupole and measures the transverse size of the beam as a function of the quadrupole strength. These measurements are equivalent to the measurements at different locations discussed above, but the matrices $\{L_i\}$ this time correspond to various quadrupole currents, while the drift distance to the screen for beam size measurement is fixed. Another difference to the multiple screen method is that none of the elements $\Sigma_{ij}(0)$ is known, because position '0' corresponds to the entrance of the quadrupole magnet. It is important to note that both the quadrupole scan and multiple screen method yield non-normalized rms transverse emittances after solving the system: 3.2 for the unknown $\Sigma_{ij}(0)$. The normalized rms emittance is given by:

$$\epsilon_{n,rms} = \beta\gamma\sqrt{\det \Sigma(0)} \quad (3.3)$$

¹Here one assumes linearly independent equations.

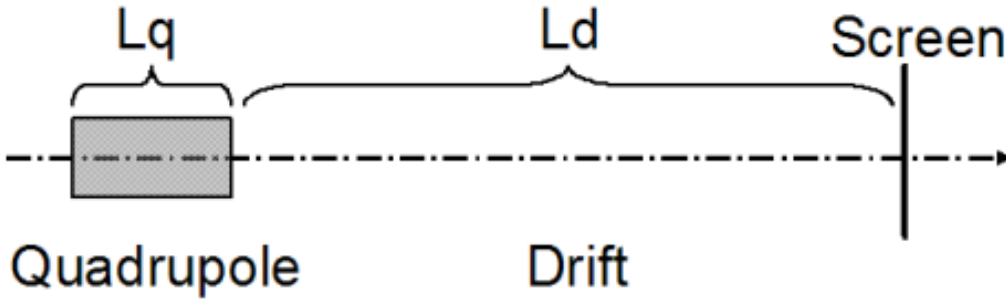


Figure 3.1: The sketch shows a typical quadrupole scan set up.

In the considerations above it was assumed that beam transverse phase space transformation from quadrupole entrance downstream to the screen can be described solely by the product of transfer matrices of the quadrupole Q and the drift L [22]:

$$LQ = \begin{pmatrix} 1 & L_d & 0 & 0 \\ 0 & 1 & 0 & 0 \\ 0 & 0 & 1 & L_d \\ 0 & 0 & 0 & 1 \end{pmatrix} \begin{pmatrix} \cos \sqrt{k}L_q & \frac{\sin \sqrt{k}L_q}{\sqrt{k}} & 0 & 0 \\ -\sqrt{k} \sin \sqrt{k}L_q & \cos \sqrt{k}L_q & 0 & 0 \\ 0 & 0 & \cosh \sqrt{k}L_q & \frac{\sinh \sqrt{k}L_q}{\sqrt{k}} \\ 0 & 0 & \sqrt{k} \sinh \sqrt{k}L_q & \cosh \sqrt{k}L_q \end{pmatrix} \quad (3.4)$$

Here L_q is the effective length of the quadrupole magnet, L_d is the drift length between the quadrupole exit and the screen, k is the focusing strength of the quadrupole, which is determined by the current through the magnet. A quadrupole scan consists on n beam size measurements, each of them at different quadrupole current. Thus Eq. 3.1 transforms into:

$$\begin{pmatrix} \Sigma_{11}(1) \\ \Sigma_{11}(2) \\ \dots \\ \Sigma_{11}(n) \end{pmatrix} = \begin{pmatrix} (LQ)_{1,11}^2 & 2(LQ)_{1,11}(LQ)_{1,12} & (LQ)_{1,12}^2 \\ (LQ)_{2,11}^2 & 2(LQ)_{2,11}(LQ)_{2,12} & (LQ)_{2,12}^2 \\ \dots & \dots & \dots \\ (LQ)_{n,11}^2 & 2(LQ)_{n,11}(LQ)_{n,12} & (LQ)_{n,12}^2 \end{pmatrix} \begin{pmatrix} \Sigma_{11}(0) \\ \Sigma_{12}(0) \\ \Sigma_{22}(0) \end{pmatrix} \quad (3.5)$$

3.1.2 Quadrupole scan including space charge

However in some cases, the space charge forces have to be taken into account for the analysis of quadrupole scan data. The space charge interactions can be integrated into quadrupole scan analysis with the following approximations:

- The electron bunch is an 3D ellipsoid of $\sigma_x, \sigma_y, \sigma_z$, with homogeneous charge distribution.

- The space charge field is linear with x , y and z .
- The transverse emittance does not change with the quadrupole field and remains constant as the beam propagates to the screen of observation.

It can be shown, that in such cases the self field term in particles transverse trajectory equations take the form[23, 24]:

$$x'' = K \frac{1 - \xi(\sigma_z/\sqrt{\sigma_x\sigma_y})}{\sigma_x\sigma_z(\sigma_x + \sigma_y)} x \quad (3.6)$$

$$K = \frac{3Qe}{20\sqrt{5}\pi\epsilon_0\beta^3\gamma^3m_e c^2} \quad (3.7)$$

where $\xi(s)$ is a form factor function given by[24]:

$$\xi(s) = \begin{cases} \frac{1}{1-s^2} - \frac{s}{(1-s^2)^{\frac{3}{2}}} \cos^{-1}(s) & \text{for } s < 1 \\ 1/3 & \text{for } s = 1 \\ \frac{1}{1-s^2} + \frac{s}{(s^2-1)^{\frac{3}{2}}} \cosh^{-1}(s) & \text{for } s > 1 \end{cases} \quad (3.8)$$

An analogous equation to Eq. 3.6 exists for y .

From Eqs. 3.6 the space charge forces can be treated analytically as a defocusing quadrupole. Thus a drift of very small length δl with included space charge has the following transfer matrix:

$$\delta L_{SC} = \begin{pmatrix} 1 & \delta l & 0 & 0 \\ k_x \delta l & 1 & 0 & 0 \\ 0 & 0 & 1 & \delta l \\ 0 & 0 & k_y \delta l & 1 \end{pmatrix} \quad (3.9)$$

with k_x, k_y given by:

$$k_x = K \frac{1 - \xi(\sigma_z/\sqrt{\sigma_x\sigma_y})}{\sigma_x\sigma_z(\sigma_x + \sigma_y)} \quad k_y = K \frac{1 - \xi(\sigma_z/\sqrt{\sigma_x\sigma_y})}{\sigma_y\sigma_z(\sigma_x + \sigma_y)} \quad (3.10)$$

Similarly one obtains a transfer matrix of propagation δl inside a quadrupole of focusing strength k_q :

$$\delta Q_{SC} = \begin{pmatrix} 1 & \delta l & 0 & 0 \\ (k_x - k_q)\delta l & 1 & 0 & 0 \\ 0 & 0 & 1 & \delta l \\ 0 & 0 & (k_y + k_q)\delta l & 1 \end{pmatrix} \quad (3.11)$$

By segmentation of the distance $L_q + L_d$ (see Fig. 3.1) into sufficiently large number N of small pieces δl one can construct stepwise the transfer matrix $L_{SC}Q_{SC} = \prod \delta L_{SC}\delta Q_{SC}$. In order to do this, at each step one has to update σ_x, σ_y according to Eq. 2.19 and then respectively k_x, k_y . At the end one has to replace $L_{SC}Q_{SC}$ in Eq. 3.5 and solve the system for $\Sigma(0)$.

3.1.3 Example, applicability limitations

The quadrupole scan technique for emittance measurements is sensitive to space charge fields. In the cases when the beam is space charge dominated this method tends to overestimate the emittance. The reason is that a space charge dominated beam evolves under the influence of both space charge and emittance effects, while the quadrupole scan analysis either completely neglects or assumes a linear space charge force. This behavior is clearly visible in the graphs of Fig. 3.2. The beam's rms size after the quadrupole was simulated as a function of the quadrupole's gradient at a constant bunch charge of 1 nC. These data were at first analyzed neglecting the space charge forces and then analyzed with taking the linear space charge into account in the way introduced by Eqs. 3.6-3.8. The simulation and data analysis were repeated for various longitudinal beam mean momenta in the range 1-35 MeV/c. Apparently the linear space charge analysis yields results somewhat closer to the true emittance value, but it still significantly overestimates the emittance in the low energy range ($p_z \leq 10$ MeV/c), where PITZ operates. Therefore the quadrupole scan method can be applied to PITZ set up only after the facility upgrade by the installation of a booster cavity and after the commissioning of the 10 MW klystron as foreseen for 2005.

3.2 Multi slit-Pepper Pot technique

An important advantage of the multi slit method is that it is applicable to high brightness, space charge dominated beams (as in the PITZ case). This technique makes use of the fact that space charge-over-emittance ratio scales as $(d/R)^2$, where d is the slit width and R the radius of the incoming beam. Thus with a slit of proper width the beamlets charge will be low enough that the contribution from self field forces to the transverse momentum can be neglected. The typical set-up for a multi-slit/pepper pot measurement is shown on Fig. 3.3 (a). A metal mask composed of a set of slits or holes in case of the pepper pot is used to sample the initial transverse phase space distribution, as shown in Fig 3.3 (b). The beam is transformed into small beamlets, which retain the uncorrelated divergence of the original beam. The beamlet profiles are observed on a screen situated at a distance L downstream, where the measured rms size $\tilde{\sigma}_i$ of the i^{th} beamlet image directly corresponds to the uncorrelated divergence $\tilde{x}'_i \cong \tilde{\sigma}_i/L$. The goal is to evaluate the rms emittance as defined in Eq. 2.6, which requires the computation of the total (correlated and uncorrelated) divergence $\langle x'^2 \rangle$ as well as the correlation $\langle xx' \rangle$. A more practical and numerically robust approach is to shear the phase space in or-

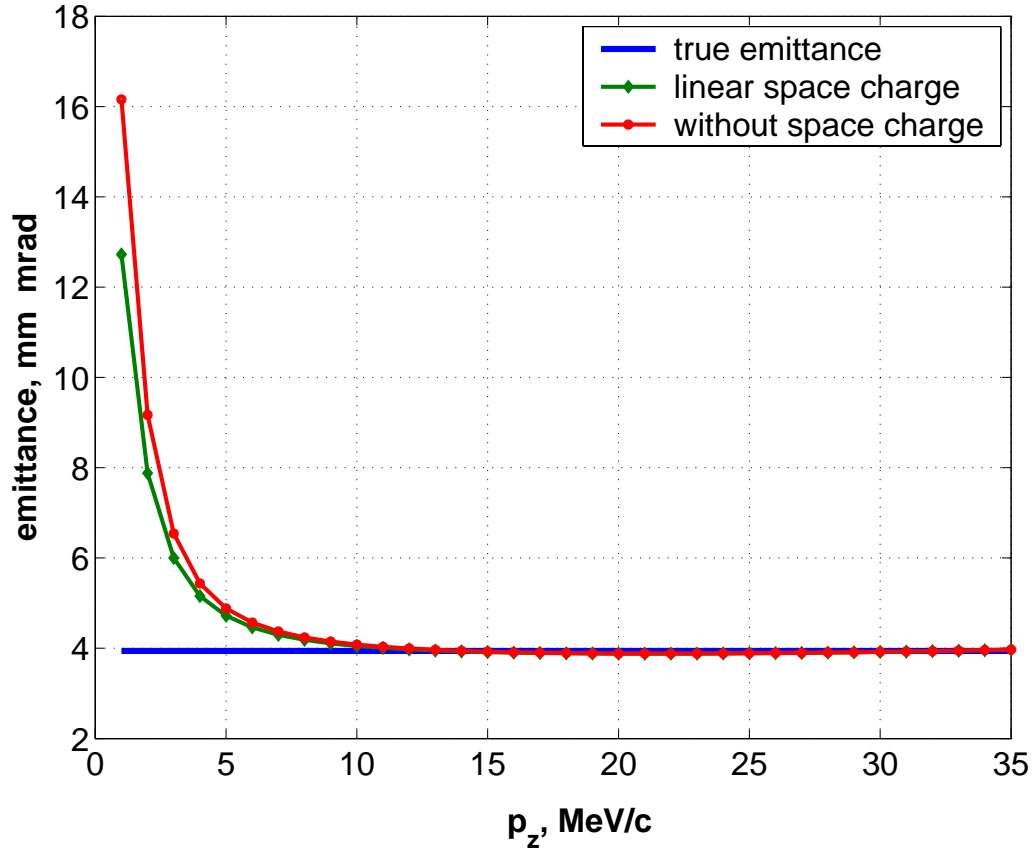
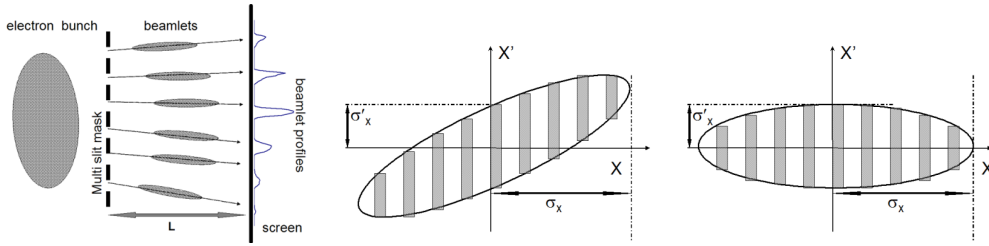


Figure 3.2: Simulated quad scan measurements for various longitudinal beam momenta p_z . Shown are results obtained after neglecting the space charge forces as well as with taking linear space charge forces into account.

der to cancel the correlation [25] as illustrated in Fig. 3.3 (c) and then apply the equivalent emittance definition:

$$\epsilon_{x,rms} = \sqrt{\langle x^2 \rangle \langle \tilde{x}'^2 \rangle} = \sqrt{\langle x^2 \rangle \left\langle \frac{\tilde{\sigma}^2}{L^2} \right\rangle} \quad (3.12)$$

The rms size $\sqrt{\langle x^2 \rangle}$ is usually measured directly by observing the beam profile on a screen with scintillating material inserted at the position of the slit mask. An expression for the rms uncorrelated divergence $\langle \tilde{x}'^2 \rangle$ of the beam can be derived considering the phase space shown in Fig. 3.3 (c). Since the slit width is typically negligible compared to rms beam size, the phase space distribution function $f(x, \tilde{x}')$ may be represented as a sum of



(a) The typical set up of a multi slit emittance measurement consists of a slit mask and a screen after a drift of length L .

(b) The transverse phase space is being sampled by the slits, producing beamlets of the same uncorrelated divergence as the beam.

(c) A shearing transformation removes the correlation and preserves the phase space area. The shaded stripes correspond to the sampling by the slits as shown (b).

Figure 3.3: Principle of multi slit (pepper pot) measurement.

δ -functions:

$$f(x, \tilde{x}') = \sum g_i(\tilde{x}') \delta(x - x_i) \Rightarrow 1 = \sum \int d\tilde{x}' g_i(\tilde{x}') \equiv \sum w_i \quad (3.13)$$

Here $\{g_i(\tilde{x}')\}$ describe the divergence distribution of the individual beamlets and the integrals w_i correspond to their weight. From Eq. 3.13 it follows:

$$\langle \tilde{x}'^2 \rangle = \sum \int \int dx d\tilde{x}' \tilde{x}'^2 g_i(\tilde{x}') \delta(x - x_i) = \sum w_i \langle \tilde{x}'^2 \rangle_i \quad (3.14)$$

$$\Rightarrow \langle \tilde{x}'^2 \rangle = \sum w_i \left(\frac{\tilde{\sigma}_i}{L} \right)^2 \quad (3.15)$$

Often when measuring with a multi-slit mask the beamlet profiles partially overlap on the screen. In such cases the projected intensity is fitted to a sum of gaussian functions in order to estimate the size of the beamlets and their contribution to the overall intensity distribution. However the applicability of this method is limited to the cases when the overlapping is not too strong and fits well to the above-mentioned sum of gaussian distributions. A variation of the multi-slit method is the so-called single-slit scan. In the single-slit scan one uses a mask with only one slit, which produces only one beamlet. One moves the slit to different transverse positions by certain steps. At each step the intensity distribution of the beamlet's profile is measured. Finally one applies the same formulae as for the multi-slit measurement. The

scanning with a single slit gives the possibility to analyze each profile separately without any assumption of the beam shape. Another advantage of a single-slit scan is that one can sample the phase space distribution at a large number of transverse positions. Depending on the accuracy of transverse positioning of the slit mask and the beam size, the number of samples could reach 10 or more, while the number of the samples taken with a multi-slit mask is limited by the spacing between the slits and it is typically less than 10.

3.3 Emittance measurement system at PITZ

For measuring the transverse emittance at PITZ the multi-slit/pepper pot technique is employed. The concrete realization of the emittance measurement system (EMSY) follows some general design considerations. All technical solutions are brought into line with the requirements introduced in [26, 27]. In this section the most essential of these requirements are summarized.

3.3.1 Accuracy of angular alignment

When a multi-slit mask intercepts the electron beam it stops or scatters most of the particles, but few of them which are mapped into special areas in the transverse phase space. The slit cuts out a rhombic area of the phase space as shown in Fig. 3.4. Provided that the ratio $\frac{2r}{l}$ between the slit width and the mask thickness is much less than unity, then the rhombic area is defined by the points $\{X_S - r, 0\}$, $\{X_S + r, -\frac{2r}{l}\}$, $\{X_S + r, 0\}$, $\{X_S - r, \frac{2r}{l}\}$. Here X_S is the transverse position of the slit and $\frac{2r}{l}$ gives its acceptance angle. If the slit is tilted by an angle Φ with respect to the beam propagation direction, then the whole rhombic area is shifted as shown in Fig. 3.4. In order to be negligible, the alignment error Φ should be small compared to the opening angle $\frac{2r}{l}$ [26]. Typical opening angles are in the order of 1 degree. The condition $\Phi \ll \frac{2r}{l}$ implies $\Phi \ll 1$ deg. At PITZ the accuracy of the angular alignment of the masks is $\Phi \approx 1 \cdot 10^{-3}$ deg., achieved by the usage of high-precision rotation stages (type RV120PEHL [28]).

3.3.2 Accuracy of spatial positioning

The high precision spatial positioning is needed especially for the realization of a single-slit scan measurement. For that reason the positioning error δx should be much smaller than the transverse size R of the beam. With

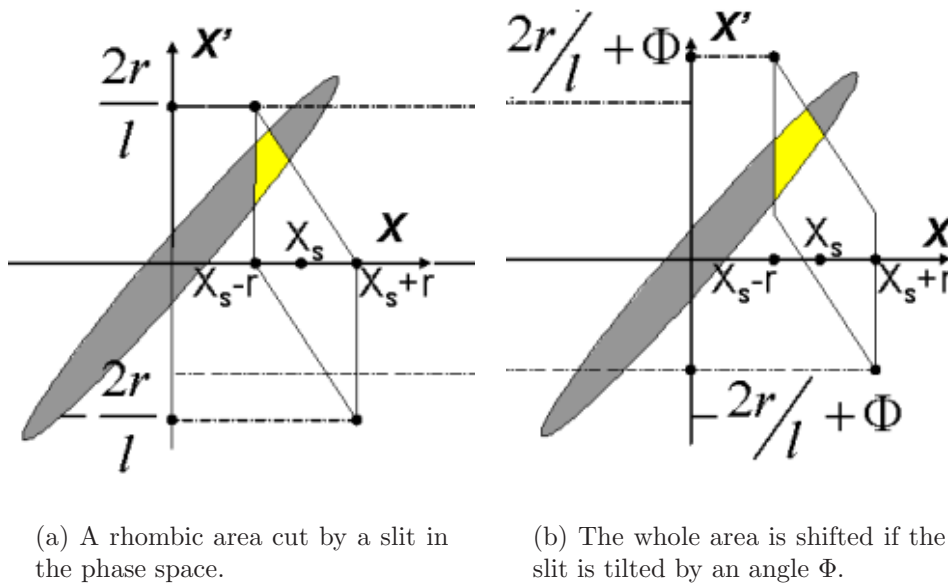


Figure 3.4: The mask stops or scatters most of the particles, but few of them which are mapped into special areas (marked in yellow) in the transverse phase space.

typical values of R of 1 mm if follows $\delta x \ll 1$ mm. The stepper motors (type MTM100PP1 [28]) and the motion controller put into operation at PITZ allow spatial positioning with an accuracy of $\delta x = 1 \mu\text{m}$.

3.3.3 Distance to screen of observation

The distance between the slit mask and the observation screen should be chosen in such a way, that it is possible to resolve the minimum expected divergence. The contribution of the slit width to the size of the beamlet profile should be negligible. Typically the beamlet's rms size $\tilde{\sigma}$ after a drift distance of length L is given by:

$$\tilde{\sigma} = \sqrt{L^2 \cdot \sigma'^2 + \frac{(2r)^2}{12}} \quad (3.16)$$

Here σ' is the beam divergence (min. approx. 0.1 mrad) and $2r$ is the slit width. The requirement $L \cdot \sigma' \gg 2r/\sqrt{12}$ implies $L \gg 2r/(\sigma'\sqrt{12})$. With $2r=50 \mu\text{m}$ and $\sigma'=0.1$ mrad one obtains $L \gg 0.14$ m. At PITZ the drift distance is $L = 1.01$ m.

3.3.4 Layout of the masks

3.3.4.1 Slit width

The evolution of the transverse rms beam size of a relativistic electron bunch in a drift is given by the equation[29]:

$$\sigma_x'' = \frac{\epsilon_{x,n}^2}{\gamma^2 \sigma_x^3} + \frac{4I}{\gamma^3 I_0 (\sigma_x + \sigma_y)} \quad (3.17)$$

where γ is the Lorentz factor, I is the peak beam current, $I_0=17$ kA is the characteristic (Alfven) current and $\epsilon_{x,n}$ is the normalized horizontal emittance. Here and in the following σ_x and σ_y denote the horizontal and the vertical rms beam size and the prime denotes differentiation with respect to the beam propagation direction. The two terms in the RHS of Eq. 3.17 represent the effects due to emittance and space charge respectively. The space charge-over-emittance ratio ρ is defined as the ratio between the space charge and the emittance terms:

$$\rho = \frac{4I\sigma_x^3}{I_0\gamma\epsilon_{n,x}^2(\sigma_x + \sigma_y)} \quad (3.18)$$

The case $\rho > 1$ indicates that the transverse beam dynamics is dominated by the space charge forces i.e. the beam is space charge dominated. In the opposite case when $\rho < 1$ the beam is emittance dominated.

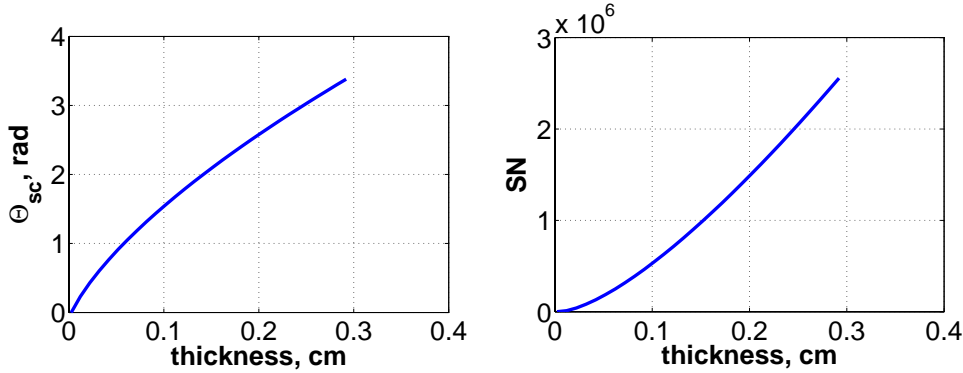
Considering the slit width, denoted in the following with $2r$, one should take into account two requirements[27]:

- the beamlets produced by a slit mask must be emittance dominated
- the contribution of the initial beamlet size to the beamlet size at the observation screen should be as small as possible

The first item is of prime importance for transverse emittance diagnostics, since the beam produced by the PITZ injector is space charge dominated at almost all operation parameters. Assuming a round beam with some typical beam parameters for PITZ like $\sigma_x \simeq 0.5$ mm, $I \simeq 50$ A, $\gamma \simeq 10$, $\epsilon_{n,x} \simeq 1$ mm · mrad one obtains $\rho \approx 150$. This large value of ρ shows that the beam is heavily space charge dominated. After passing through a vertical slit the horizontal beam size, the peak current and the emittance scale by a factor ξ that depends on the slit width and rms beam size so that $\xi = 2r/(\sqrt{12}\sigma_x)$. In such case the scaling law is as follows: $I \rightarrow \xi \cdot I$, $\sigma_x \rightarrow \xi \cdot \sigma_x$, $\sigma_y = \text{const}$, $\epsilon_{n,x} \rightarrow \xi \cdot \epsilon_{n,x}$ and from Eq. 3.18 it follows that $\rho \rightarrow \xi^2 \cdot \rho$. For the PITZ

operation parameters considered above, a slit opening of $50\ \mu\text{m}$ gives a scaling factor $\xi^2 \approx 8 \cdot 10^{-4}$ and thus the space charge-over-emittance ratio after the slit would become $\rho \approx 0.1$. In order to resolve a wide range of transverse emittance values, slits of $50\ \mu\text{m}$ as well as $20\ \mu\text{m}$ width were produced.

3.3.4.2 Mask material and thickness



(a) RMS scattering angle for 5 MeV electrons in a tungsten plate of variable thickness.

(b) Lower theoretical limit of signal-to-noise ratio at a screen situated at $L=1.01\ \text{m}$ after a tungsten mask of variable thickness.

Figure 3.5: RMS scattering angle Θ and signal-to-noise ratio SN calculated for various thicknesses of the mask plate.

The mask plate material was chosen to be tungsten due to its high melting temperature ($T_{\text{melt}}=3653\ \text{K}$) and short radiation length ($X_0=0.35\ \text{cm}$). The plate thickness is a compromise between the need to stop or scatter the electrons which are not passing through the slit into an uniform background and the desire not to affect significantly the measurement because of the edge scattering of the electrons[27]. The latter phenomenon tends to corrupt the beam divergence if the thickness is too large, because the electrons with large divergence are scattered on the slit edge. One can optimize the plate thickness so that the rms scattering angle is large enough and the scattered electrons contribute to the beamlets intensity only as uniform background. This means that if D is the diameter of the viewing screen, L the distance between the screen and the slit mask and Θ the rms scattering angle then $\Theta \gg D/L$ is required. Assuming a screen diameter $D=2\ \text{cm}$ and distance $L=1\ \text{m}$ yields $\Theta \gg 20\ \text{mrad}$. An estimation for the needed mask thickness s

can be given considering the angle $\Theta(s)$ and the signal-to-noise ratio SN on the observation screen. The scattering angle is given by the relation[26]:

$$\Theta(s) = \frac{19.2\text{MeV}}{E} \sqrt{\frac{s}{X_0}} \left[1 + 0.2 \ln \left(\frac{s}{X_0} \right) \right] \quad (3.19)$$

here E denotes the beam energy. In Fig. 3.5 (a) it is shown how Θ depends on the thickness of the tungsten mask, when the electrons energy is 5 MeV. The dependence of SN on mask thickness is given by the following expression[26]:

$$SN(s) \geq \frac{(\Theta \cdot L)^2}{2\sigma^2 \left(1 + \frac{\sigma' \cdot L}{2r} \right)^2} \quad (3.20)$$

where σ, σ' are the rms size and the divergence of the incoming electron beam. Fig. 3.5 (b) shows the expected signal-to-noise ratio SN as a function of s for the case when $2r=50 \mu\text{m}$. From the two graphs above it follows that a tungsten plate of 1 mm thickness should be sufficient for emittance measurements at beam energies of about 5 MeV.

3.3.5 Error calculations

According to Eq. 3.12 the normalized rms emittance is given by:

$$\epsilon_{n,x} = \beta\gamma \cdot \sigma_x \cdot \tilde{\sigma}'_x = \frac{\bar{p}_z [\text{MeV}/c]}{0.511} \cdot \sigma_x \cdot \tilde{\sigma}'_x \quad (3.21)$$

where σ_x is the rms beam size directly measured at the slit mask position, $\tilde{\sigma}'_x$ is the uncorrelated rms beam divergence calculated according to Eq. 3.15 and \bar{p}_z is mean longitudinal beam momentum measured with the help of the dipole spectrometer. Then the emittance measurement error basically will be given by the expression:

$$\frac{\delta\epsilon_{n,x}}{\epsilon_{n,x}} = \sqrt{\left(\frac{\delta\bar{p}_z}{\bar{p}_z} \right)^2 + \left(\frac{\delta\sigma_x}{\sigma_x} \right)^2 + \left(\frac{\delta\tilde{\sigma}'_x}{\tilde{\sigma}'_x} \right)^2} \quad (3.22)$$

In the following each one of the terms in the quadratic sum above will be discussed.

3.3.5.1 Error in momentum measurement - $\delta\bar{p}_z$

The error of mean momentum is determined mainly by two systematic contributions. The first of them is the relative error of about 0.8% [6] due to

uncertainty in the order of 0.5° in the angle between the beam pipe of the dispersive arm and the direction of electrons in front of the dipole. The second systematic error of about 0.9% [6] is due to the uncertainty of the fit parameters of the curve describing the dependence of dipole magnetic field B_{dipole} as a function of dipole current I_{dipole} . With further considerations of statistical fluctuations and camera calibration uncertainty one can estimate the total relative error of momentum measurement $\frac{\delta \bar{p}_z}{\bar{p}_z} \simeq 2\%$

3.3.5.2 Errors in beam size measurement - $\delta\sigma_x$

The beam position and rms size measurements are performed by calculating first and second central moments of intensity distributions of images obtained by CCD cameras. A description of the camera system can be found in [30]. Concerning beam size measurements there are several sources of errors which have to be taken into account and which are related to the specific measurement set up.

- $\delta\sigma_{pixel}$: The error due to the finite pixel size of the CCD camera. An optical system images the screen area onto the CCD chip with a certain and known demagnification coefficient M , usually in the range 2-10. Thus the error due to the finite camera pixel size can be estimated $\delta\sigma_{pixel} = \frac{M}{\sqrt{12}} \cdot 8.3\mu m$, where $8.3\mu m$ is the pixel size of the CCD camera chip used for the measurements presented in this thesis. Typically this error is in the range 1-5%.
- $\delta\sigma_{noise}$: Error due to electronic and dark current noise. In order to minimize the influence of the noise due to dark current and electronic noise a background subtraction is applied prior to the calculation of beam positions and rms sizes. Since the background subtraction is never perfect the remaining noise still contributes to the rms size. An estimation $\delta\sigma_{noise}$ of this influence can be given considering the mean and the peak values of the noise signal [31]. Typically this error is in the range 1-5%.
- $\delta\sigma_{stat}$: Error determined by the random small fluctuations in working point of the machine systems and components during the measurement. This includes jitter of rf power and rf phase, cathode laser pointing stability, laser intensity fluctuations, variation of magnet currents etc. The statistical error $\delta\sigma_{stat}$ is calculated as the standard deviation of N subsequent beam size measurements, where usually $N=50$. Most typically this error is in the order of 1%.

- All errors add up quadratically $\delta\sigma_x = \sqrt{\delta\sigma_{pixel}^2 + \delta\sigma_{noise}^2 + \delta\sigma_{stat}^2}$

3.3.5.3 Errors in beam divergence measurement - $\delta\tilde{\sigma}'_x$

Since the divergence measurements are reduced to beam size measurements (see Eq. 3.12), the same arguments apply as for calculation of $\delta\sigma_x$ above. However there is an additional contribution due to the finite slit width:

- $\delta\tilde{\sigma}'_{slit} = \frac{w}{\sqrt{12}L} \simeq 0.01$ mrad. Typically this error is in the order of about 1%.

- All errors add up quadratically $\delta\tilde{\sigma}'_x = \sqrt{\delta\sigma_{pixel}^{\prime 2} + \delta\tilde{\sigma}_{noise}^{\prime 2} + \delta\tilde{\sigma}_{stat}^{\prime 2} + \delta\tilde{\sigma}_{slit}^{\prime 2}}$

For each individual emittance measurement the errors $\delta\tilde{\sigma}'_x$, $\delta\sigma_x$ and $\delta\bar{p}_z$ have to be determined and enter in the total emittance measurement error according to Eq. 3.22.

Chapter 4

Thermal emittance measurements

4.1 Introduction

The origin of the term *thermal emittance* can be traced back to thermionic cathodes, where the electrons in metal cathode material are regarded as Fermi-Dirac gas with temperature T typically in the order of 10^3 K. As given by Lawson[32], the Maxwellian velocity distribution corresponding to kT relates to the initial normalized beam emittance:

$$\epsilon_{th} \propto \sqrt{kT} \quad (4.1)$$

The case of photoemission from a semiconductor cathode involves different mechanisms (details in next section), but the thermal i.e. initial beam emittance is given by a similar relation:

$$\epsilon_{th} \propto \sqrt{E_k} \quad (4.2)$$

Here E_k denotes the mean kinetic energy of the photoelectrons immediately after emission. The thermal emittance adds in quadrature to the other emittance contributions, thus it sets the lower limit for the emittance in electron sources. Numerous theoretical and experimental studies have been dedicated to the measurements e.g. [33, 34, 35, 36] as well as to solutions for the reduction [37, 38] of the thermal emittance. Everywhere the authors point out the high importance of thermal emittance measurements to understand and to improve the ultimate performance of injectors feeding linac driven FELs. Among the various possible photocathode materials, the semi conductive alkali telluride Cs_2Te shows high quantum efficiency (QE), high robustness and long lifetime [36] and therefore has been chosen for PITZ as well as for many

other photoinjectors. First thermal emittance measurements for Cs₂Te photocathodes under real rf operating conditions were performed at PITZ and will be presented in the following sections.

The thermal emittance depends[33] on the laser spot size, the momentum

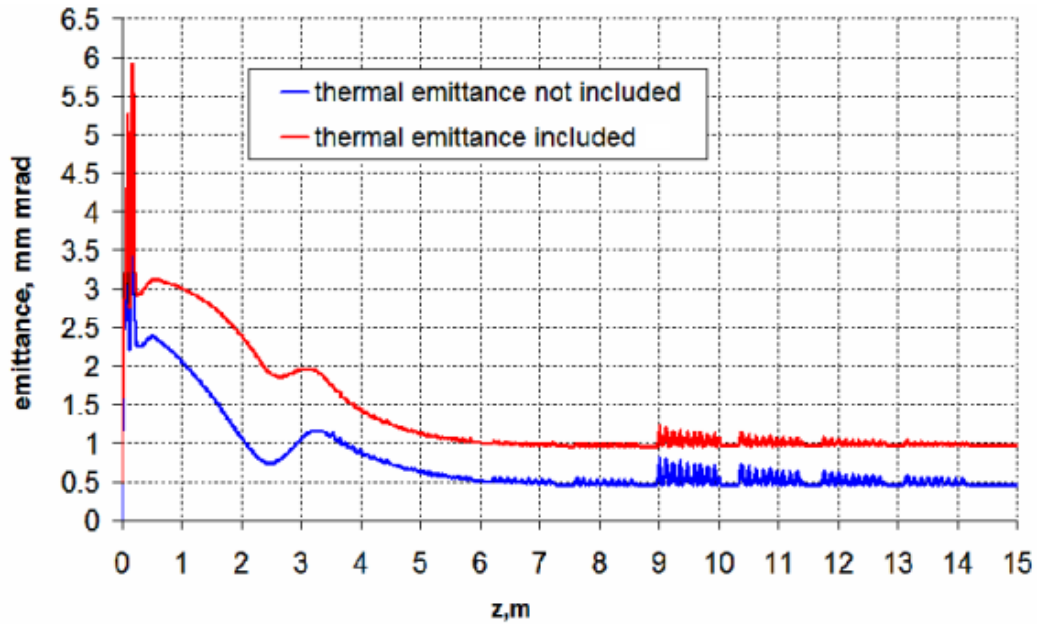


Figure 4.1: The thermal emittance might spend up to 50% of the emittance budget. These simulations show the emittance evolution along the XFEL injector beamline. Two scenarios are considered: with and without taking the thermal emittance into account.

and the angular distribution of the emitted photoelectrons. Its typical value is small, usually in the range 0.3-0.7 mm·mrad and therefore it starts to play a significant role in the emittance formation, when the injector operating parameters have been fully optimized so that very low emittances in the order of 1 mm·mrad are about to be produced. In such situations the thermal emittance might spend up to 50% of the emittance budget, as shown with simulations in Fig. 4.1. Both simulations have been done for the optimized operating conditions of the XFEL injector, as described in the XFEL CDR [39]. It is important to note that the thermal emittance is a quantity influenced not only by the photocathode material properties but also by the parameters of the cathode UV laser and the accelerating field amplitude. In planning the measurements one has to consider the dependence on the rms laser spot size, on lowering the surface potential barrier due to the high

rf field (Schottky effect) and on passivation of the cathode surface due to increased vacuum pressure.

4.2 Photoemission model for Cs₂Te. Emittance calculation

In order to give a correct physical interpretation of the thermal emittance measurements, it is necessary to introduce a model of the photoemission from Cs₂Te as well as a model for the thermal emittance calculation.

4.2.1 Photoemission model

The photoemission in semiconductors can be described by the three-step model introduced by Spicer[40] and further studied by Powell[41], which was found to be relevant to describe the behaviour of photocathodes [42]. According to this model the photoemission takes place in the following sequence as illustrated schematically in Fig. 4.2:

- **Step 1: Absorption of a photon in the bulk material and excitation of electrons to the conduction band (CB).**

Since Cs₂Te is a semiconductor material of band gap $E_G = 3.3$ eV, a photon energy $E_{ph} > 3.3$ eV is required. The UV laser put into operation at PITZ generates photons at a wavelength of $\lambda = 262$ nm or $E_{ph} = 4.72$ eV.

- **Step 2: Transport of these electrons to the maximum of the CB density of states, where the dominant energy loss mechanism in the CB are electron-phonon collisions.**

The first maximum of the density of states in the CB of Cs₂Te is located at an energy of 4.05 eV above the maximum of the valence band (VB). The used photon energy of $E_{ph} = 4.72$ eV is sufficient to excite valence band electrons to this level. However, it would not be enough for excitation into the second maximum of the density of states in the CB at an energy of 4.9 eV and therefore transitions to the second maximum will not be considered in the thermal emittance calculations.

- **Step 3: Escape of the electrons into vacuum.**

In order to escape from the conduction band to the vacuum, electrons have to overcome the surface potential barrier given by the electron affinity E_A , which is defined as the energy difference between the vacuum level E_{vac} and the bottom of the conduction band. Thus, the

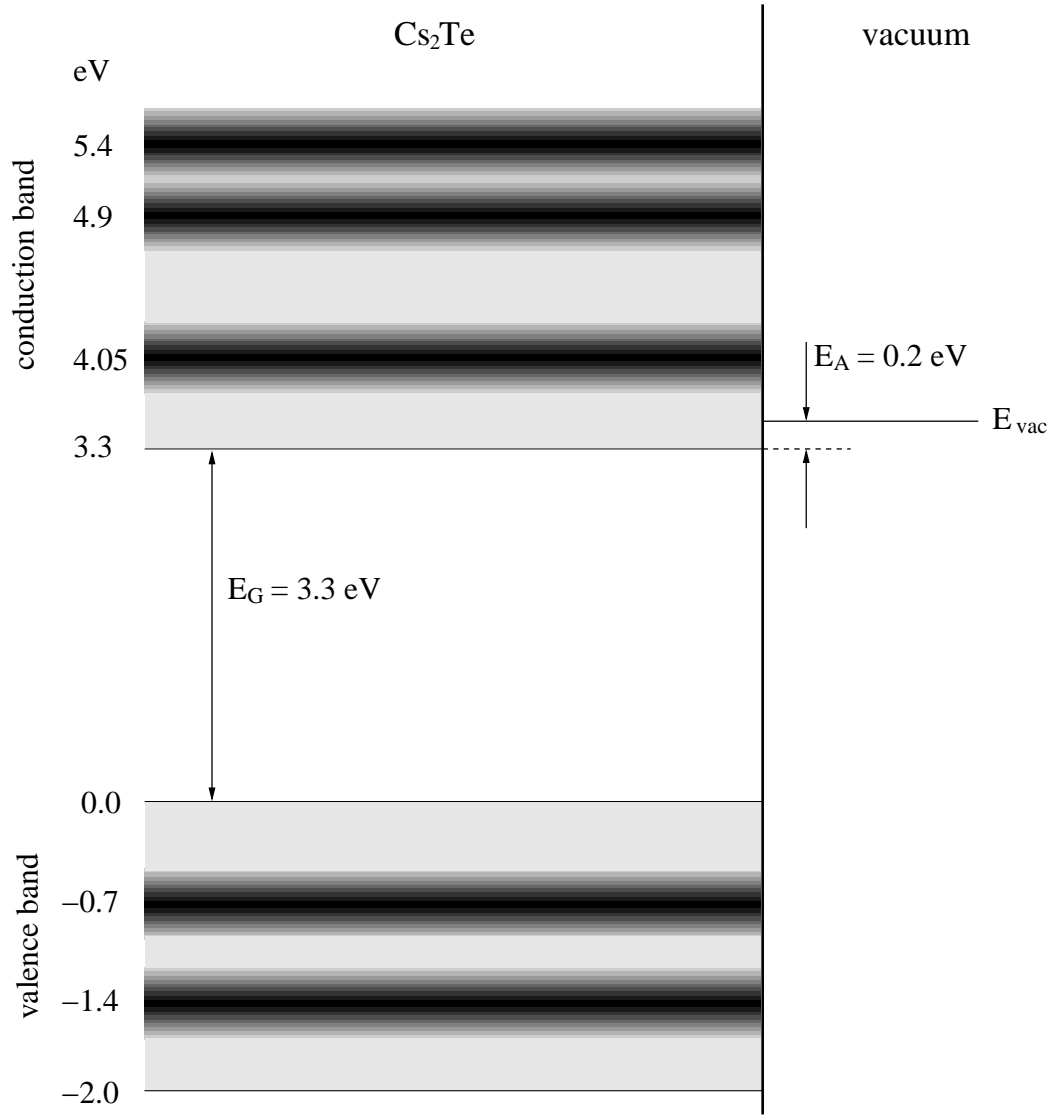


Figure 4.2: Schematic structure of the energy levels of Cs₂Te according to [33]. The maxima of density of states are shown in dark. The vacuum level is about 3.5 eV above the VB maximum. The laser photons with an energy of 4.72 eV excite the electrons to a final energy 4.05 eV in the CB, corresponding to a kinetic energy $E_k = 0.55$ eV of a free electron.

threshold energy $E_T = E_{vac}$ for photoemission is given by the sum of the band gap and the electron affinity: $E_T = E_A + E_G$. The threshold energy for Cs₂Te is measured to be $E_T = 3.5$ eV and hence the electron affinity for a fresh cathode can be estimated by: $E_A = E_T - E_G = 0.2$ eV

(due to cathode oxidation E_A might become larger). Since the electron's final state energy in Step 2 is on average $E_{CB} = 4.05$ eV, after escaping into the vacuum it will have a mean kinetic energy of $E_k = E_{CB} - E_{vac} = 4.05 - 3.5 = 0.55$ eV.

The above quoted value for the average kinetic energy of the emitted photoelectrons was estimated considering the measurements of Powell[41] performed with fresh cathodes and very low electric fields. However the actual value of E_k obtained when the cathode is operated in an rf gun with high accelerating gradient might be larger because of reduction of the electron affinity due to Schottky effect or lower due to oxidation of the cathode surface.

4.2.2 Thermal emittance calculation

Following the considerations of Flöttmann[33] one can derive a relation between the thermal emittance and photoemission parameters: the average kinetic energy of the emitted photoelectrons and the electron affinity. The normalized rms emittance is defined by the following expression:

$$\epsilon_{th} = \frac{1}{m_0 c} \sqrt{\langle x^2 \rangle \langle p_x^2 \rangle - \langle xp_x \rangle^2} \quad (4.3)$$

where x denotes the transverse coordinate of a particle and p_x the corresponding transverse momentum component. In the equation above $\langle x \rangle = 0$ and $\langle p_x \rangle = 0$ has been assumed. At the cathode there is no correlation in phase space i.e.

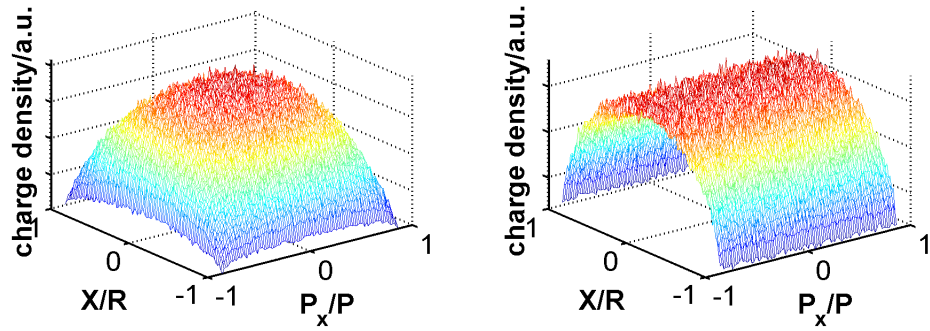
$$\langle xp_x \rangle = 0 \quad (4.4)$$

With Eq. 4.4 one can re-write Eq. 4.3 as:

$$\epsilon_{th} = \sigma_r \frac{p_{x,rms}}{m_0 c} \quad (4.5)$$

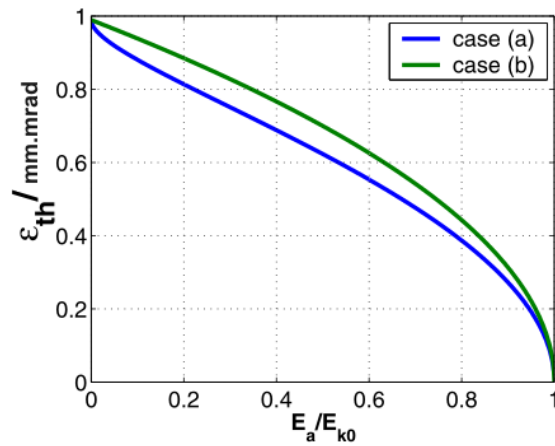
where σ_r denotes the laser spot size at the cathode and $p_{x,rms}$ is the rms transverse momentum spread. One can think of different models to describe analytically the escape of electrons from the cathode surface into vacuum. In one model one assumes that the electrons are emitted isotropically into the hemisphere over the cathode surface with an energy $E_{k0} = E_{CB} - E_G$. The electrons must in addition overcome the hurdle of the potential barrier given by the electron affinity E_A . If ϕ and θ denote the azimuth and meridian angles and p the full momentum of a particle, then transverse and longitudinal momentum components can be expressed as:

$$p_x = p \cdot \sin \phi \cdot \cos \theta \quad p_z = p \cdot \cos \phi \quad (4.6)$$



(a) Phase space charge distribution for the model corresponding to Eq. 4.8

(b) Phase space charge distribution for the model corresponding to Eq. 4.10



(c) Normalized thermal emittance as a function of electron affinity. Considered are both phase spaces shown above.

Figure 4.3: The phase spaces for the two emission models are reconstructed with Monte Carlo simulation. It is assumed that the electrons are emitted from a homogeneous circular cathode of radius $R=2$ mm.

The potential barrier will stop all particles with longitudinal momentum $p_z < \sqrt{2m_0 E_A}$ i.e. all electrons emitted with azimuth angles larger than $\phi_{max} = \arccos \sqrt{\frac{E_A}{E_{k0}}}$ will not escape into the vacuum. With this model the rms value of transverse component of the momentum $p_{x,rms}$ can be deter-

mined by the integral:

$$p_{x,rms} = \sqrt{\frac{\int_0^{\phi_{max}} \int_0^{2\pi} p_x^2 \cdot \sin \phi \cdot d\theta \cdot d\phi}{\int_0^{\phi_{max}} \int_0^{2\pi} \sin \phi \cdot d\theta \cdot d\phi}} \quad (4.7)$$

Integrating Eq. 4.7 and plugging the result into Eq. 4.5 yields the following expression for the thermal emittance:

$$\epsilon_{th} = \sigma_r \sqrt{\frac{2E_{k0}}{3m_0c^2}} \cdot \sqrt{\frac{2 + \cos^3 \phi_{max} - 3 \cos \phi_{max}}{2(1 - \cos \phi_{max})}} \quad (4.8)$$

Another analytical approach to calculate the rms transverse momentum spread is to assume an isotropic emission into the hemisphere over the cathode surface but this time behind the potential barrier. The average kinetic energy of photoelectrons is defined as:

$$E_k = E_{CB} - E_G - E_A \quad (4.9)$$

Since the emission is assumed to take place behind the potential barrier, $\phi_{max} = \pi/2$ and the same calculations as introduced in Eq. 4.7, Eq. 4.8 yield the relation for the thermal emittance:

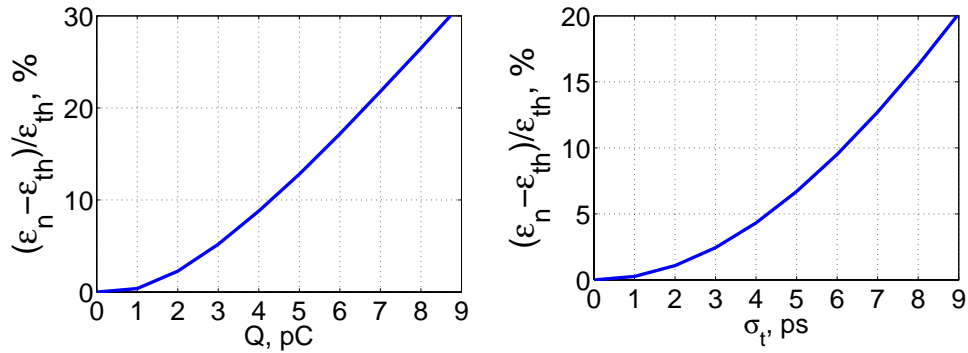
$$\epsilon_{th} = \sigma_r \sqrt{\frac{2E_k}{3m_0c^2}} \quad (4.10)$$

The phase spaces of the two discussed models corresponding to Eq. 4.8 and Eq. 4.10 look somewhat different as it is shown in Fig. 4.3 (a) and (b), however the discrepancy between thermal emittance values is small as demonstrated in Fig. 4.3(c). Since the maximum transverse momentum in both models is the same, the estimation given in Eq. 4.10 is the upper limit for the thermal emittance due to the maximum emission cone angle $\phi_{max} = \pi/2$, which is assumed.

4.3 Operation parameters

As discussed above the thermal emittance determines the lower emittance limit for an rf gun because it adds quadratically to the other emittance terms to form the total emittance: $\epsilon_n \approx \sqrt{\epsilon_{th}^2 + \epsilon_{rf}^2 + \epsilon_{sc}^2}$. This relation has to be taken into account in order to determine the operation conditions needed to perform thermal emittance measurements. The main problem is that with

the PITZ set up one can not measure the thermal emittance directly at the photocathode (inside the rf gun), but at the position of the emittance measurement system (EMSY), which is located about 1.62 m downstream. This means that one measures not only thermal emittance but the contributions of the rf field and the space charge as well. Under proper operation conditions the last two terms should be minimized so that $\epsilon_n \approx \epsilon_{th}$. The space charge contribution to the emittance rapidly scales up with the charge as presented in Fig. 4.4(a), which implies that the bunch charge should be set as close as possible to zero. On the other hand one has to keep the signal-to-noise ratio during the emittance measurement sufficiently high, which sets a lower limit to the charge. According to the practical experience a charge of about 3 pC is a reasonable compromise between these contradicting requirements. For this charge, the relative emittance increase due to self-fields should not be larger than 5%.



(a) A simulation showing not more than 5% relative emittance increase due to space charge at $Q=3$ pC

(b) A simulation showing not more than 2% relative emittance increase due to the rf field for $\sigma_t = 3$ ps

Figure 4.4: ASTRA simulations to determine the required bunch charge and cathode laser pulse length as well as possible errors due to space charge and rf.

Regarding the contribution of the rf field it is helpful to recall that $\epsilon_{rf} \propto \sigma_t^2$ [19], where σ_t is the length of the laser micropulse. Hence the laser pulse length has to be shortened to the possible limit. The laser system of PITZ can generate gaussian pulses of $\sigma_t \approx 3$ ps, through bypassing the longitudinal pulse shaper and feeding the output of the pulse train oscillator (see Fig. 1.2(a)) directly to the preamplifier. A further reduction of the temporal extent of the laser pulses is not possible without major reconstruction of the system. According to the simulation results plotted in Fig. 4.4(b)

the rf induced emittance growth is expected to be not more than 2% of the thermal emittance for a pulse length of 3 ps. Taking into account that for the tiny charge of 3 pC the beam current $I \simeq Q/\sigma_t$ is just about 1 A, one has to consider to lower the accelerating rf gradient in order to minimize the dark current and its impact on the emittance and the data analysis. For that reason most measurements were done at an accelerating field of about 32-34 MV/m, since the experimental studies[43] show that the PITZ gun (with inserted Cs₂Te photocathode) produces a negligible dark current of about $1 \cdot 10^{-4}$ A for a peak gradient of 34 MV/m. The rf phase for the measurements was always set to the phase of maximal mean energy gain, although a large emittance variation with the phase for that small charge is not expected.

4.4 Emittance scaling with laser spot size

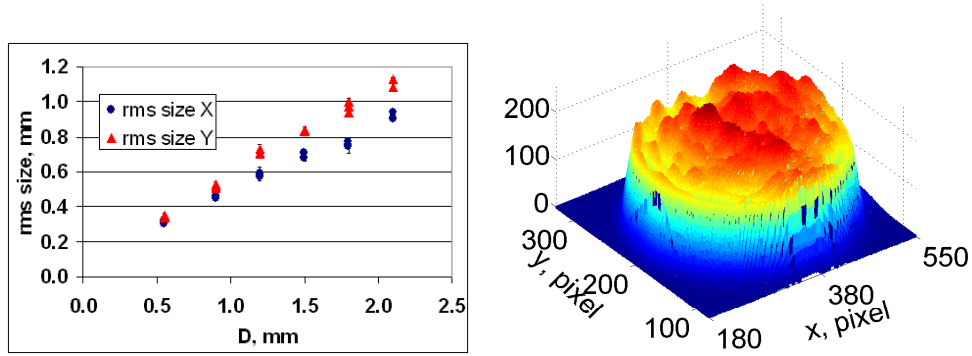
The final goal of these studies is to estimate the average kinetic energy E_k of the electrons immediately after emission from the Cs₂Te photocathode. By differentiation of both sides of Eq. 4.10 one obtains a relation between energy of the electrons and the rate of increase of emittance with the laser spot size σ_r .

$$E_k = 1.5m_0c^2 \left(\frac{d\epsilon_{th}}{d\sigma_r} \right)^2 \quad (4.11)$$

Thus an estimate for E_k can be given, provided that the slope ($d\epsilon_{th}/d\sigma_r$) is known. It can be determined by measuring the emittance as a function of the laser spot size and then fitting a straight line through the measured data points.

The emittance was measured vs. laser rms spot size using the slit scanning technique at a small bunch charge of 3 pC and a moderate gradient of about 32 MV/m. The variation of the laser spot size was realized by passing the initial laser beam through a circular aperture of changeable diameter $D = \{0.55; 0.90; 1.00; 1.20; 1.50; 1.80; 2.10\}$ mm. In Fig. 4.5 it is shown how the laser spot size changes with the diameter of the shaping aperture. Since the transverse intensity profile was kept fairly homogeneous, with an rms intensity modulation in the range of 5-10 %, the laser spot size scales linearly with D . The small difference between the x- and y- rms spot size is due to non homogeneous laser intensity distribution before the shaping aperture.

Two sets of measurements were taken for two different Cs₂Te cathodes: cathode №60 (see Fig. 4.6) with QE of about 1 % at the time of the measurements and cathode №61 (see Fig. 4.7) with QE of about 1.5 %. Straight line fits



(a) The laser spot rms size is shown as a function of the aperture diameter

(b) The typical transverse profile is close to flat top with rms intensity modulation of 5-10%

Figure 4.5: Variation of the laser spot size with the shaping aperture diameter and the transverse intensity profile.

through the measured data for the horizontal as well as for the vertical emittance yield the following results for cathode №60:

$$\frac{d\epsilon_{th,x}}{d\sigma_x} \approx 1.25 \text{ mrad} \Rightarrow E_k \approx 1.2 \text{ eV}; \quad \frac{d\epsilon_{th,y}}{d\sigma_y} \approx 1.1 \text{ mrad} \Rightarrow E_k \approx 0.9 \text{ eV} \quad (4.12)$$

Since there is no reason to expect the energies obtained for both transverse planes to differ, one takes their average as a final result with an uncertainty equal to the standard deviation between the two cases:

$$E_{k,\#60} = 1.1 \pm 0.2 \text{ eV} \quad (4.13)$$

The same analysis applied to the emittance data taken with cathode №61 yields the following results:

$$\frac{d\epsilon_{th,x}}{d\sigma_x} \approx 1.15 \text{ mrad} \Rightarrow E_k \approx 1.0 \text{ eV}; \quad \frac{d\epsilon_{th,y}}{d\sigma_y} \approx 1.0 \text{ mrad} \Rightarrow E_k \approx 0.7 \text{ eV} \quad (4.14)$$

And the final result for cathode №61:

$$E_{k,\#61} = 0.9 \pm 0.2 \text{ eV} \quad (4.15)$$

In general the thermal emittance is correlated with the quantum efficiency of the photocathode. Taking into account the investigations of Spicer[40] and

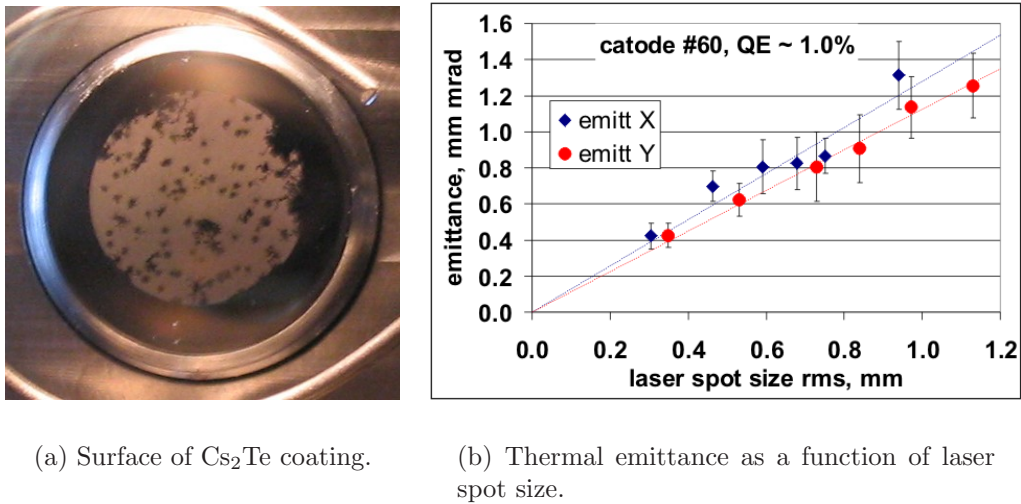


Figure 4.6: Measurements with cathode N°60.

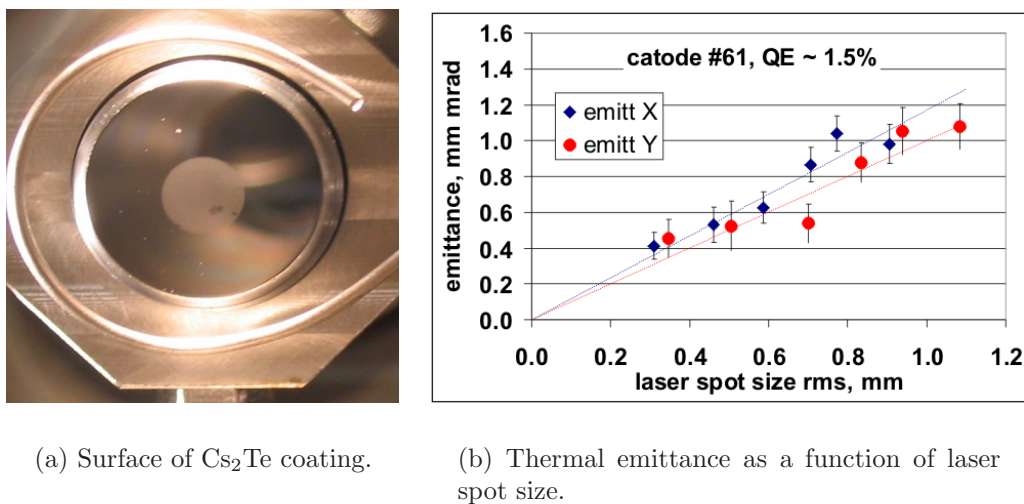
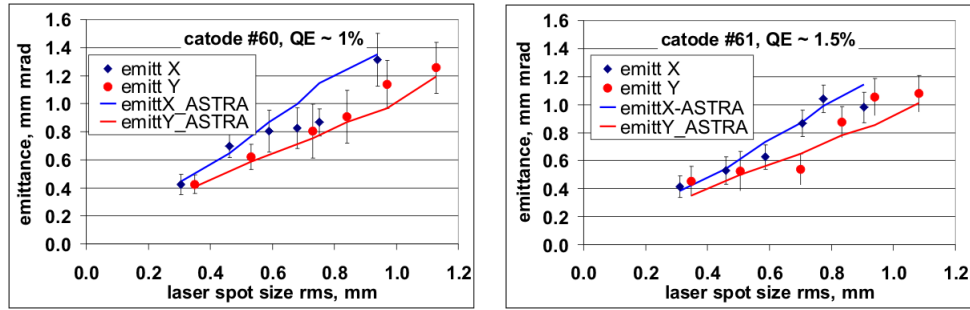


Figure 4.7: Measurements with cathode N°61

Eq.4.9, Eq.4.10, it follows that the thermal emittance increases with QE. The cathode surface roughness has also an impact on the emission process. On a microscopic level the cathode surface (see for example Fig.4.6(a)) can be damaged by dark current and ion back bombardment. The surface irregularities result in variations in the surface electric field. The ratio between the microscopic electric field to that of an ideal planar surface, the so called field enhancement factor[44], can reach a value of 3 or larger. On the other

hand, due to the Schottky effect, the quantum efficiency scales up with the electric field. These arguments suggest that the thermal emittance as well as the mean energy of the photoemitted electrons should be individual for each cathode. However, as apparent from Eq.4.13 and Eq.4.15, a precision better than 0.2 eV is needed, in order to resolve the cathode-specific differences in E_k . Figure 4.8 shows a comparison between measured and simulated emittances.



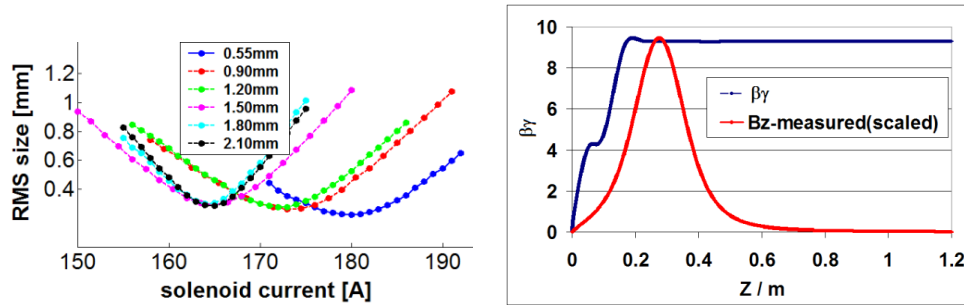
(a) Cathode №60: measurements are compared with simulation, whereat E_k is as determined in Eq.4.13.

(b) Cathode №61: measurements are compared with simulation, whereat E_k is as determined in Eq.4.15.

Figure 4.8: ASTRA simulation results are compared to measured data.

tance. The simulation assumes E_k as given in Eq. 4.13 and Eq.4.15. Another series of thermal emittance measurements has been done with cathode №60 at lower accelerating gradient and using a different technique - the solenoid scan method to determine the emittance. The beam size was measured at screen EMSY (1.62m after the cathode) as a function of the main solenoid current at a max. gradient of about 26 MV/m and a charge of 6 pC. The solenoid scan data are plotted in Fig. 4.9 a. The laser pulse length was about the same as for the previously presented data - 3 ps rms. Such scans were done for different laser spot sizes corresponding to diaphragms of {0.55, 0.90, 1.20, 1.50, 1.80, 2.10} mm diameter. The idea is to evaluate the emittance using these solenoid scan measurements for each diaphragm size. However the solenoid field extends far into the rf gun (Fig. 4.9 b) and moreover due to the higher charge of 6 pC the space charge effects can not be neglected. Therefore the analysis of the solenoid scan data was done with ASTRA code, which takes into account the evolution of beam energy along the magnetic axis as well as space charge and rf effects. The result of the analysis represents the thermal emittance value, which used as input to the simulation, yields the best agreement between the simulated and the measured solenoid scan

data. Table 4.1 shows E_k and ϵ_{th} obtained with the help of ASTRA code, for a bunch charge of 6 pC and an accelerating gradient of about 26 MV/m. The solenoid scan measurements yield about the same kinetic energy as the slit technique.



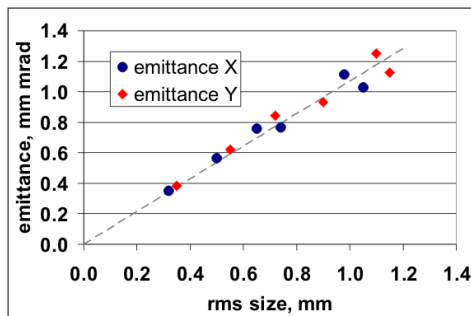
(a) Beam rms size is measured vs. main solenoid current for various shaping aperture diameters.

(b) Magnetic and electric field overlap inside the gun.

Figure 4.9: Analysis of solenoid scan data has to take into account space charge as well as change in solenoid focusing strength as beam accelerates.

Table 4.1: The average kinetic energy of the emitted photoelectrons (left). The plot on the right shows the x- and y- emittance, which used as input to ASTRA, yields the best agreement between the simulated and the measured solenoid scan data.

D [mm]	E_k [eV]	$\epsilon_{th,x}$ [μm]	$\epsilon_{th,y}$ [μm]
0.55	0.93	0.35	0.39
0.90	0.98	0.56	0.62
1.20	1.05	0.76	0.84
1.50	0.82	0.77	0.93
1.80	0.99	1.11	1.25
2.10	0.74	1.03	1.13
$E_k = 0.9 \pm 0.1 \text{ eV}$			



4.5 Thermal emittance dependence on electric rf field

4.5.1 Introduction.

It was experimentally verified that the photo emission from Cs₂Te cathodes is a field assisted process[45, 46], where the quantum efficiency (QE) increases with the electric field strength applied at the cathode. The field enhancement of the QE can be well understood in terms of the so-called Schottky effect, a lowering of the potential barrier by the applied rf field and thereby an increasing of the escape probability of electrons from a photo emissive layer. The reduction of the potential barrier due to the Schottky effect for a metal cathode, caused by the electric field E_0 in an rf gun is given by[47]:

$$\Delta\Phi = e\sqrt{\frac{eE_0}{4\pi\epsilon_0}} \quad (4.16)$$

In this case, the form of the potential barrier is determined by the interaction of an electron with its electric mirror charge. The nature of the electron affinity for dielectric semiconductors like cesium telluride is similar to that of metals: it is due to the interaction of an electron with its image charge due to the medium polarization. Then the reduction of the electron affinity due to the Schottky effect for a semiconductor photocathode with ideal planar surface is described by the following expression[48] :

$$\Delta E_A = e\sqrt{\frac{\epsilon - 1}{\epsilon + 1} \frac{eE_0}{4\pi\epsilon_0}} \quad (4.17)$$

where ϵ is the high-frequency dielectric constant of the photocathode material.

As shown in the previous section, (see Fig. 4.6 a), in reality, the cathode surface is neither planar nor clean, which results in large variations in the microscopic surface field. This local field variation is quantitatively described by the so-called field enhancement factor[44]:

$$\beta_{local} \equiv \frac{E_m}{E} \quad (4.18)$$

where E_m denotes the electric field at the surface irregularity and E is the field corresponding to an ideal surface. In terms of the field enhancement factor Eq. 4.17 can be rewritten in the following form as suggested in [49] and experimentally verified in [50] :

$$E_A = E_A(0) - e\sqrt{\beta \frac{eE}{4\pi\epsilon_0}} \quad (4.19)$$

with β denoting an effective field enhancement factor (typically $\beta \geq 3$), which for convenience incorporates also the term $(\epsilon - 1)/(\epsilon + 1)$ and $E_A(0)$ is the electron affinity at zero electric field.

In summary from Eq. 4.9, Eq. 4.10 and Eq. 4.19 one expects the following general relation between thermal emittance and applied electric field:

$$\epsilon_{th}^2 = A + B\sqrt{E} \quad (4.20)$$

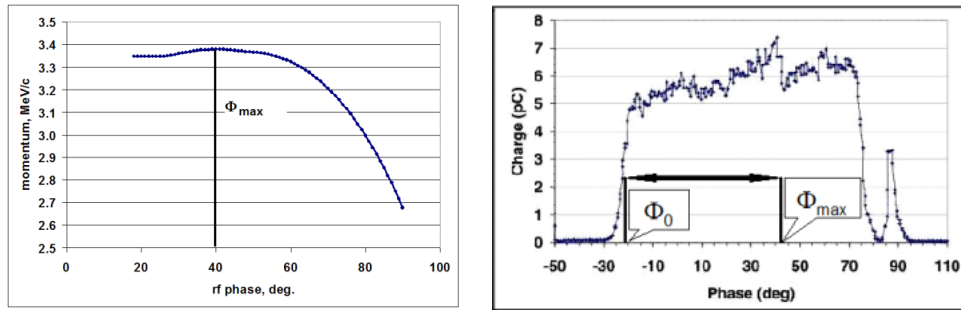
i.e. a linear dependence between the square of thermal emittance and the square root of electric field.

4.5.2 Measurements of thermal emittance vs. electric field

The goal is to study the thermal emittance and hence the average kinetic energy of the photoelectrons as a function of the electric field at the moment of photoemission. The measurements were done using the PITS slit scanning technique. Since the same general requirements for the operation parameters apply as described above in section 4.3, the measurement procedure was as follows:

- The electric field amplitude E_0 was varied in the range of 24 to 39 MV/m
- The diameter of the laser shaping aperture was kept fixed
- Before each emittance measurement the beam charge was measured vs. rf phase. From the rising edge of that scan the phase Φ_0 was determined (see Fig. 4.10 (b)). Φ_0 is the rf phase at the onset of the photoemission.
- For each value of E_0 the rf phase was adjusted to the phase of maximum mean energy gain Φ_{max} (see Fig. 4.10 a)
- The bunch charge was set to 2-3 pC

Following the procedure described above the thermal emittance was measured as a function of the cathode field using cathode №61 with a laser spot size of $\sigma_x=0.46$ mm, $\sigma_y=0.51$ mm. The results presented in Fig. 4.11 show an increasing emittance with the accelerating field. The simulation in the same graph predicts a constant emittance. It includes the beam dynamics in the rf gun, but does not scale the kinetic energy of the emitted electrons with the applied field at the cathode. The same measurements were done with another cathode - №43 with QE of about 3% and then repeated for a



(a) The rf phase Φ_{max} corresponds to maximum mean energy gain

(b) From the rising edge of the phase scan a zero crossing phase Φ_0 was determined

Figure 4.10: Cathode field is determined by: $E = E_0 \sin(\Phi_{max} - \Phi_0)$

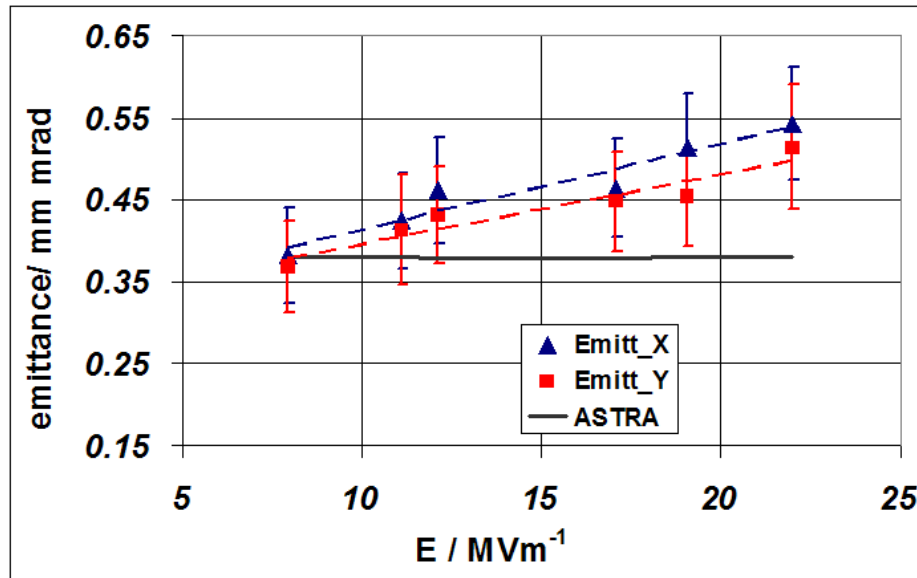


Figure 4.11: Measurements with cathode №61. RF phase set to Φ_{max} . Laser spot size $\sigma_x=0.46$ mm, $\sigma_y=0.51$ mm. The simulation shows a constant emittance, since it does not scale the kinetic energy of the emitted electrons with the applied field at the cathode.

slightly different rf phase corresponding to $\Phi_{max}-5^\circ$. The laser spot size was adjusted to $\sigma_x=0.55$ mm, $\sigma_y=0.54$ mm. Results of these measurements are shown in Fig. 4.12. In all cases, the thermal emittance increases with the accelerating field, which corresponds to a rising average kinetic energy of the

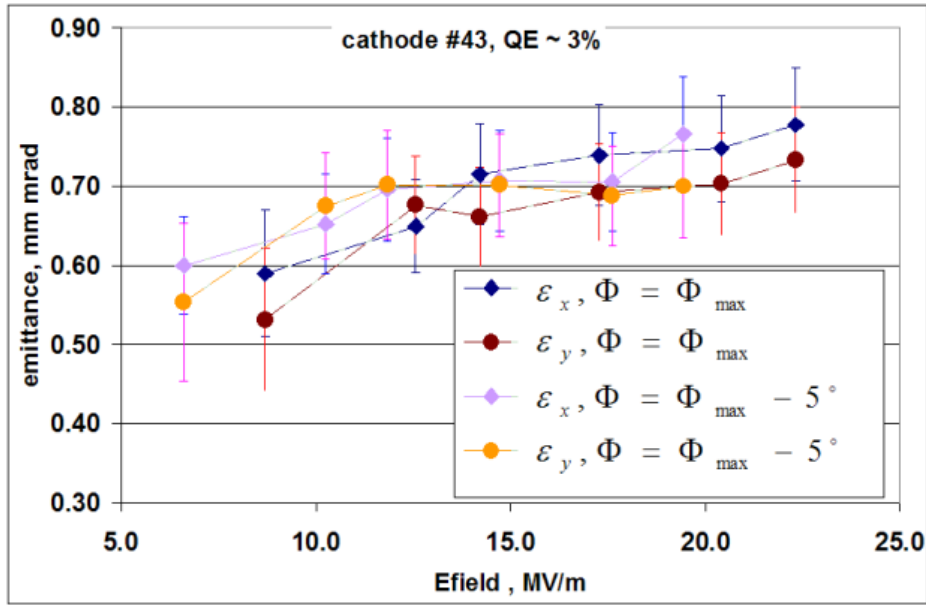
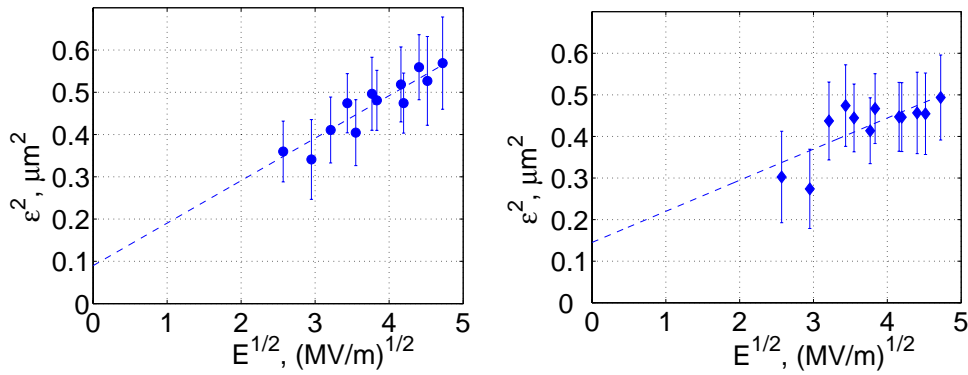


Figure 4.12: Measurements with cathode №43. RF phase set to Φ_{max} and $\Phi_{max}-5^\circ$. Laser spot size $\sigma_x=0.55$ mm, $\sigma_y=0.54$ mm



(a) χ^2 fit of horizontal emittance data yields: $\epsilon_{th,x}^2 = 0.09 + 0.10\sqrt{E}$

(b) χ^2 fit of vertical emittance data yields: $\epsilon_{th,y}^2 = 0.15 + 0.07\sqrt{E}$

Figure 4.13: Measurements plotted in Fig. 4.12 are analyzed using the regression model given in Eq. 4.20.

photoelectrons.

It is well known that the main problem in using semiconductor photocathodes in an rf gun is the relatively short lifetime, compared with metals, due

to contamination caused by residual gases[51]. This photocathode degradation appears as monotonic QE decay with time and can be explained with an electron affinity increase due to passivation of photocathode surface. Therefore the value of electron affinity $E_A=0.2$ eV, quoted in Section 4.2.2, is valid only for a very fresh cathode. During the cathode transportation and rf operation the electron affinity monotonically grows and might reach significantly larger values than the initial one[49]. The photocathodes used in the thermal emittance studies presented above have been stored several months in the photocathode chamber and were also exposed to residual gases in the rf gun. For that reason it is important to give an estimate of their actual electron affinity at the time of the measurements. In order to do this, according to Eq. 4.20, one has to fit a straight line to the square of the measured thermal emittance ϵ_{th}^2 as a function of the square root of the rf field \sqrt{E} . The fit coefficient denoted as A in Eq. 4.20 is related to the actual value of the electron affinity at zero electric field. The replacement of Eq. 4.9, Eq. 4.10 into Eq. 4.19 yields:

$$\epsilon_{th}^2(E) = \sigma_r^2 \left(\frac{2}{3} \cdot \frac{E_{k0} - E_A(0) + e\sqrt{\frac{\beta e}{4\pi\epsilon_0}}\sqrt{E}}{m_0c^2} \right) \quad (4.21)$$

Here $E_{k0} = E_{CB} - E_G = 0.75$ eV is the mean kinetic energy of the photoelectrons in the conduction band. By setting the electric field $E=0$ in Eq. 4.21 one obtains:

$$E_A(0) = E_{k0} - \frac{3}{2} \frac{m_0c^2 \epsilon_{th}^2(0)}{\sigma_r^2} = E_{k0} - \frac{3}{2} \frac{A m_0c^2}{\sigma_r^2} \quad (4.22)$$

where $\epsilon_{th}(0) = \sqrt{A}$ denotes thermal emittance at zero electric field. With these considerations the measured data for cathode №43 were analyzed using the regression model introduced in Eq. 4.20. The results of the straight line χ^2 fits, plotted in Fig. 4.13 (a) and (b), give the following value for A :

$$A = \epsilon_{th}^2(0) = 0.12 \pm 0.04 \mu\text{m}^2 \quad (4.23)$$

and subsequently by replacement in Eq. 4.22:

$$E_A(0) = 0.45 \pm 0.10 \text{ eV} \quad (4.24)$$

The last result is in very good agreement with the value of 0.44 eV [49] obtained by measuring the QE dependence on rf phase. The estimated high value of the electron affinity for cathode №43 (compared to 0.2 eV for a very fresh not yet used cathode) is a clear indication of degradation of the photoemissive layer due to residual gases in the rf cavity.

4.5.3 Summary

The transverse emittance was measured for a very low charge of 2-3 pC, short laser pulses of σ_t about 3 ps and moderate accelerating gradients. According to simulations space charge and rf field contributions to the emittance should be negligible. The scaling of the transverse emittance with the laser spot rms size was measured using the single slit scanning technique as well as the solenoid scan method. Such measurements were performed with different cathodes. A dependence of the thermal emittance on the cathode surface roughness was observed.

The average kinetic energy of the emitted photoelectrons was measured to

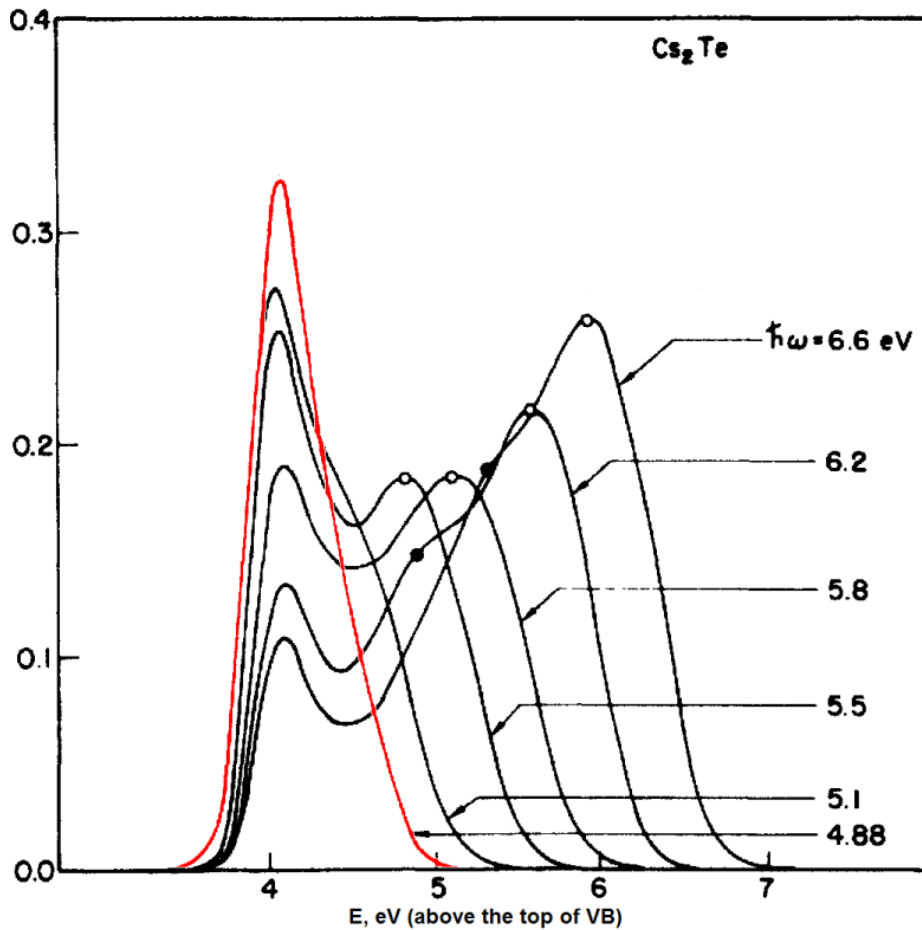


Figure 4.14: Normalized energy distributions of the photoemitted electrons for $4.88 \leq \hbar\omega \leq 6.6$ eV. (from ref.[41])

be in the range 0.9-1.1 eV relative to the vacuum level. The expected value

was about 0.75 eV, where a symmetric energy distribution curve (EDC) of the photoemitted electrons was assumed. The slightly higher experimental result might be assigned to an asymmetry in the EDC, similar to the one measured by Powell[41] for a photon energy $\hbar\omega = 4.88 \text{ eV}$ (see Fig. 4.14). Moreover, due to the electric rf field the probability for optical transition between the valence and the conduction bands increases (Franz-Keldysh effect)[52]. The effective band gap energy reduction can be estimated by the electro-optic energy $\hbar\theta_v \equiv \hbar(e^2 E^2 / 2m_{eff}\hbar)^{1/3} \sim 0.03 \text{ eV}$, taking $E=30\text{MV/m}$ and $m_{eff} = m_0$. This phenomenon might broaden the EDC towards large values and hence contribute to the average energy increase.

The thermal emittance was measured as a function of the applied field at the cathode, where a monotonic increase with electric field due to the Schottky effect was observed. The electron affinity at zero accelerating field was estimated to be $0.45 \pm 0.10 \text{ eV}$ for a cathode with QE of about 3%.

Chapter 5

Transverse emittance study with flat top temporal laser pulse shape

5.1 Impact of the laser pulse temporal profile on the emittance

5.1.1 Introduction

The laser system of PITZ was modified to produce laser pulses with flat top longitudinal profile and typical length in the range 18 – 23 ps FWHM. The modification was realized by installing a pulse shaper between the pulse train oscillator and the first preamplifier. The sketch in Fig. 1.2 a shows the layout of the laser system after the modification. As shown in Fig. 5.1 the obtained profile is not perfectly rectangular, but has a rise/fall time of 4-8 ps and intensity modulation of about 5%. The exchange from gaussian to flat top profile was motivated by the resulting significant reduction of the transverse emittance, which will be demonstrated by the experimental data in the following sections.

This emittance decrease can be well understood when the transverse space charge forces are considered. The space charge emittance growth in the rf cavity starts in the vicinity of the photocathode, where the electrons are still not relativistic and the influence of the defocusing space charge forces on the phase space is significant. The emittance compensation technique[21] cures the emittance increase due to linear space charge force. However the nonlinearities cause phase space distortions, which can not be removed by the emittance compensation scheme[53, 54]. It follows that a reduction of the

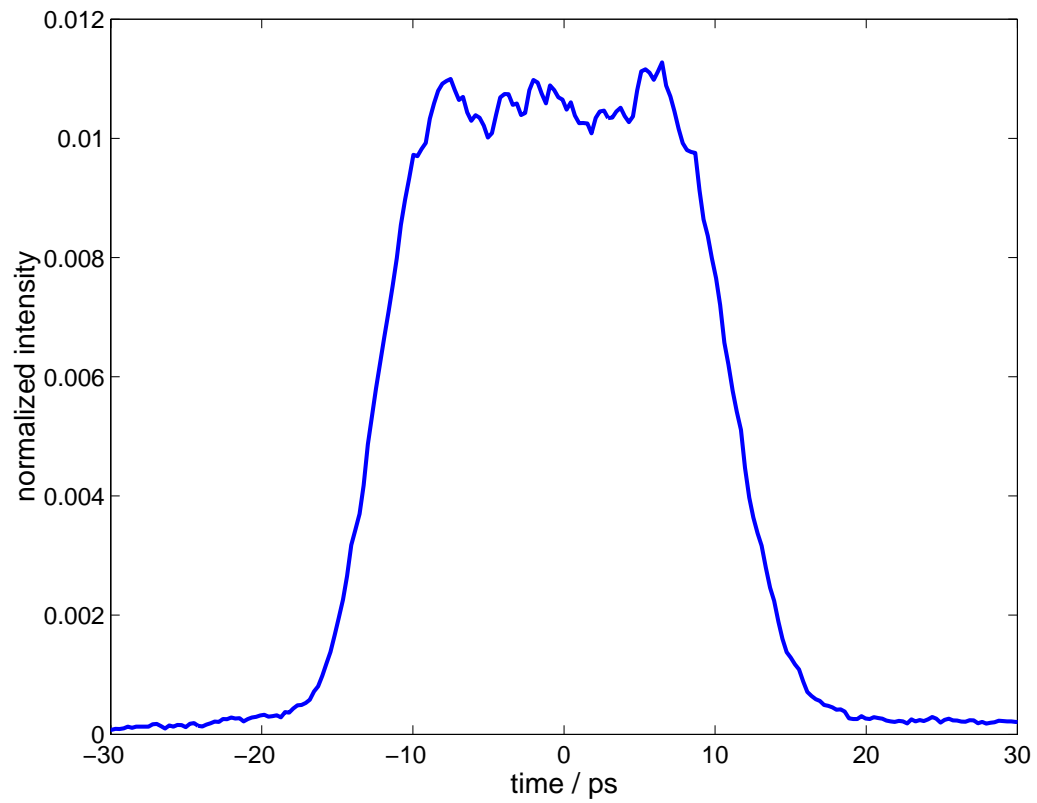
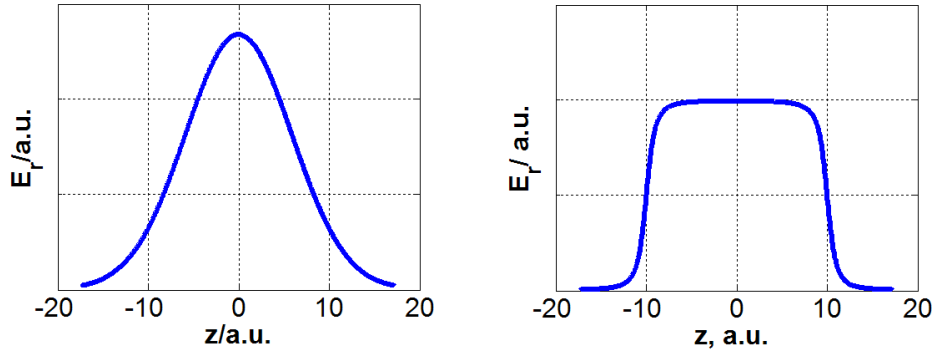


Figure 5.1: Time profile of the flat top laser pulse measured with a streak camera

nonlinear component of the space charge force is needed. The graphs in Fig. 5.2(a) and Fig. 5.2(b) show that the radial space charge fields for the gaussian and for the flat top longitudinal charge distributions differ significantly. As Jones[55] points out, a long slug beam expands self-similarly (due to the linearity of the space charge force) except at the ends, where the non linear effects start to contribute to the beam emittance and moreover in the limit of an infinite bunch length the space charge emittance growth goes to zero. The variation of the defocusing space charge force along the longitudinal axis results in different solutions of the equations of motion for the particles with different z -position. Hence the amplitude of the betatron motion as well as the betatron phase advance $\mu(z, s) = \int_0^s \frac{d\xi}{\beta(z, \xi)}$ will vary along the bunch, being larger for the particles closer to the longitudinal center of the bunch ($z = 0$), where the radial forces are maximum, and smaller at the head and the tail[20].

The spread of the particles in the phase advance introduces a correlation in

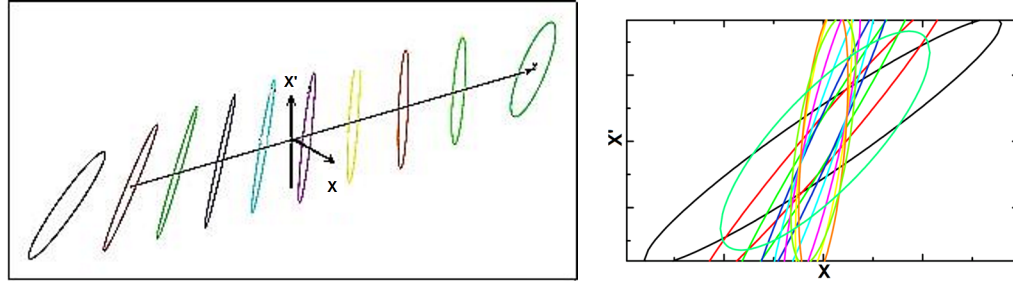


(a) Radial electric field for gaussian charge distribution.

(b) Radial electric field for flat top charge distribution

Figure 5.2: Radial electric field for various z locations for longitudinally gaussian and flat top charge distribution. The rms bunch lengths and the bunch charges are the same in both cases.

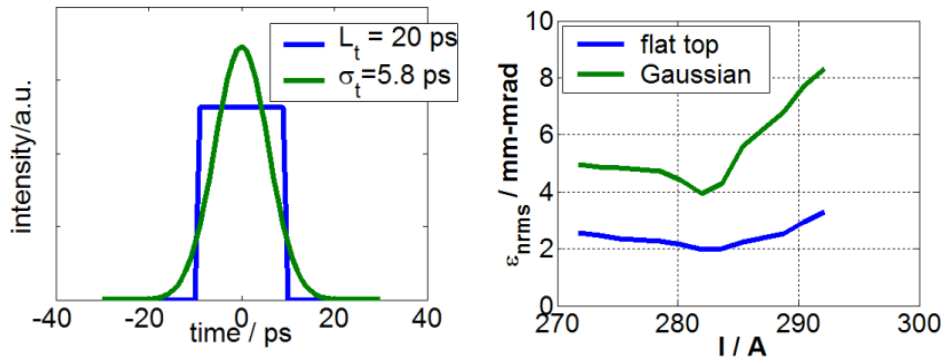
(x, x', z) space, such that when projected to the (x, x') phase space, appears as an emittance increase. This effect can be illustrated by representing the bunch as a set of longitudinal slices like shown in Fig. 5.3(a). Because of the variation of the defocusing space charge force with the z -coordinate, each longitudinal slice will be differently twisted in the (x, x') space. This twisting results in a projected emittance growth, i.e. the total projected area occupied by all the slices in the transverse phase space is larger as presented in Fig. 5.3(b). Since the variation of the transverse space charge force along



(a) Due to a variation of the radial space charge forces along the z -axis, the longitudinal slices are twisted differently in (x, x') phase space

(b) The twisting along the z -axis results in a larger area occupied by the longitudinal slices in (x, x') phase space.

Figure 5.3: Numerical simulation showing the impact of the nonuniform longitudinal charge distribution on the particles spread in the transverse phase space. Considered is a gaussian laser pulse of 6.5 ps FWHM and 1 nC bunch charge.



(a) Two temporal distributions are considered: gaussian with standard deviation $\sigma_t = 5.77$ ps and ideal rectangular pulse of length $L_t = 20$ ps $= \sqrt{12} \cdot \sigma_t$.

(b) Simulation results are shown for the two time profiles. Compared with the gaussian the flat top pulse produces an about twice smaller transverse emittance.

Figure 5.4: Simulations to compare the emittance dependence on longitudinal laser pulse shape. A bunch charge of 1 nC and uniform radial distribution at the photocathode are assumed in both cases.

the z -axis for the gaussian distribution is larger, compared to the flat-top distribution, one expects the emittance in the gaussian case to be larger as well.

5.1.2 Simulation studies

Simulation studies have been done in order to quantify the emittance difference between the gaussian and the flat top profile. Two bunches with the same rms emission time were compared - the first one created by a laser pulse of gaussian temporal distribution with $\sigma_t = 5.77$ ps (see Fig. 5.4a) and the second bunch produced by an ideal rectangular pulse of length $L_t = 20$ ps $= \sqrt{12} \cdot \sigma_t$. A bunch charge of 1 nC and uniform radial distribution at the photocathode were assumed. The simulations were performed for various focusing solenoid currents and the results presented in Fig. 5.4 manifest clearly the benefit of the rectangular pulse shape regarding the approximately twice smaller transverse emittance in the entire solenoid current range. This result is consistent with PARMELA simulations[56] and ISIS studies[55], which also show about a factor two emittance reduction by replacing a gaussian with uniform distribution.

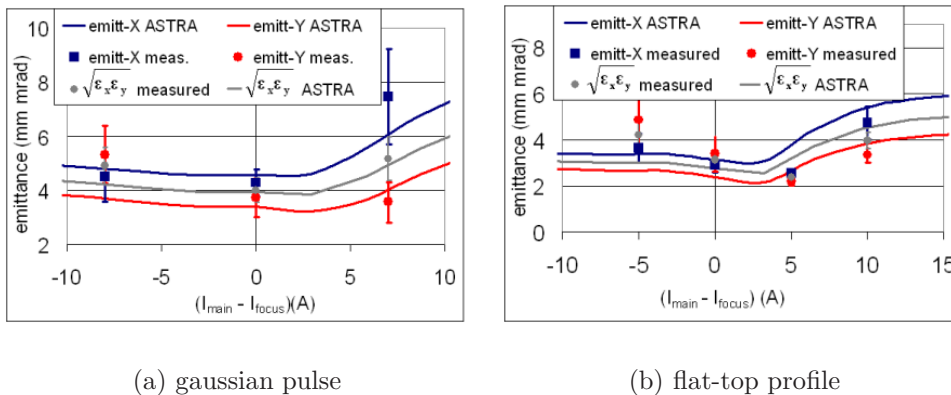
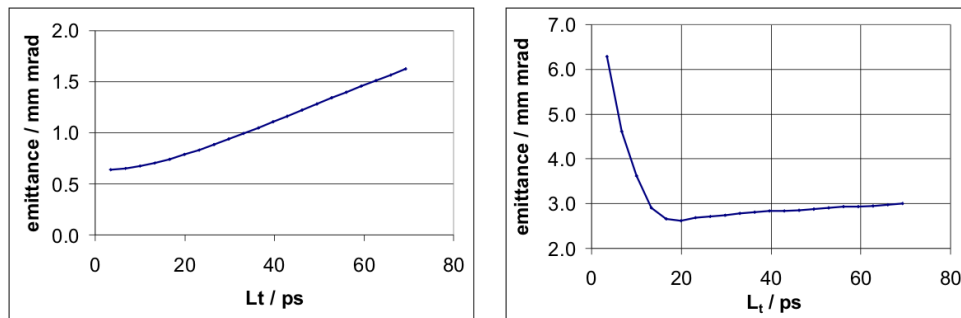


Figure 5.5: Projected normalized emittance as a function of the main solenoid current I_{main} : (a) for a bunch charge of 0.5 nC and a gaussian laser pulse with a length of 6.0 ps FWHM, and (b) for a bunch charge of 1.0 nC and a flat top laser pulse with a length of 23 ps FWHM. I_{focus} denotes the solenoid current to focus the beam on the position of the slit mask. The parameters have not yet been optimized for minimum emittance.

5.1.3 Experimental validation

Finally one can compare the numerical simulation directly with measured data as presented in [57] and shown in Fig. 5.5, where in the left graph the emittance dependence on the solenoid current is displayed for a gaussian pulse of 6 ± 1 ps FWHM and 0.5 nC. The minimal geometrical average $\sqrt{\epsilon_x \epsilon_y}$ is about $4.0 \text{ mm} \cdot \text{mrad}$, but since the emittance scales with the charge, one expects the emittance for the gaussian case at 1 nC to be even larger. The same set of measurements has been repeated with a flat top longitudinal laser pulse profile of 23 ± 1 ps FWHM. The bunch charge was set to 1 nC. The rf phase and rms laser spot size at cathode were the same as for the first solenoid scan. The results together with an ASTRA simulation are plotted in Fig. 5.5(b). The minimal geometrical average of the emittance is about $2.0 \text{ mm} \cdot \text{mrad}$. Since the operating conditions for both solenoid scans are similar, a flat top laser profile yields a more than a factor two smaller emittance than the gaussian profile.



(a) The emittance growth due to rf field scales quadratically with the laser pulse length.

(b) Simulated curve showing the emittance dependence on laser pulse length L_t . The simulation accounts for rf field as well as for space charge effects.

Figure 5.6: The optimal length L_t of a rectangular laser pulse is a balance between at least two counteracting effects - the rf and the space charge emittance growth.

The optimized length L_t of a rectangular laser pulse is determined with respect to the smallest transverse emittance, which the photoinjector can produce. In general L_t is correlated with the other photoinjector parameters like the laser spot size, gun gradient and rf phase. Two counteracting effects have to be taken into account during the optimization of the laser pulse length

- on one hand the rf contribution to the emittance scales quadratically with L_t [19] as shown by simulation in Fig. 5.6(a), which calls for shortest possible laser pulses. On the other hand the space charge term scales with the peak current and hence is inversely proportional to L_t (see Fig. 5.6(b)). As shown in the extended investigations[39], carried out for the optimization of the parameters of the XFEL photoinjector, the smallest emittance is expected to be reached with a laser pulse length of about 20 ps. Since the laser pulses in practice have nonzero rise/fall time r_t , the emittance dilution due to the finite value of r_t should also be taken into account. The rise/fall time have to be minimized and the final goal of the laser development would be to reach rise times as short as 1 – 2 ps[4].

5.2 Simulation study to determine the most sensitive parameters

After the upgrade of the laser system, an extended measurement program was carried out at PITZ in order to characterize and optimize an rf gun cavity for the use at the VUV-FEL at the TTF2 (cavity prototype №2). Later on after the delivery of gun prototype №2 to Hamburg, cavity prototype №1 was installed at PITZ and characterized as well. The goal of the measurements was to define the optimum rf gun operation conditions and to determine the photoinjector parameters minimizing the normalized projected emittance at a nominal bunch charge of 1 nC. The measurements were preceded by numerous simulation studies to estimate the most sensitive machine parameters and their optimal values. For these initial numerical investigations an ideal rectangular time profile of the laser pulse of $L_t = 20$ ps and uniform radial distribution of the laser intensity were assumed. The electric field amplitude E_0 in the cavity should be as high as possible [39] in order to reduce the beam blow up due to space charge forces and therefore a value of 42 MV/m was used in the simulations, as a realistic starting point. In general the optimization of the injector parameters should take into account all contributions to the transverse emittance like the thermal emittance, rf focusing and space charge forces, so that the total projected emittance $\epsilon_n = \sqrt{\epsilon_{th}^2 + \epsilon_{rf}^2 + \epsilon_{sc}^2}$ is as small as possible. Figure 5.7 shows the projected transverse emittance as a function of the launching rf phase Φ and the focusing solenoid current I_{main} for different initial rms sizes σ_r of the UV laser beam on the photocathode. As shown in Fig. 5.7 the laser spot size determines the smallest attainable emittance. On one hand, as derived in Chapter 4 of this thesis, the thermal emittance is proportional to σ_r and the rf field emittance growth

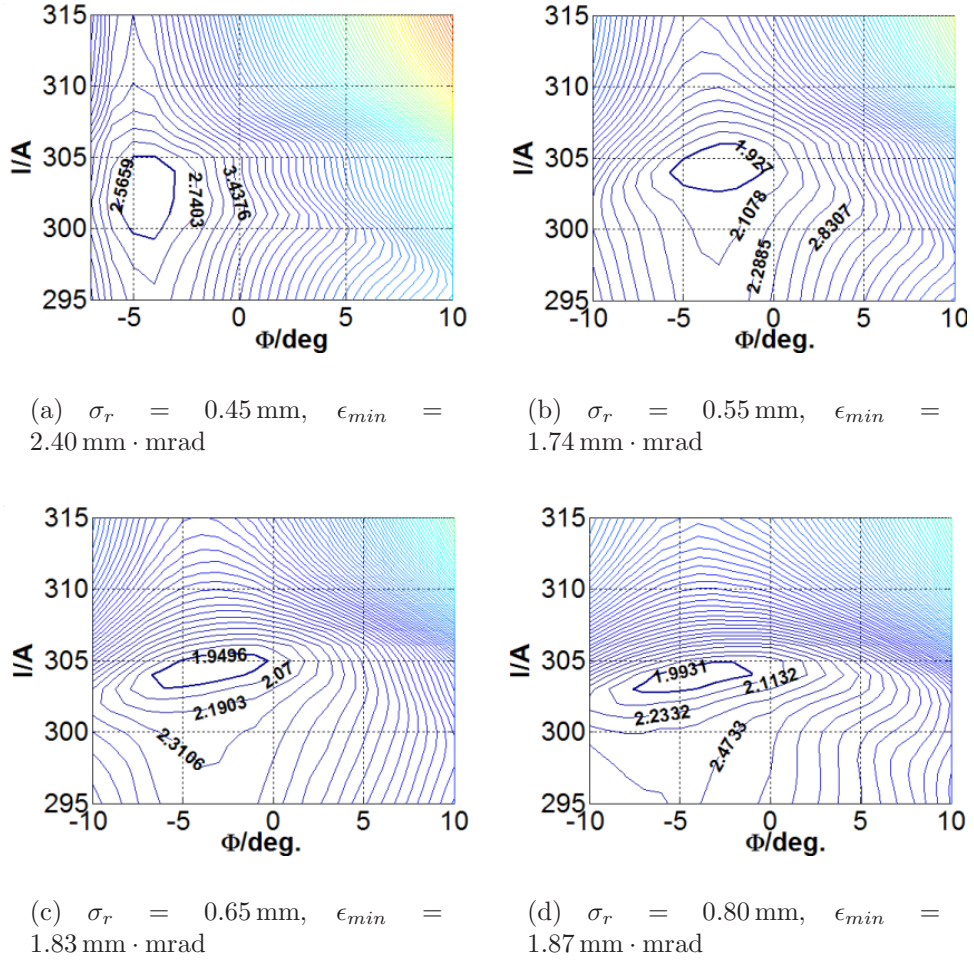


Figure 5.7: Two dimensional transverse emittance scans for various rms laser spot sizes $\sigma_r = [0.45, 0.55, 0.65, 0.80]$ mm. The simulations predict that the emittance reaches a minimum for a certain pair of solenoid current and rf phase $\{I_0, \Phi_0\}$, where $\{I_0, \Phi_0\}$ depend on the laser spot size σ_r .

is proportional to σ_r^2 , which calls for small spot sizes. On the other hand, for reduction of the space charge contribution one needs large σ_r . It follows that by changing the laser beam size one mitigates some of the emittance sources but simultaneously increases the others and therefore the optimal laser beam size has to be determined such that it minimizes the net increase of all terms. The emitted photoelectrons experience a solenoid field all the time during the acceleration in the gun cavity. The magnetic field serves to focus the beam and to compensate the space charge emittance growth by the so called emittance compensation technique invented by Carlsten [21] and described in Chapter 2 of this thesis. The basic idea is to tune the solenoid current I_{main} so that emittance compensation is achieved (see Chapter 2.2 for details). This is equivalent to making the projections of the longitudinal bunch slices onto the (x, x') plane overlap and thus reducing the projected transverse emittance. According to the simulation results plotted in Fig. 5.7, the emittance depends strongly on the solenoid current and within a range of about 10 A around the minimum the emittance value changes by about 20%. The simulations presented in Fig. 5.7 reveal also that the minimal emittance depends strongly on the launching rf phase Φ . This strong correlation is expected since the rf phase determines both the single particle dynamics in the rf cavity as well as the effects related to the collective space charge field of all electrons in the bunch. As derived earlier, each individual particle obtains a transverse kick induced by the rf field at the exit of the gun, on account of what the rf emittance growth ϵ_{rf} has been introduced. Due to the phase dependence of the obtained additional radial momentum one expects that the rf emittance is minimal for a certain launching phase $\Phi < 90^\circ$ corresponding to $\Phi_{\text{exit}} = 90^\circ$ at the gun exit. In contrast, the emittance growth due to the space charge ϵ_{sc} would be minimal if the electrons were emitted close to crest, i.e. for the launching phase $\Phi = 90^\circ$. This is caused by the rapid acceleration at this rf phase and the corresponding reduction of the space charge force. From the theoretical models one expects that ϵ_{sc} is inversely proportional to the accelerating electric field $E(\Phi) = E_0 \cdot \sin(\Phi)$ at the photocathode at the moment of injection. In conclusion, the optimal rf phase balances between the beam degradation determined by single particle dynamics and the emittance dilution due to collective effects.

The solenoid magnetic field, considered so far, is fully compensated at the photocathode position. However if the z -component of the magnetic field B_z^{cathode} is not zero, this will lead to an residual angular momentum of the emitted photoelectrons, proportional to the magnetic flux enclosed by the boundary of the beam, at the cathode. The resulting contribution to the normalized emittance, as derived in Appendix A, is given by the relation: $\epsilon_{\text{magn}} = eB_z^{\text{cathode}}\sigma_r^2/2m_e c$, where σ_r denotes the rms laser beam size on the

cathode, e is the charge and m_e the mass of the electron. The theoretical and experimental investigations performed on the solenoids of PITZ[58] show that the longitudinal magnetic field at the cathode position created solely by the main solenoid is of the order of 8 – 10 mT for a solenoid current of about 300 A. Applying the formula cited above yields an additional magnetic field induced emittance growth of about $0.9 \text{ mm} \cdot \text{mrad}$, where $\sigma_r = 0.6 \text{ mm}$ has been assumed. Therefore it is possible to reduce the emittance by a careful compensation of the magnetic field at the cathode by means of a bucking coil, which is located upstream behind the cathode plate. Therefore the current through the bucking magnet I_{buck} has also to be considered as a parameter for tuning the beam quality.

The figure of merit to determine the optimal magnitude of the parameters introduced up to now like laser spot size, solenoid current, rf phase and bucking coil current is the smallest reachable emittance. In contrast, there is another group of photoinjector parameters, which have to be adjusted prior to the emittance measurements. One such parameter is the laser spot offset with respect to the electric field axis at the photocathode plane. The result of a misalignment is that the electron bunch is launched with a transverse offset and especially for a low energy beam this creates emittance dilution. This unfavorable effect can be corrected by means of movable mirrors installed in the laser beamline. Since the motion of the mirrors is relative to their initial position and the absolute values of the laser misalignment are not known, a beam-based alignment procedure (BBA) has been developed[59]. The BBA procedure combines measurements of beam position as a function of rf gun parameters, their analysis and calculation of the misalignment correction. A similar alignment procedure has to be performed for the main solenoid, which is mounted on remote controllable movers, because due to fabrication tolerances its geometrical center may not exactly coincide with the magnetic axis .

5.3 Optimisation strategy

The practical approach to find the optimal operation conditions has to take into account the specific details of the measurement set-up. The variation of the laser beam spot size is realized via beam shaping aperture located in the laser room. A number of diaphragms with different diameters in the range of 0.3 – 2.1 mm were used. After each diaphragm exchange it is necessary to adjust the transverse position of the aperture so that the laser intensity distribution stays as close as possible to uniform. Then the longitudinal profile and the rise/fall time of the laser pulses have to be tuned

and subsequently a beam-based alignment has to be performed. All these prerequisites to the emittance measurement are very time consuming and hence a diaphragm exchange should take place only after accomplishing the study of the other sensitive parameters like the rf phase and the solenoid current. Because of the screening effect due to space charge[60] and the Schottky effect[46] the charge varies with the rf phase. Therefore changing the rf phase affects directly not only the beam quality and momentum, but has a definite impact on the extracted charge. On that account, a laser power adjustment would be necessary after each phase manipulation, so that the bunch charge remains constant. Therefore, it is preferable to choose an optimization algorithm that varies the rf phase less frequently than the solenoid current.

With the considerations discussed in Chapter 5.2 in mind and taking into account the details explained above one can imply a possible optimization strategy[61] like illustrated in Fig.5.8. Due to the high dimension of the parameter space, the search for the emittance minimum should take place in steps starting with tuning the most sensitive parameters like solenoid current and rf phase, but keeping the laser spot size at the photocathode fixed. In the beginning the emittance for a bunch charge of 1 nC has to be measured as a function of the main solenoid current I_{main} for the rf phases $\Phi - \Phi_m = \{-10^\circ, -5^\circ, 0^\circ, +5^\circ, +10^\circ\}$ at the maximum accelerating gradient on the cathode. Here the rf phase Φ_m denotes the phase with maximum mean energy gain. The scanning order is as determined earlier - at first the solenoid current and second the rf phase. In this first optimization step the magnetic field at the photocathode is not compensated by the bucking solenoid. In the third step, the bucking solenoid current I_{buck} has to be fine tuned, for the settings $\{I_{\text{main}}^*, \Phi^*\}$ with the smallest emittance. Last comes the laser diaphragm exchange and re-iteration of the steps one to three. During the measurements, the laser temporal and transverse properties ought to be frequently monitored and adjusted, with the goal to maintain a radially uniform intensity profile and flat top longitudinal shape of about 18 – 23 ps FWHM and an as short as possible rise/fall time.

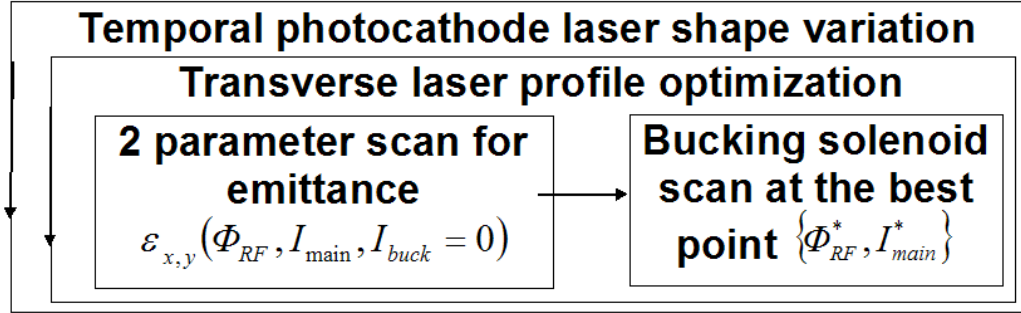


Figure 5.8: The schematic of the optimization strategy is shown. In the inner iteration loop one scans the solenoid current and rf phase. Then follows the tuning of the bucking coil and last comes the shaping aperture exchange.

5.4 Results of the transverse emittance measurements. Comparison with simulations

5.4.1 Variation of the transverse laser beam size

5.4.1.1 Invariant envelope analysis. Operating diagram.

In the following some results of the invariant envelope theory [53], will be applied to the PITZ set up in order to obtain operating diagrams for the laser spot size at the cathode. The considerations below investigate the influence of the repulsive space charge forces on the transverse phase space dynamics, while the effects related to the thermal emittance will be ignored.

The invariant envelope theory regards the bunch as an ensemble of longitudinal slices and the total emittance as an integral over the entire longitudinal ensemble. One should stress that although the emittance of an individual slice, located at a given distance ζ from the bunch center, can be negligibly small, the total emittance might be rather large due to a correlation between the local beam current value $I(\zeta)$ with the phase space angle $\theta(\zeta)$ determined by:

$$\theta(\zeta) = \tan^{-1} \left(\frac{\sigma'(\zeta)}{\sigma(\zeta)} \right) \quad (5.1)$$

There exists a special set of photoinjector operation conditions, which is characterized by all the slices in the final beam state having a constant phase space angle θ , independent of the local current amplitude. This beam propagation mode, called invariant envelope mode, is the basic condition to achieve

the wanted minimum emittance performance of an rf cavity. The gun parameters, necessary to operate a compact photoinjector in invariant envelope regime, can be estimated by analysis of the beam rms envelope equation[14],

$$\sigma'' + K_r \sigma - \frac{\epsilon_n^2}{\sigma^3 \beta^2 \gamma^2} - \frac{P}{4\sigma} = 0 \quad (5.2)$$

which governs the evolution of the transverse rms size σ of a cylindrical symmetric beam passing through a hard-edge solenoid field of amplitude B and focusing strength $K_r = \left(\frac{eB}{2mc\beta\gamma}\right)^2$. Here the generalized perveance $P = 2I/I_0(\beta\gamma)^3$ determines the space charge contribution of the peak beam current denoted by I , $I_0 = ec/r_e \simeq 17 \text{ kA}$ is the Ålfven current and ϵ_n stands for the normalized beam emittance. The derivative is taken with respect to the longitudinal coordinate: $\sigma'' = \frac{d^2}{ds^2}\sigma$. The goal is to define operating conditions for the gun (laser spot size at the cathode σ_r , rf field amplitude E_0) such that there exists an invariant envelope-like solution of Eq.5.2. The last condition implies that the phase space angle θ , given in Eq.5.1 should be independent on space charge forces:

$$\frac{d}{dP}\theta = 0 \Rightarrow \frac{d}{dP}\left(\frac{\sigma'}{\sigma}\right) = 0 \quad (5.3)$$

As it is derived in [53], one can find an approximate solution of Eq.5.2 by applying the condition given by Eq.5.3 and furthermore neglecting the emittance term and taking a constant space charge contribution with a value corresponding to the position at the cavity exit. Skipping the proofs and mathematical derivations, one ends up with the necessary conditions to operate the gun in the invariant envelope mode,

$$\Lambda[kA] \simeq 58.33 - 11.83\alpha + 2.52\alpha^2 + 27.34A - 1.816\alpha A + 1.88A^2 \quad (5.4)$$

expressed in terms of the following quantities:

$$\Lambda \equiv \frac{I}{(\gamma'\sigma_r)^2}, \quad \alpha \equiv \frac{eE_0}{2m_e c^2 k}, \quad k \equiv \frac{2\pi\nu_{rf}}{c}, \quad \gamma' \equiv \alpha k, \quad A \equiv \frac{\sigma_r}{\sigma_z} \quad (5.5)$$

The parameter A is defined as the bunch rms aspect ratio, γ' is the maximal value of the energy gain per unit length, k is the rf wavenumber, α is a dimensionless parameter representing the strength of the accelerating field and Λ is proportional to the peak current density. For the needs of the following considerations it is necessary to quantify the parameters defined in the equations above starting with the aspect ratio $A = \frac{\sigma_r}{\sigma_z}$. As it was

already noted the PITZ laser generates flat-top laser pulses of length L_t in the range 18-23 ps FWHM, hence the rms pulse length σ_z can be estimated by $\sigma_z \simeq \frac{cL_t}{\sqrt{12}} \simeq 1.5 - 2.0$ mm. Usually PITZ operates with an rms spot size at the cathode σ_r bounded in the range of 0.3-1.0 mm, thus the bunch aspect ratio stays in the interval $0.2 < A < 0.7$, but most typically the value is close to 0.3 (assuming $L_t = 20$ ps, $\sigma_r = 0.5$ mm). By substitution in Eq.5.5 and taking into account that PITZ runs at the L-band with $\nu_{rf} = 1.3$ GHz, one obtains for the rf wavenumber $k = 27.2 \text{ m}^{-1}$.

If one considers a uniform temporal charge distribution of length L_t , then the peak beam current will be given by $I[kA] = \frac{Q}{10^3 L_t}$ and the aspect ratio $A = \frac{\sqrt{12}\sigma_r}{cL_t}$. After replacement in Eq. 5.4 and taking into account Eq. 5.5 one obtains the following equation for the laser spot size at the cathode:

$$p_1\sigma_r^4 + p_2\sigma_r^3 + p_3\sigma_r^2 + p_4 = 0 \quad (5.6)$$

with coefficients, which are given by

$$p_1 = \frac{22.56\gamma'^2}{c^2 L_t^2} \quad p_2 = \frac{\gamma'^2(94.71 - 6.29\alpha)}{cL_t} \quad (5.7)$$

$$p_3 = \gamma'^2(58.33 - 11.83\alpha + 2.52\alpha^2) \quad p_4 = -\frac{Q}{10^3 cL_t} \quad (5.8)$$

Solutions of Eq.5.6 were found numerically for various electric field amplitudes E_0 and pulse lengths L_t . Thus one constructs the operating diagram shown in Fig.5.9, which defines the rms laser spot size, needed to operate an injector in invariant envelope mode, as a function of the accelerating gradient. The results will be validated later by comparison with numerical simulations and experimental data. In summary the theory predicts that the optimal transverse laser size is monotonically decreasing with the electric field gradient, a fact assigned to the relativistic diminishing of the space charge force during the acceleration. On the other hand decreasing the pulse length increases the optimal cathode spot size which is needed to minimize the current density needed to operate the injector in emittance compensation regime. The maximal accelerating gradient achieved with the cavity prototype №2 installed at PITZ till autumn 2003 was in the order of 42 MV/m, while with the cavity prototype №1 a higher gradient of about 45 MV/m was reached. According to the operating diagram obtained from theory the optimal cathode spot size $\sigma_r(L_t = 21 \text{ ps})$ should be in the order of 0.7 mm. However since the thermal emittance has been neglected in the derivation of Eq.5.6 the actual optimal value is expected to be somewhat smaller, as shown in Fig. 5.7.

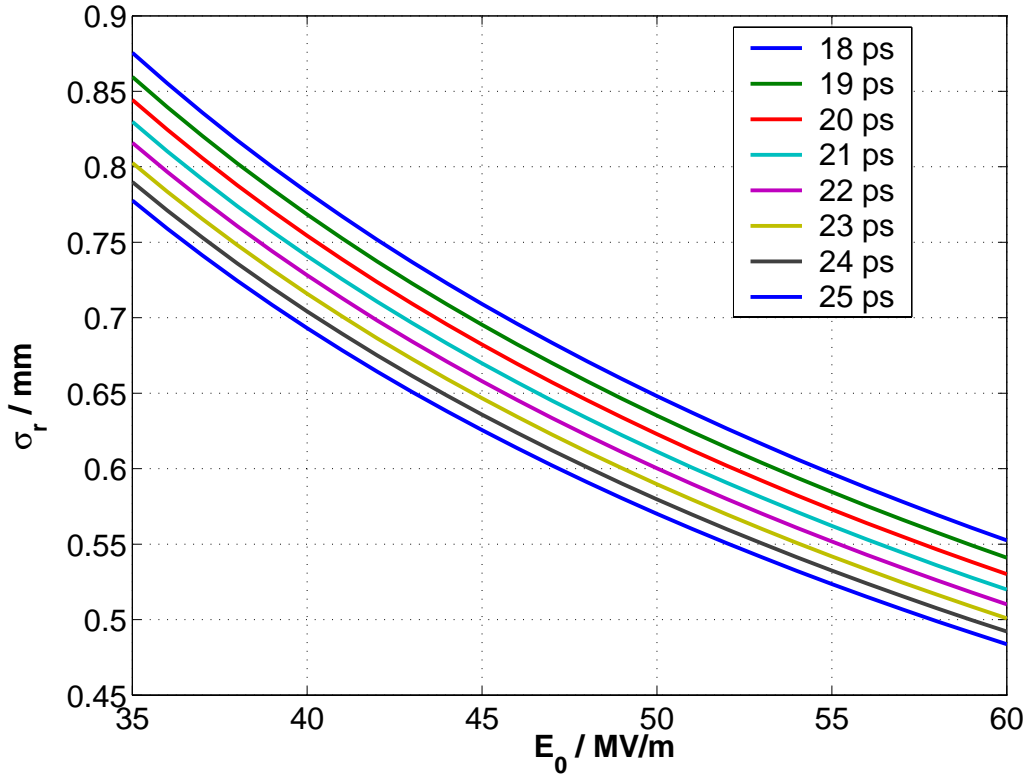
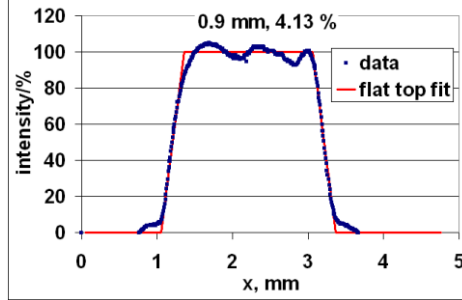


Figure 5.9: Operation diagram derived from Eq. 5.6 for the optimal laser spot size at the cathode as a function of rf field gradient E_0 for various pulse lengths L_t at 1 nC bunch charge.

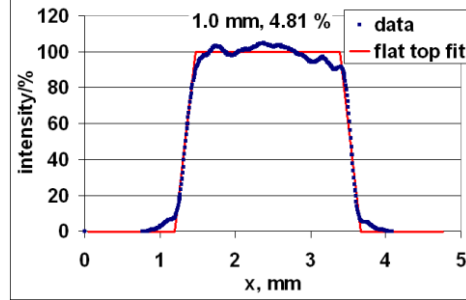
5.4.1.2 Measurements and numerical simulations

The emittance was studied for different laser spot sizes σ_r at the photocathode. For each size the emittance was minimized by adjusting the rf phase and the solenoid current. Such measurements were performed for both cavity prototypes №1 and №2 (see Chapter 1.3). In all cases a maximal rf power was put into the gun and peak field gradients of about 45 MV/m and 42 MV/m were applied respectively. The variation of the laser beam size was realized by passing the initial gaussian beam through a circular aperture with a changeable diameter. In this way a truncated gaussian is created at the diaphragm exit, which is a good approximation of a uniform profile in the case that the aperture diameter is significantly smaller than the size σ_0 of the incoming beam. For an aperture size of the order of σ_0 or larger the nonhomogeneity of the incoming beam starts to affect the overall intensity modulation. The generation of some diffraction effects can not be avoided,

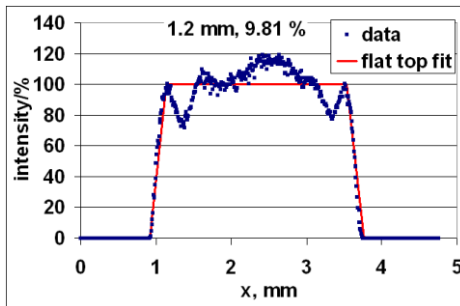
which also contributes to the radial nonuniformity. Fig. 5.10 shows how the measured transverse rms intensity modulation evolves with the diameter D of the shaping aperture. The gun cavity prototype N^o2 was character-



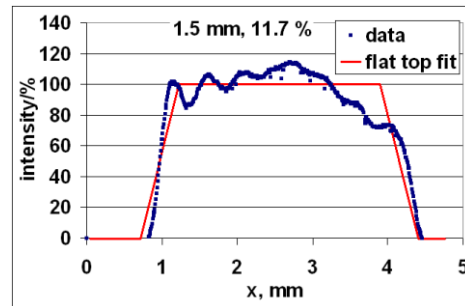
(a) $D = 0.90$ mm, modulation rms = 4.13%



(b) $D = 1.00$ mm, modulation rms = 4.81%



(c) $D = 1.20$ mm, modulation rms = 9.81%



(d) $D = 1.50$ mm, modulation rms = 11.7%

Figure 5.10: Intensity distribution and the corresponding intensity modulation along horizontal diametrical slices of the laser beam for various aperture sizes. For comparison the best flat-top fit is plotted as well.

ized using shaping apertures of diameter $D=\{0.9, 1.0, 1.2\}$ mm (full list of operation conditions is given in Appendix B, tables 5.3, 5.4, 5.5). In Fig.5.11 these measurements are summarized and compared with ASTRA simulations. The simulations were performed by scanning the rms size of a round laser beam in the range 0.45 to 0.80 mm with a step size of 0.05 mm and assuming a laser pulse length of 18 ps FWHM, a rise time of 4 ps and a peak accelerating gradient of 42.3 MV/m. In the summary plot the geometrical average $\sqrt{\epsilon_x \epsilon_y}$ was taken as a measure for the transverse beam emittance as well as the geometrical average $\sqrt{\sigma_x \sigma_y}$ as a measure for the

transverse laser beam size. A number of conclusions can be drawn comparing the measured data, the numerical simulations and the theoretical curves introduced in Fig.5.9. According to the numerical simulation the optimal laser spot size $\sigma_{opt} \approx 0.55$ mm is smaller than the one predicted from Eq.5.6. The difference of about 0.15 mm rms is due to the contribution of the ther-

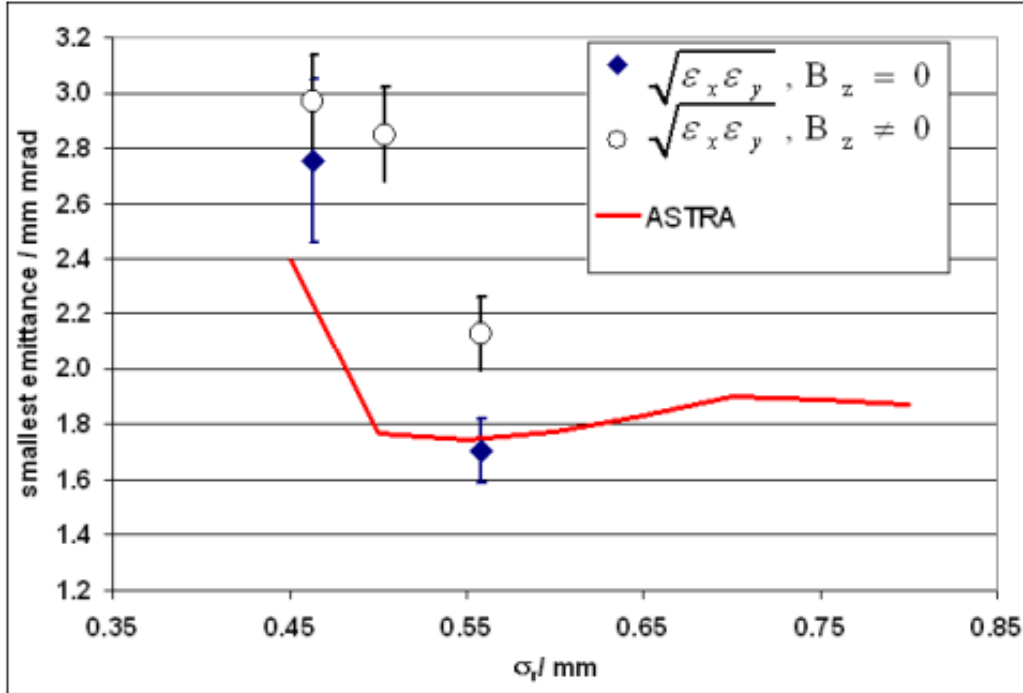


Figure 5.11: Measured data (summary of all measurements in 2003) and simulation for the minimal achievable emittance as a function of the laser beam size at the photocathode.

mal emittance, which was not considered in the theoretical derivations. From Eq.4.10 it follows that the thermal emittance ϵ_{th} is directly proportional to the laser spot size at the cathode. If ϵ_{th} is taken into account, then the total emittance $\epsilon_n \approx \sqrt{\epsilon_{th}^2 + \epsilon_{rf}^2 + \epsilon_{sc}^2}$ scales faster with the size of the laser beam. In Fig. 5.11 one notes a difference in the smallest emittance, which was measured without magnetic field compensation which is 2.1 ± 0.2 mm · mrad for $\sigma_r \approx 0.55$ mm and 1.7 ± 0.1 mm · mrad for the same laser spot size, but obtained by compensating the residual solenoid field. Since the magnetic emittance ϵ_{magn} adds up in quadrature to the other emittance terms, one estimates $\epsilon_{magn} \approx 1.2$ mm · mrad. From Eq. 5.38, one can estimate also the noncompensated longitudinal magnetic field at the cathode to be in the or-

der of 10 mT. As shown in Fig. 5.11 the emittance has been experimentally studied only in a limited range of laser beam sizes, where a close to uniform transverse profile (modulation rms $\leq 10\%$) could be obtained. The addi-

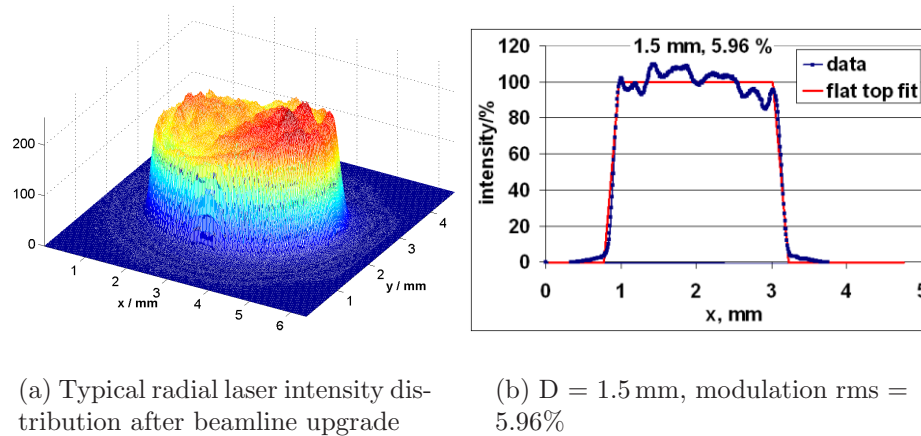


Figure 5.12: Typical intensity distribution (a) and the intensity distribution along a horizontal diametrical slice the laser spot (b) after the laser beamline upgrade in 2004.

tional emittance growth induced by transversely nonuniform space charge distribution is direct proportional to the laser beam nonuniformity [62] and therefore the laser beam transverse homogeneity is a key issue for further improving the beam quality. In early 2004 the PITZ laser and laser beamline were upgraded to create a radial flat-top beam shape at the cathode and as a result of the improved imaging (see Fig. 5.12) the typical intensity modulation has been reduced to well below 10% even for large diaphragm diameters. This made it possible to consistently carry out the characterization of the next installed cavity prototype №1 with an even larger variety of apertures of diameter $D = \{1.2, 1.5, 1.8\}$ mm (the full list of operation conditions is given in tables 5.6, 5.7, 5.8). This gun cavity was operated [63] with a peak power of about 4 MW, corresponding to a maximum mean momentum of about 5.2 MeV/c. The graph in Fig. 5.13 shows a comparison between the minimal measured emittance for cavity №1 as a function of the cathode spot size and simulations. The simulations were performed by scanning the rms size of an round laser beam in the range 0.45 to 0.80 mm with a step of 0.05 mm and assuming a laser pulse length of 18 ps FWHM, a rise time of 4 ps and a peak accelerating gradient of 45.8 MV/m. The measurements presented in Fig. 5.13 were done following the same strategy as described in

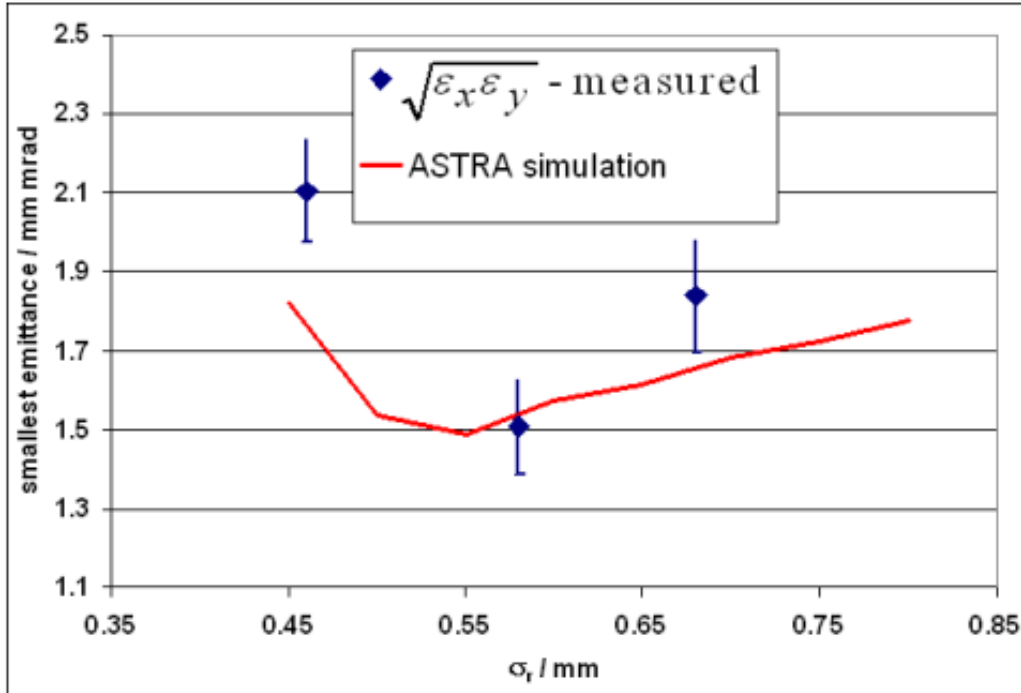


Figure 5.13: Measured data (summary of all measurements in 2004) and simulations for the minimal achievable emittance as a function of the laser beam size at the photocathode are shown for gun prototype №1 at 1 nC.

Section 5.3, but the remnant solenoid field at the cathode was compensated with the bucking coil in all cases. A geometrical average emittance $\sqrt{\epsilon_x \epsilon_y}$ of about 1.5 ± 0.1 mm · mrad was achieved. Results like this were expected for two reasons - first the electric field amplitude was higher, which leads to a faster diminishing of the space charge force and second the laser profile was closer to flat top, which reduces the emittance growth due to nonhomogenous charge distribution.

5.4.2 Variation of the focussing solenoid field

5.4.2.1 Introduction

The PITZ photoinjector belongs to the class of electron sources capable of producing electron beams of very high brightness ($B_n \sim 10^{14}$ A · m⁻² · rad⁻²). The generated electron bunch inherits the time structure and the spatial extent of the driving laser pulse, which leads to a very large space charge density and strong space charge interactions. Consequently, the beam particles gain

additional transverse momentum, which finally increases the emittance. Such effects are the major contributors to the emittance when a photoinjector is operated in the space charge dominated regime, therefore they have been studied in numerous theoretical and experimental works. Some theoretical treatments give rather pessimistic estimations for the space charge emittance growth. Kim[19] for example, considering a cylindrical bunch of radius r and length cL_t , derives:

$$\epsilon_{n,sc} \simeq \frac{\pi m_e c^2 I}{2.8 e E_0 I_A} \frac{1}{\left(3 \frac{r}{L_t c} + 5\right)} \simeq 5 - 10 \text{ mm} \cdot \text{mrad} \quad (5.9)$$

Here $I_A = \frac{ec}{r_e} \approx 17000 \text{ A}$, $I \simeq 50 - 100 \text{ A}$ denotes the peak current at a bunch charge of 1 nC , $L_t = 20 \text{ ps}$ and $r = 0.5 \text{ mm}$ have been assumed. In that model the emittance is monotonically increasing along the beam propagation direction. In contrast, Carlsten suggested[21] that the emittance growth induced by the linear component of the self field can be compensated by means of a solenoid lens located in the vicinity of the rf gun (see Section 2.2.3). The potential to reduce the transverse emittance by means of an external solenoid field were experimentally studied at PITZ. In the following the results of these studies will be presented and compared with theoretical models and multiparticle simulations.

5.4.2.2 Invariant envelope analysis of the PITZ set up

The theoretical models, compared to the numerical simulations, give approximate solutions for the performance of a photoinjector, but on the other hand the simulations are more time consuming compared to the analytical approach. Therefore it is interesting, for validation, to determine the optimal operation conditions of PITZ through the emittance compensation theory and to compare the outcome with the experimental data. The goal is to construct an operation diagram of the same type as that in Fig. 5.9. Following the model already introduced in [53], the optimal magnetic field amplitude can be determined in terms of the dimensionless field strength amplitude α defined in Eq. 5.5 and the magnetic-to-rf focusing ratio:

$$b = \frac{c B_{z,0,HE}}{E_0} \quad (5.10)$$

Here $B_{z,0,HE}$ is the field amplitude of a hard edge solenoid field (see Fig. 5.14), which begins at $z_b = \lambda/2$ and ends at $z_e = \frac{7}{4}\lambda$, where $\lambda = c/\nu_{rf} \approx 0.23 \text{ m}$ is the rf wavelength. The optimal value of b is approximately given by the relation [53]:

$$b \approx 1.38 + \frac{1.52}{\sqrt{\alpha}} - \frac{1.86}{\alpha^{1/4}} \quad (5.11)$$

However, the expression above cannot be directly applied to determine the

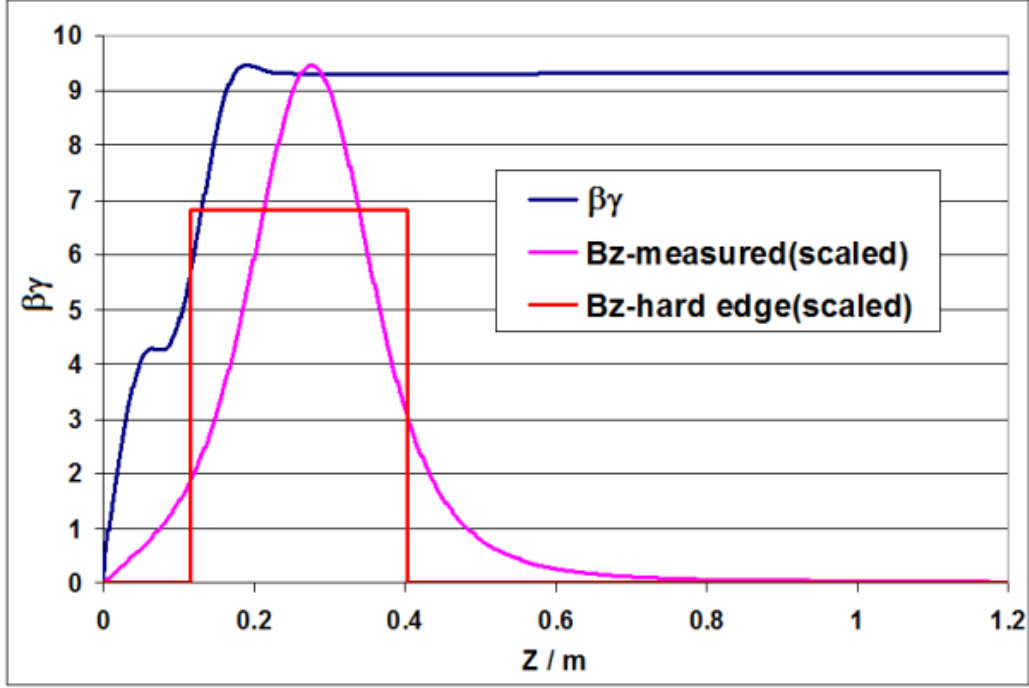


Figure 5.14: Evolution of $\beta\gamma$ as obtained from simulation and put together with the measured and the hard-edge B_z profiles.

optimal magnetic field amplitude and the current through the main solenoid installed at PITZ. The reason is that Eq. 5.11 considers the amplitude $B_{z,0,HE}$ of a hard edge solenoid, which means its longitudinal magnetic profile $B_{z,HE}$ differs from the actual measured one $B_{z,meas.}$ as plotted in Fig. 5.14. Also is shown how the magnetic field extends far into the cavity in the region where the beam momentum increases quickly along the z -axis and therefore the change in the focusing strength with $\beta\gamma$ has to be taken into account when comparing both peak field values $B_{z,0,HE}$ and $B_{z,0,meas.}$. Assuming the thin lens approximation is valid, a rough relation between $B_{z,0,HE}$ and $B_{z,0,meas.}$ can be derived by equalizing the optical strengths of the solenoid lens for the two cases:

$$\frac{1}{f_{HE}} \approx \frac{e^2 B_{z,0,HE}^2 L_{eff,HE}}{(2m_e c \beta_0 \gamma_0)^2} = \frac{1}{f_{meas}} \approx \frac{e^2 B_{z,0,meas}^2 L_{eff,meas}}{(2m_e c \beta_0 \gamma_0)^2} \quad (5.12)$$

$$B_{z,0,meas} = B_{z,0,HE} \sqrt{\frac{L_{eff,HE}}{L_{eff,meas}}} \quad (5.13)$$

Here $L_{eff,HE}$ and $L_{eff,meas}$ denote the effective solenoid length for the hard-edge approximation and for the actual profile, $\beta_0\gamma_0$ correspond to the final energy at the gun exit. The effective length should be determined considering the evolution of the beam momentum:

$$L_{eff} = \frac{\beta_0^2\gamma_0^2}{B_{z,0}^2} \int_0^\infty \frac{B_z(z)^2}{\beta(z)^2\gamma(z)^2} dz \quad (5.14)$$

A numerical integration of Eq. 5.14 yields the following values for the effective solenoid length:

$$L_{eff,HE} = 0.331 \text{ m}, \quad L_{eff,meas} = 0.156 \text{ m} \quad (5.15)$$

Finally after a substitution of Eq. 5.15 in Eq. 5.13 one obtains:

$$B_{z,0,meas} = B_{z,0,HE} \sqrt{\frac{L_{eff,HE}}{L_{eff,meas}}} = 1.46 B_{z,0,HE} \quad (5.16)$$

The formula above was derived under the assumption that the thin lens approximation is valid, i.e. if Φ is the image rotation angle given by:

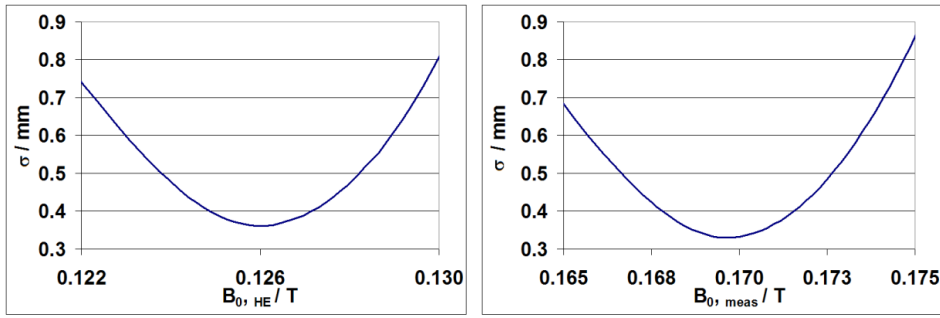
$$\Phi = \frac{eB_0 L_{eff}}{2m_e c \beta_0 \gamma_0} \quad (5.17)$$

then $\sin(\Phi) \approx \Phi$ should be fulfilled for both of the considered magnetic field profiles. But evaluation of Eq. 5.17 yields $\Phi \sim 1$ rad, which implies a deviation from the thin lens model. A more accurate estimation for the ratio $B_{z,0,HE}/B_{z,0,meas}$ can be obtained by numerical simulations of the variation of the electron beam size vs. solenoid peak field for both magnetic distributions. In Fig. 5.15 the results of such numerical investigations are shown, where in the left graph the tracking was done using the hard-edge longitudinal profile and in the right plot the actual magnetic field distribution was used. Taking the two peak fields to focus the beam, that are 0.170 T from the right plot and 0.126 T for the hard-edge model, yields

$$B_{z,0,meas} \approx 1.35 B_{z,0,HE} \quad (5.18)$$

Replacing $B_{z,0,HE}$ in Eq. 5.10 with Eq. 5.18 gives the condition to operate PITZ in a regime to minimize the projected beam emittance at about the beam waist position. These optimal conditions are expressed in terms of the main solenoid field amplitude vs. peak rf gradient E_0 as follows:

$$B_{z,0} \approx 1.86 \frac{E_0}{c} + 2.05 \sqrt{\frac{2m_e k E_0}{e}} - 2.51 \sqrt[4]{\frac{2m_e k E_0^3}{ec^2}} \quad (5.19)$$



(a) Hard-edge solenoid approximation

(b) Actual magnetic longitudinal profile

Figure 5.15: Simulations with ASTRA for the beam size dependence on solenoid field amplitude. Considered are two cases: the hard-edge model (a) and the actual profile (b). The rf phase was set to maximum mean energy gain at a gradient of 42 MV/m. Space charge forces are included in the simulation.

This dependence was plotted in Fig. 5.16, but instead of the magnetic field amplitude vs. rf gradient, the more practical representation of the solenoid current vs. rf gradient was used. The relation between the solenoid current and the magnetic field amplitude is the following[64]: $I_{\text{main}}[\text{A}] \approx 1698.6B_{z,0}[\text{T}]$.

It has to be noted that the operation diagram given by Eq. 5.19 and plotted in Fig 5.16 is coupled with Eq. 5.6 and Fig. 5.9, thus forming the 4D parameter space $\{E_0, I_{\text{main}}, \sigma_r, \sigma_z\}$ considered so far in the phase space optimization of the photoinjector.

5.4.2.3 Measurement results and numerical simulations with cavity prototype №2

Following the discussion in Chapter 5.3, the dependence of the transverse emittance on the solenoid current I_{main} was systematically studied at a bunch charge of 1 nC for various rf phases Φ and shaping aperture diameters ($D=0.9$ mm, 1.0 mm, 1.2 mm). For the points $\{I_{\text{main}}^*, \Phi^*\}$, where the smallest emittance was obtained, additional tuning with the compensating solenoid current I_{buck} was performed. A variation of the laser spot size has been done only after accomplishing the $\{I_{\text{main}}, \Phi\}$ scan. All the measurements of horizontal as well as vertical emittance were performed using a single-slit scan technique[65]. Beamlet profiles were observed 1010 mm downstream of

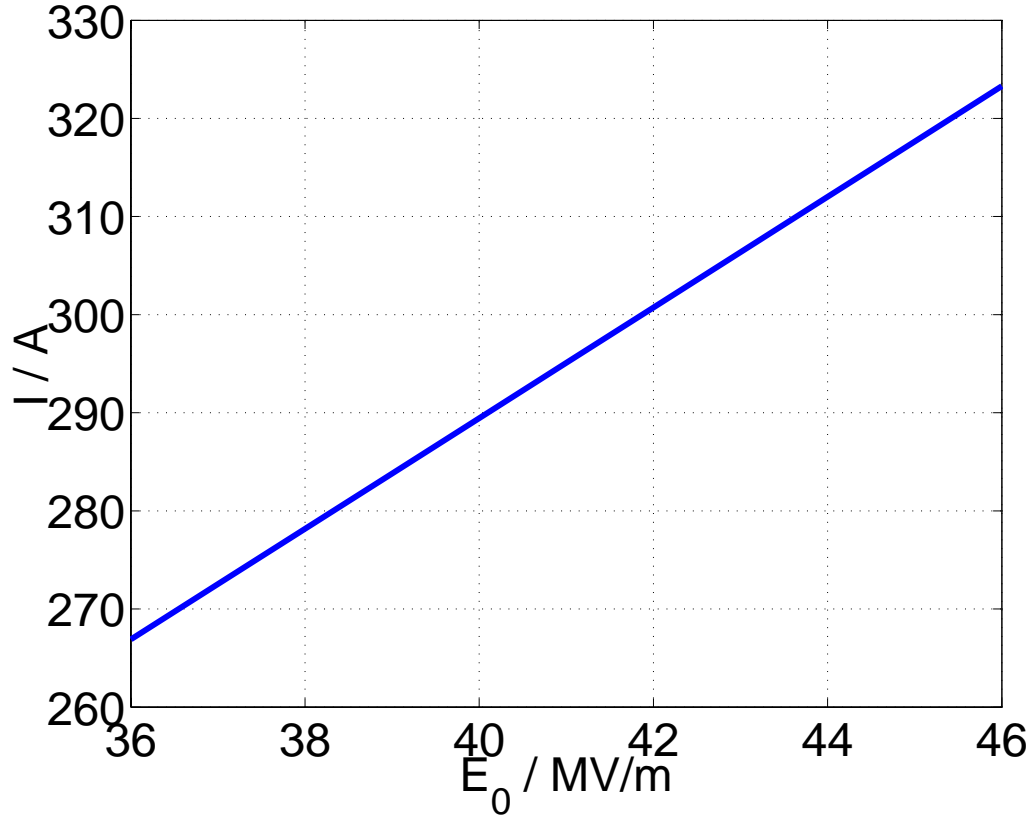
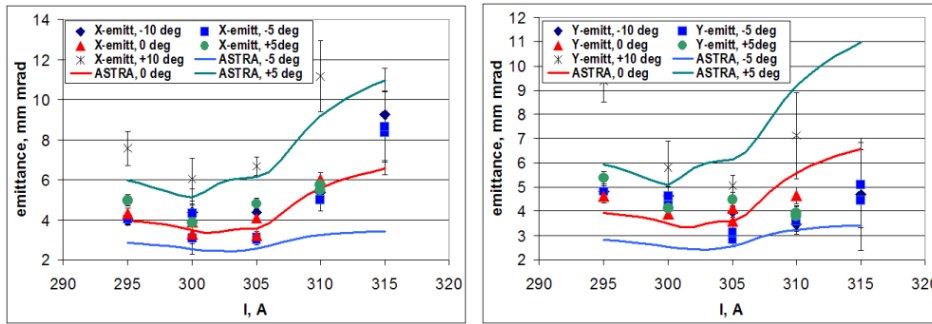


Figure 5.16: Theoretical estimation of the optimal current through the main solenoid at PITZ as a function of the peak accelerating gradient. The curve is calculated from Eq. 5.19 and will be compared with the measured data and simulations in the rest of this chapter.

the single-slit mask (1 mm thick tungsten plate, $50 \mu\text{m}$ slit opening). The beam transverse phase space was sampled at three slit positions separated by a distance $\delta = 0.7\sigma_x$. Here σ_x is the rms electron beam size in the corresponding transverse direction at the position of the slit mask. During the measurements an accelerating gradient of about 42 MV/m was used. Three different apertures for transverse shaping of the laser beam were successively inserted in the laser beamline. The corresponding PITZ operation conditions for these measurements are listed in Appendix B, where Φ_m denotes the rf phase with maximal mean energy gain.

In parallel to the experimental studies, ASTRA simulations were performed for the same solenoid field and rf phase as in the emittance measurements. The results of these simulation studies are plotted together with the measured data in Figures 5.17, 5.18, 5.19. In the simulations a rotationally

symmetric laser beam has been assumed, where the rms laser spot size σ_r was set equal to the geometrical average $\sqrt{\sigma_x\sigma_y}$ of the laser spot sizes measured in both transverse directions. The transverse nonhomogeneity of the laser beam was simulated as a gaussian distribution truncated at $0.7\sigma_r$ from the center, which yields an rms intensity modulation of about 7%. The assumed temporal laser pulse profile was a flat top of 18 ps FWHM and 4 ps rise/fall time. In all simulations the bunch charge was set to 1 nC and the accelerating field to 42.3 MV/m. After accomplishing of the phase space



(a) Horizontal emittance at rf phases $\Phi - \Phi_m = (-10, -5, 0, +5, +10)^\circ$

(b) Vertical emittance at rf phases $\Phi - \Phi_m = (-10, -5, 0, +5, +10)^\circ$

Figure 5.17: Emittance measurements for $D=0.9$ mm compared with ASTRA simulations, at different rf phases and focusing solenoid currents.

characterization for the case $D=0.9$ mm a minimal geometrical average emittance $\sqrt{\epsilon_x\epsilon_y} = 2.8 \pm 0.3$ mm mrad was reached (see Fig. 5.20(a)), where the horizontal emittance was $\epsilon_x = 3.8 \pm 0.6$ mm mrad and the vertical emittance was $\epsilon_y = 2.0 \pm 0.2$ mm mrad. For the case $D=1.2$ mm, $\sqrt{\epsilon_x\epsilon_y} = 1.7 \pm 0.1$ mm mrad was achieved (see Fig. 5.20(b)), where the horizontal emittance was $\epsilon_x = 1.9 \pm 0.2$ mm mrad and the vertical emittance was $\epsilon_y = 1.5 \pm 0.1$ mm mrad. The smallest measured emittance as a function of the main solenoid current is given in Fig. 5.21. The data cover all measurements done with a given fixed magnetic field, where from the measurements with various rf phases, laser spot sizes and bucking coil currents only the minimal emittance values have been taken. Since the characterization of gun cavity prototype N^o2 took place before the laser beam line upgrade (see discussion in Chapter 5.4.1) the laser spot was slightly asymmetric, e.g. for the case of $D=1.2$ mm, where the best transverse emittance was measured the laser spot size was $\sigma_x=0.50-0.52$ mm, $\sigma_y=0.60-0.62$ mm, what might explain the

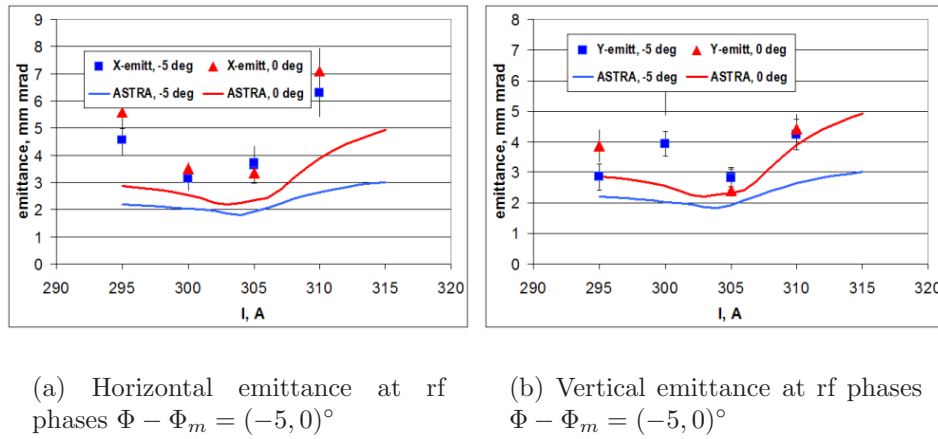


Figure 5.18: Emittance measurements for $D=1.0$ mm compared with ASTRA simulations, at different rf phases and focusing solenoid currents.

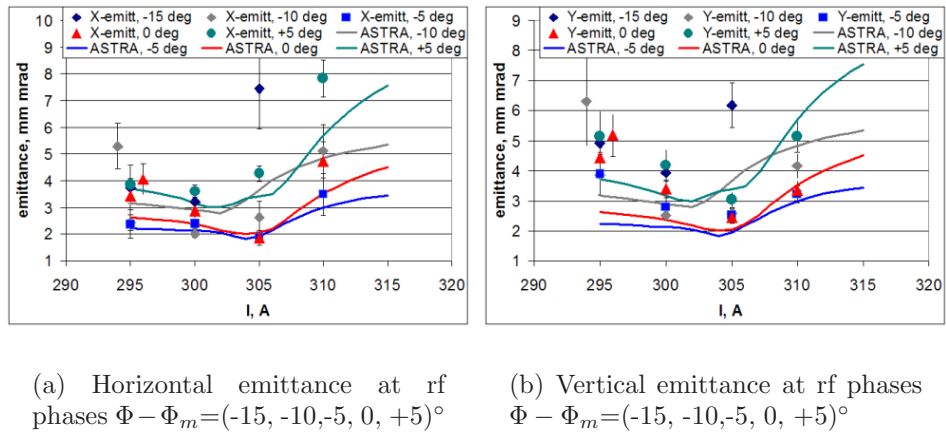
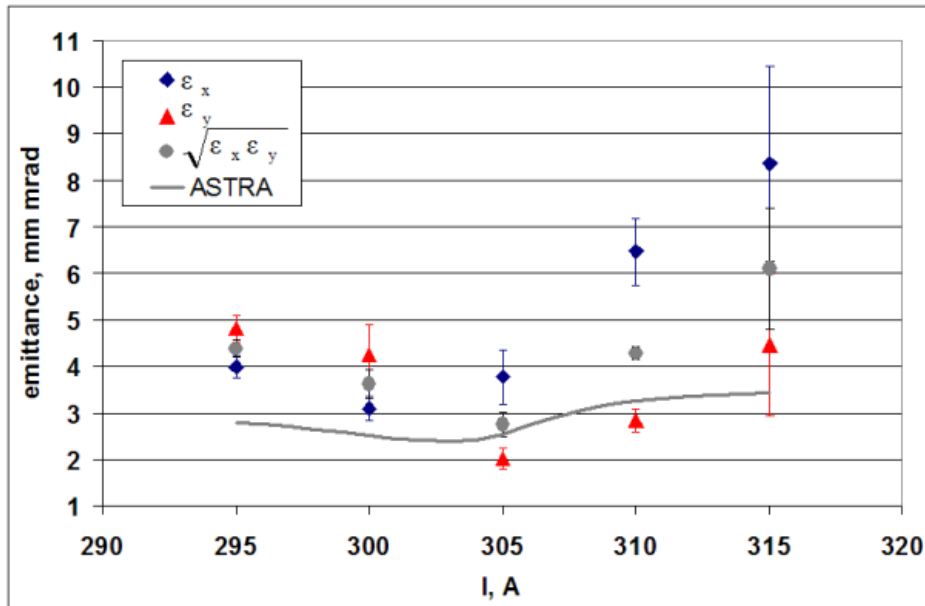
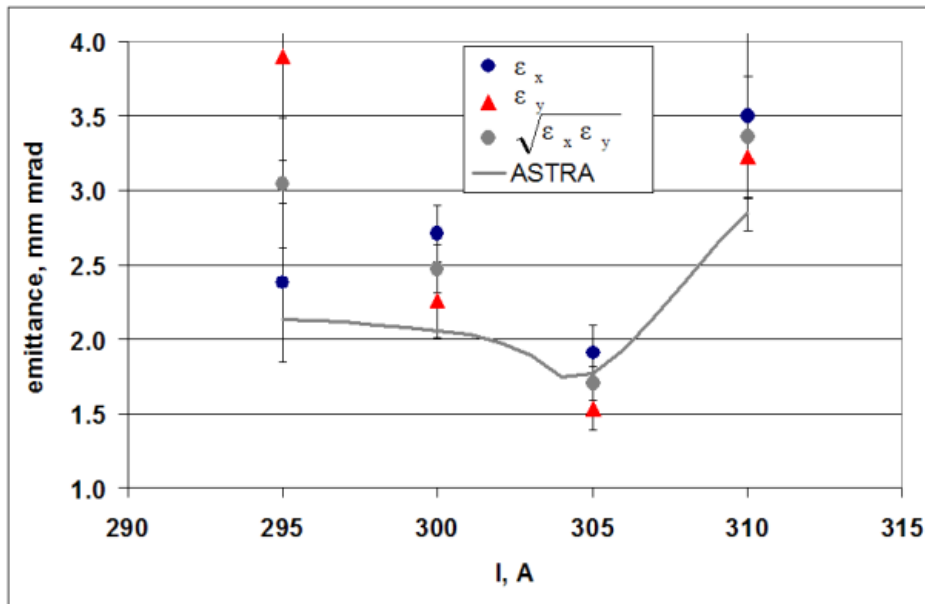


Figure 5.19: Emittance measurements with for $D=1.2$ mm compared with ASTRA simulations, at different rf phases and focusing solenoid currents.



(a) Aperture diameter $D = 0.9$ mm.



(b) Aperture diameter $D = 1.2$ mm.

Figure 5.20: Smallest measured emittance as a function of the main solenoid current

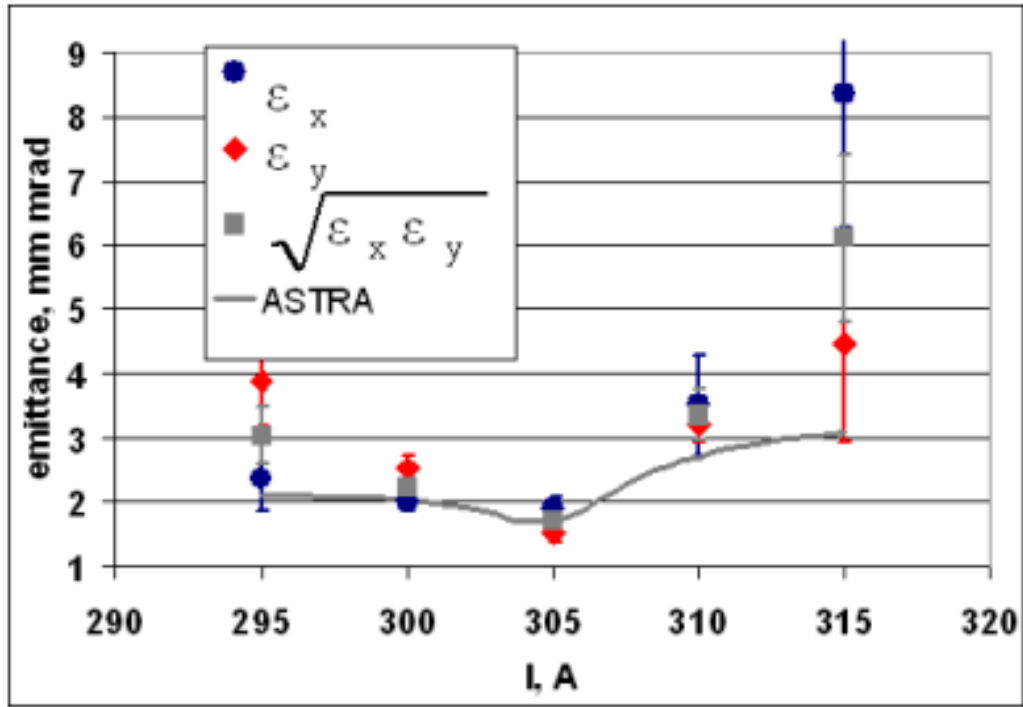


Figure 5.21: Smallest measured emittance with cavity prototype №2, as a function of the main solenoid current.

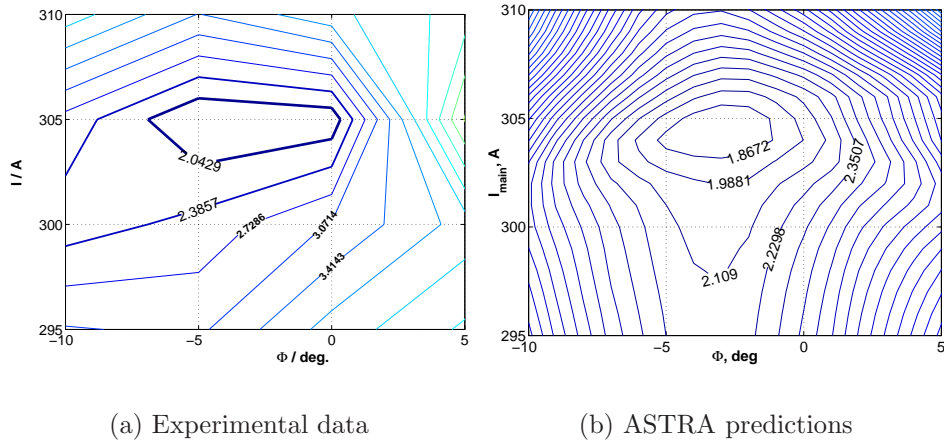


Figure 5.22: Isolines representing the points of equal measured (a) and simulated (b) geometric mean $\sqrt{\epsilon_x \epsilon_y}$ emittance. The experimental characterization is done at 1 nC, an accelerating field of about 42 MV/m and a laser spot rms size $\sigma_x=0.51$ mm, $\sigma_y=0.62$ mm.

differences between the measured horizontal and vertical emittances. Nevertheless, according to the studies summarized in the graph in Fig. 5.11, the geometrical mean $\sqrt{\sigma_x \sigma_y} \approx 0.56$ mm is close to the optimum with respect to the smallest reachable emittance. As expected, apart from the laser spot size and main solenoid current, the measured emittance depends also on the rf phase, therefore it is convenient to summarize the emittance measurements with cavity prototype №2 using an isocontour plot like the one in Fig. 5.22 a, which is to be confronted with the simulated emittance isolines in the right of the same figure. The comparison shows that the position of the isolines around the smallest measured geometric mean emittance of about $1.7 \text{ mm} \cdot \text{mrad}$ agree well with the simulation, however there seems to be a difference in the shape of the contours tracing the higher emittance values. The reason is that in the simulation a round transverse laser profile is assumed, while the real laser shape is rather elliptical than circular. This laser spot shape asymmetry in combination with the applied solenoid field introduces a coupling between the two transverse directions. But as discussed in Chapter 2 the quantity $\sqrt{\epsilon_x \epsilon_y}$ is a measure for the four-dimensional phase space volume only in the case when the coupling is negligible.

5.4.2.4 Measurement results and numerical simulations with cavity prototype №1

After the characterization of cavity prototype №2 and its delivery for installation at the VUV-FEL injector, cavity prototype №1 was installed at PITZ. The conditioning performed in the beginning of 2004 gave the possibility to reach a maximum accelerating gradient of the order of 45 MV/m . The transverse phase space characterization followed the outline of the previously performed studies of cavity №2, but this time the longitudinal solenoid field at the photocathode was compensated from the very beginning. As explained in Chapter 5.4.1, another major improvement concerns the transverse laser shape at the cathode, which had significantly smaller intensity modulations than it was for the measurements with the previous gun. Three different apertures for transverse shaping of the laser beam were successively inserted in the laser beamline. The corresponding PITZ operation conditions for these measurements are listed in Appendix B. The measurements results, compared with simulations, are plotted in the Figures 5.23, 5.24, 5.25. Considering the improved imaging onto the photocathode, the laser transverse profile in the simulations was taken as flat top. The assumed temporal laser pulse profile was a flat top of 18 ps FWHM and 4 ps rise/fall time. In all simulations the bunch charge was set to 1 nC and the accelerating field to 45.8 MV/m . A summary of the emittance measurements with

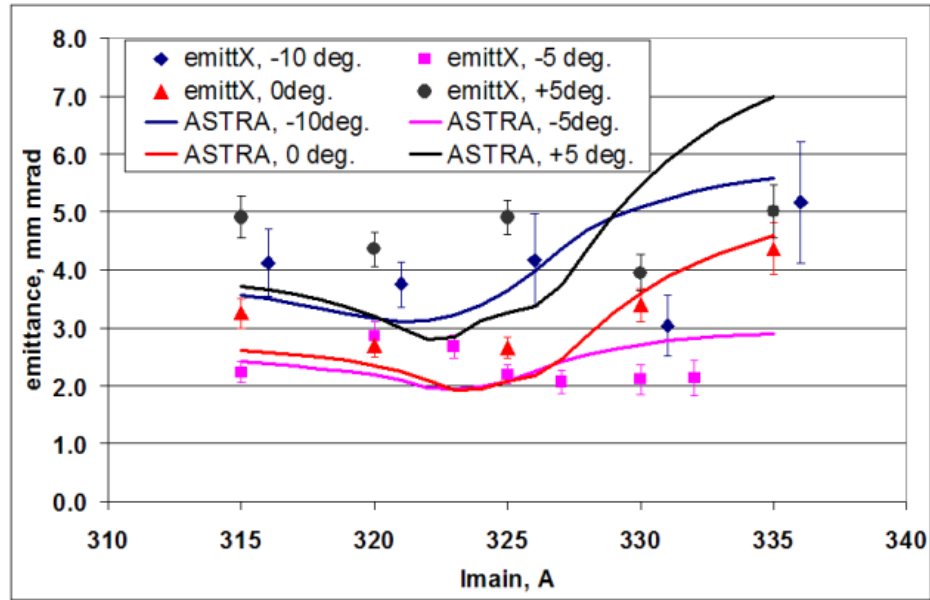
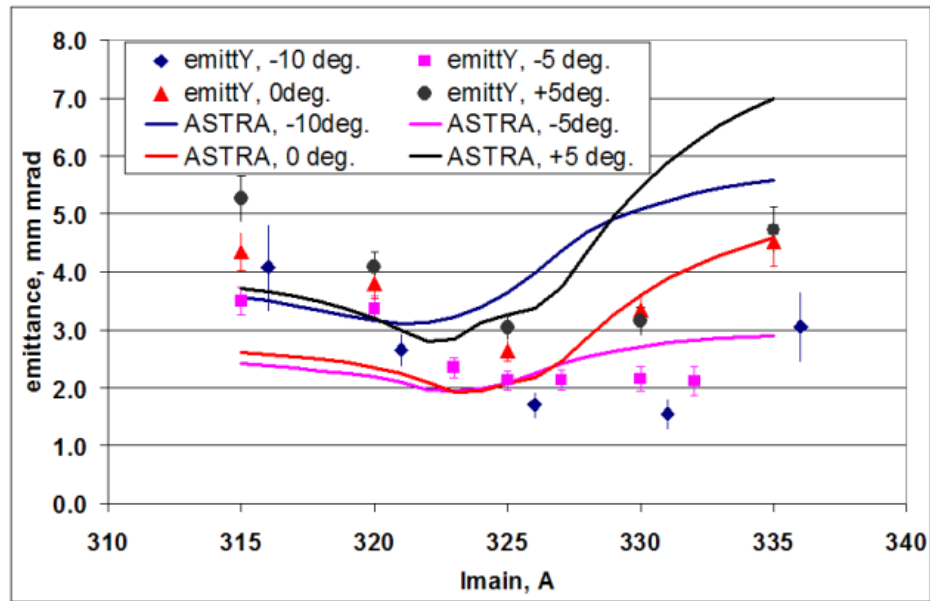
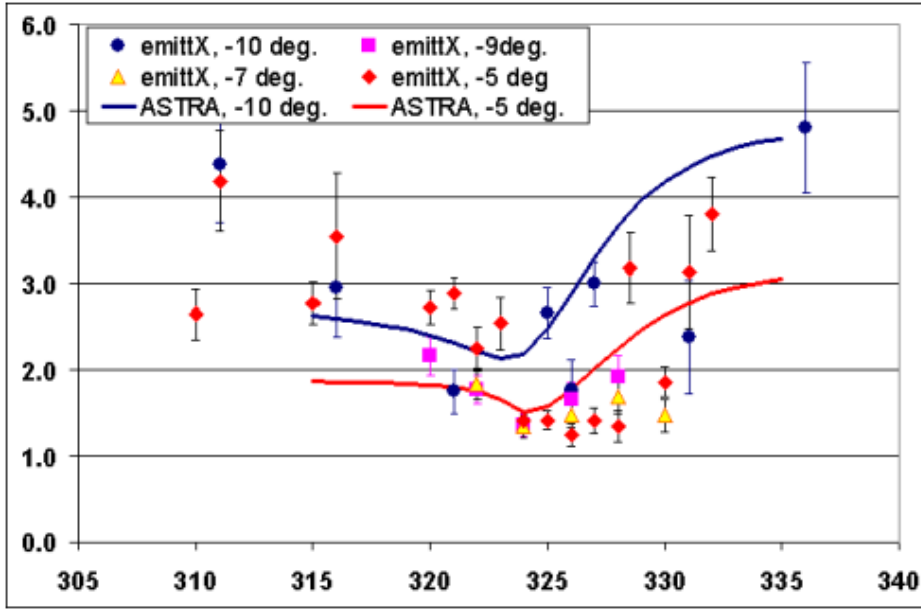
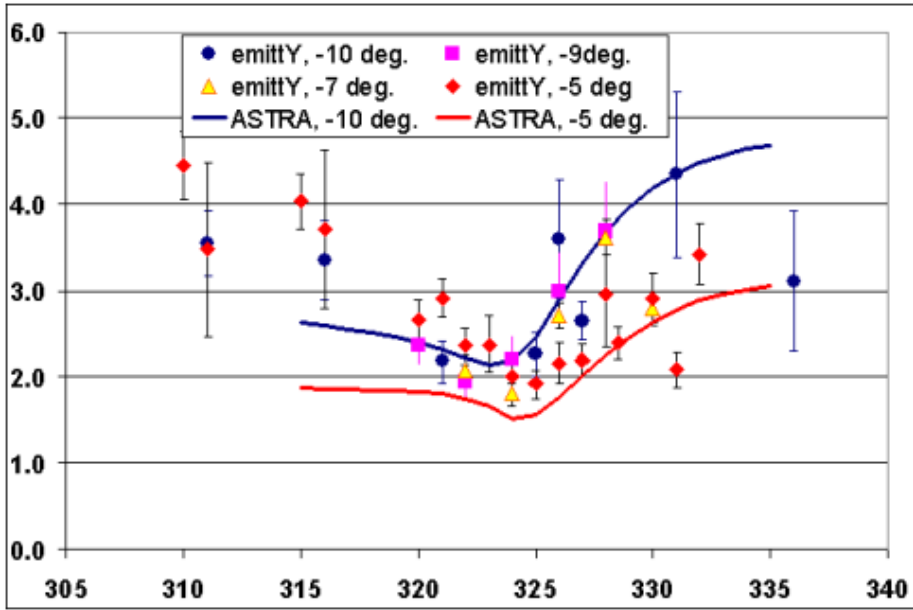
(a) Horizontal emittance at rf phases $\Phi - \Phi_m = (-10, -5, 0, +5)^\circ$ (b) Vertical emittance at rf phases $\Phi - \Phi_m = (-10, -5, 0, +5)^\circ$

Figure 5.23: Emittance measurements for $D=1.2$ mm. The minimal geometrical average emittance $\sqrt{\epsilon_x \epsilon_y} = 2.1 \pm 0.2$ mm mrad is achieved at $\{I = 327 \text{ A}, \Phi - \Phi_m = -5^\circ\}$



(a) Horizontal emittance at rf phases $\Phi - \Phi_m = (-10, -9, -7, -5)^\circ$



(b) Vertical emittance at rf phases $\Phi - \Phi_m = (-10, -9, -7, -5)^\circ$

Figure 5.24: Emittance measurements for $D=1.5$ mm. The minimal geometrical average emittance $\sqrt{\epsilon_x \epsilon_y} = 1.5 \pm 0.2$ mm mrad is achieved at $\{I = 324 \text{ A}, \Phi - \Phi_m = -7^\circ\}$

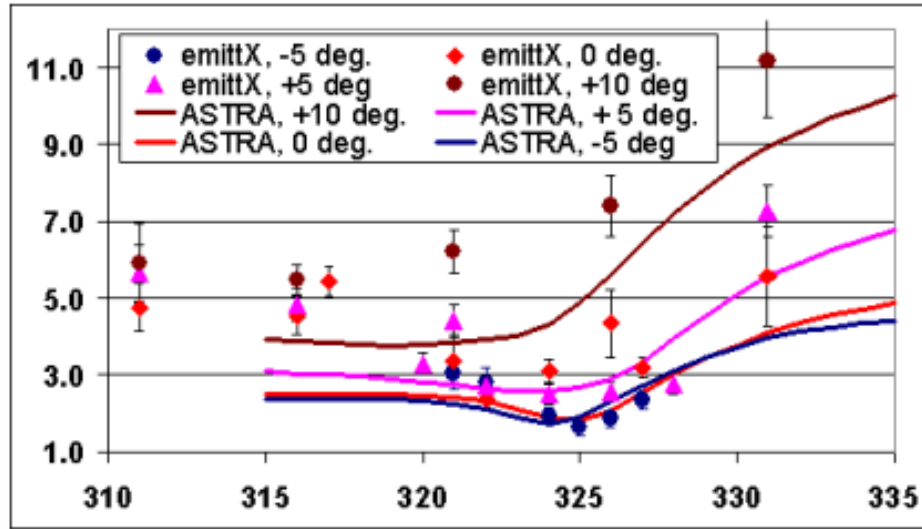
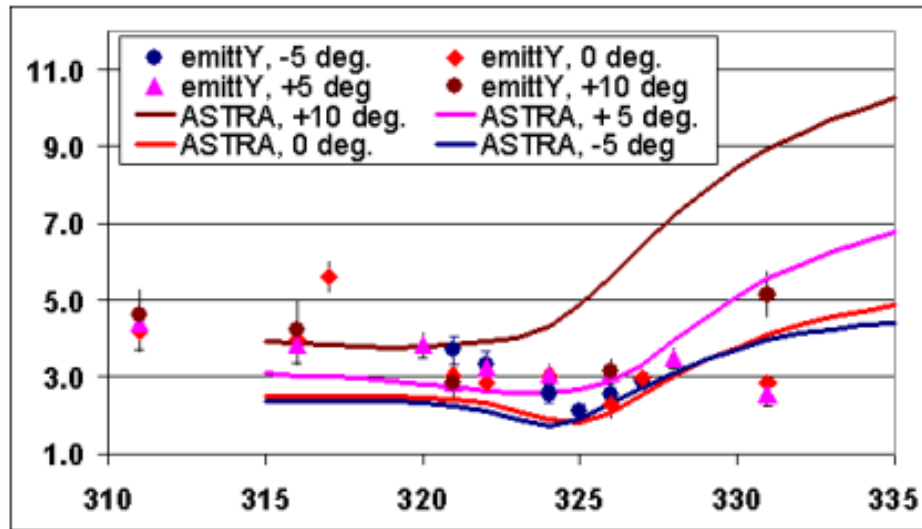
(a) Horizontal emittance at rf phases $\Phi - \Phi_m = (-5, 0, +5, +10)^\circ$ (b) Vertical emittance at rf phases $\Phi - \Phi_m = (-5, 0, +5, +10)^\circ$

Figure 5.25: Emittance measurements for $D=1.8$ mm. The minimal geometrical average emittance $\sqrt{\epsilon_x \epsilon_y} = 1.8 \pm 0.2$ mm mrad is achieved at $\{I = 325 \text{ A}, \Phi - \Phi_m = -5^\circ\}$

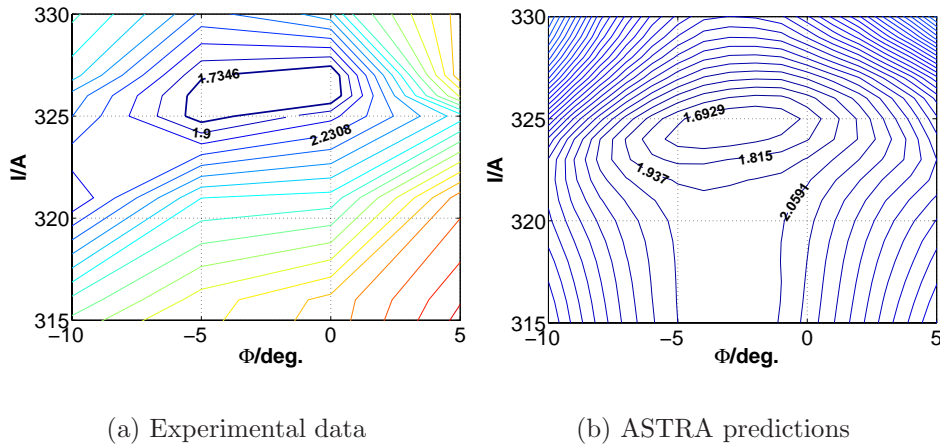


Figure 5.26: Isolines representing the points of equal measured (a) and simulated (b) geometric mean $\sqrt{\epsilon_x \epsilon_y}$ emittance. The experimental characterization is done at 1 nC, accelerating field of about 45 MV/m and laser spot rms size $\sigma_x=0.57$ mm, $\sigma_y=0.59$ mm.

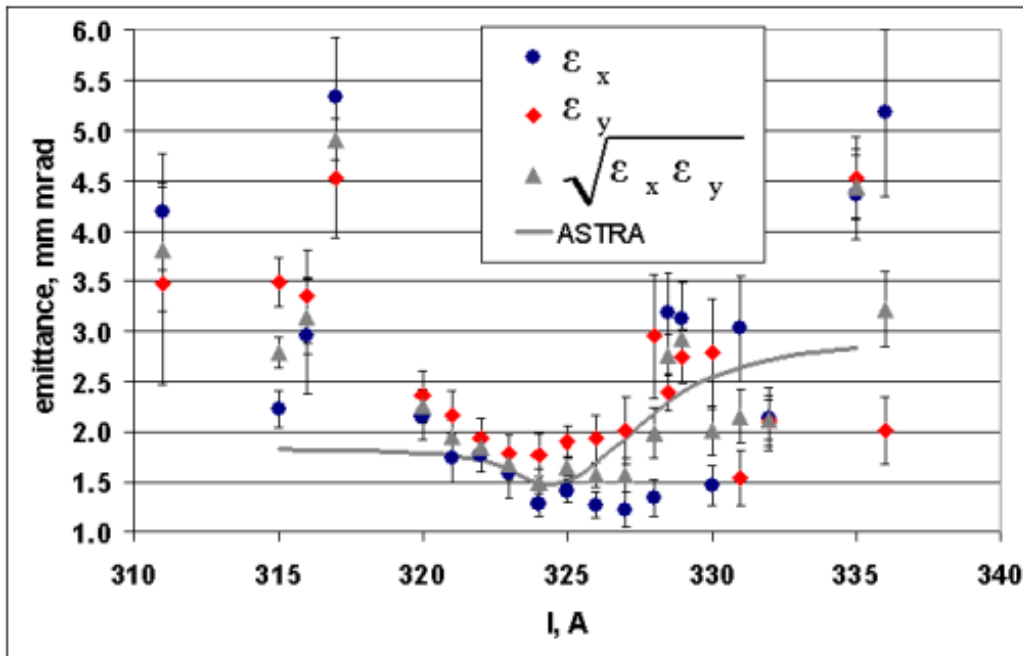


Figure 5.27: Smallest measured emittance as a function of the main solenoid current.

cavity prototype №1 is shown in Fig. 5.26 a, which is to be compared with the simulated emittance isolines on the right of the same figure. Another representation for the smallest measured emittance as a function of the main solenoid current is given in Fig .5.27. Despite of the fair general agreement between the experiment and the simulation, at some points the measured data differ from the results obtained from the idealized model of the beam, which is assumed in the simulations. One can think of several possible effects contributing to this difference like laser misalignment on the photocathode, laser spot nonhomogeneity, variations in laser pulse temporal profile, wake-field effects. The electron beam in the simulations starts from a point on the electrical axis, but in reality the laser beam offset δx_c might be in the order of ~ 0.1 mm [59]. The laser offset in combination with the applied solenoid field break the beam symmetry and introduce an emittance growth proportional to $(\delta x_c/\sigma_r)^2$ [14], where σ_r is the laser spot size. Moreover the simulation assumes a flat top temporal distribution of the laser pulse, but the real longitudinal shape might differ from this model as it is shown in Fig. 5.1(a). Apparently the ripple of the laser intensity with the time results in a fast variation of the space charge field with the longitudinal position in the bunch. As it is discussed in [20], such fast space charge force variation makes the emittance compensation incomplete and degrades the transverse emittance. If the beamline is perfectly aligned the wakefield effects can be neglected. However, in some cases the wakefields associated with certain vacuum components, like the laser in-vacuum mirror (see Chapter 5.5), have significant impact on the beam emittance. This influence is well pronounced when the solenoid current $I_{\text{main}} < 320$ A (see Fig.5.27). In this current range the electron beam is weakly focused and its size in the vicinity of the vacuum mirror is large, what increases the emittance growth induced by the vacuum mirror.

5.4.3 Variation of the rf phase

5.4.3.1 Introduction

The rf phase Φ of the bunch centroid at the moment of injection affects the projected transverse emittance through a variety of phenomena related to the dynamics of the individual particle as well as collective effects for all the electrons in the bunch e.g. space charge interactions and the emittance compensation. Considering the individual particle acceleration one defines the rf emittance growth, determined by the radial deflection in the gun rf field. The total rf emittance growth $\epsilon_{rf} \propto |\cos(\Phi)|$ depends[19] on the particle phase with respect to the rf field $\phi = \omega t - kz + \Phi \approx \frac{1}{2\alpha \sin \Phi} + \Phi$ at the position of

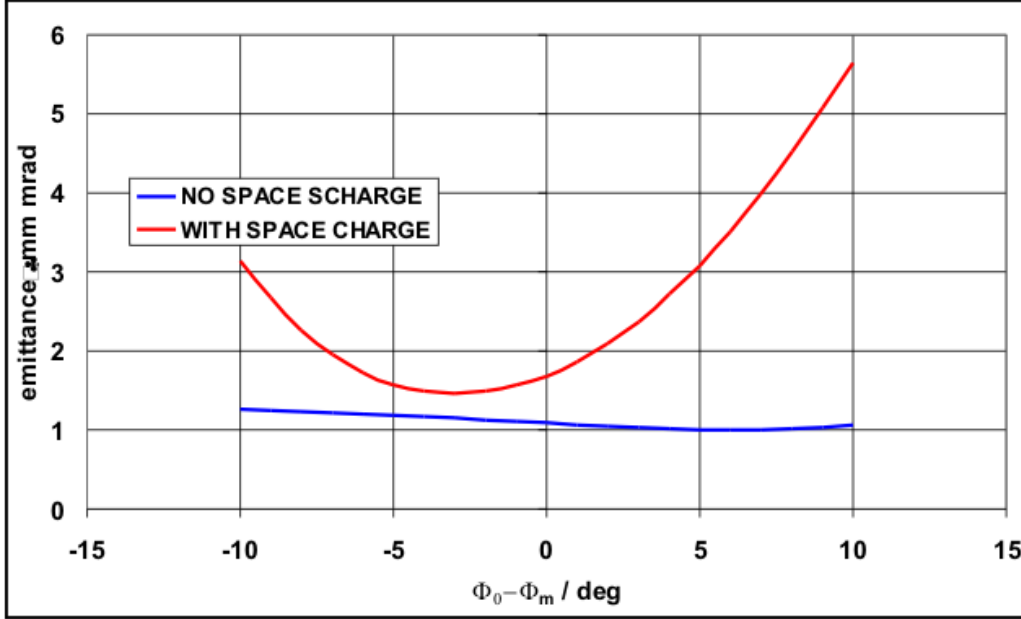


Figure 5.28: The projected transverse emittance is shown as a function of the rf phase. In the simulation are considered two cases - with and without space charge. Φ_m denotes the rf phase of maximum energy gain.

the cavity exit. Here α is the dimensionless rf field strength parameter defined in Eq.5.5. The relation cited above shows the existence of an optimal initial rf phase minimizing the emittance increase due to the rf field. The simulation in Fig. 5.28 shows how the emittance changes with the launch phase with and without taking the space charge forces into account. The case without the space charge forces corresponds to transverse emittance growth only due to the rf field deflection by not more than about 25%. The space charge contribution ϵ_{sc} is significantly larger and as it is shown in the same figure the emittance varies by up to 300% in the same phase range. If the presence of the self field can not be neglected then the rf phase has a twofold impact on the beam emittance - first on the emittance of each longitudinal bunch slice and second on the total projected emittance of the entire slice ensemble. The single slice emittance is influenced by the relativistic damping of the space charge force. Due to the variation of the initial phase Φ the acceleration $\frac{d\gamma}{dz}$ changes, especially in the vicinity of the photocathode, where the approximation $\frac{d\gamma}{dz} \approx \frac{eE_0}{m_0c^2} \sin \Phi$ is valid. Subsequently the final state energy γ_{end} as well as the net transverse momentum p_{\perp} arising from the repulsive self field force will also change. The variation of the single slice phase space volume as a function of the launching rf phase follows through the relation

$p_{\perp} \propto \int_1^{\gamma_{end}} \frac{d\gamma}{\gamma^2 \beta}$. However the slice emittance growth has a significant contribu-

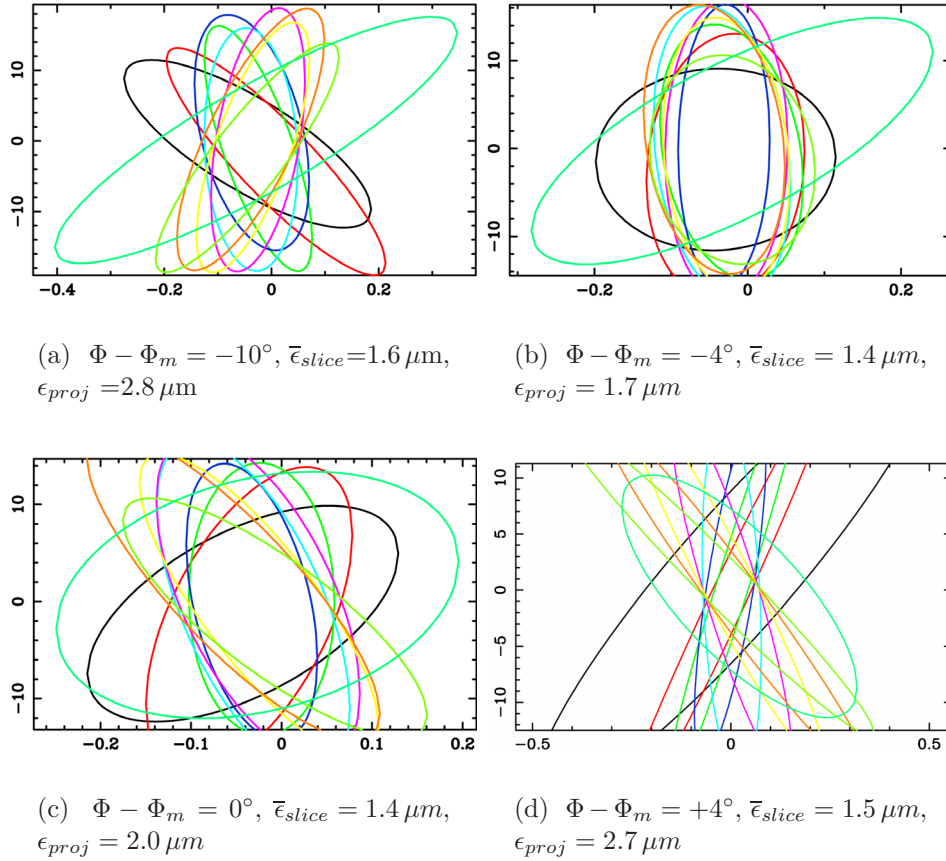
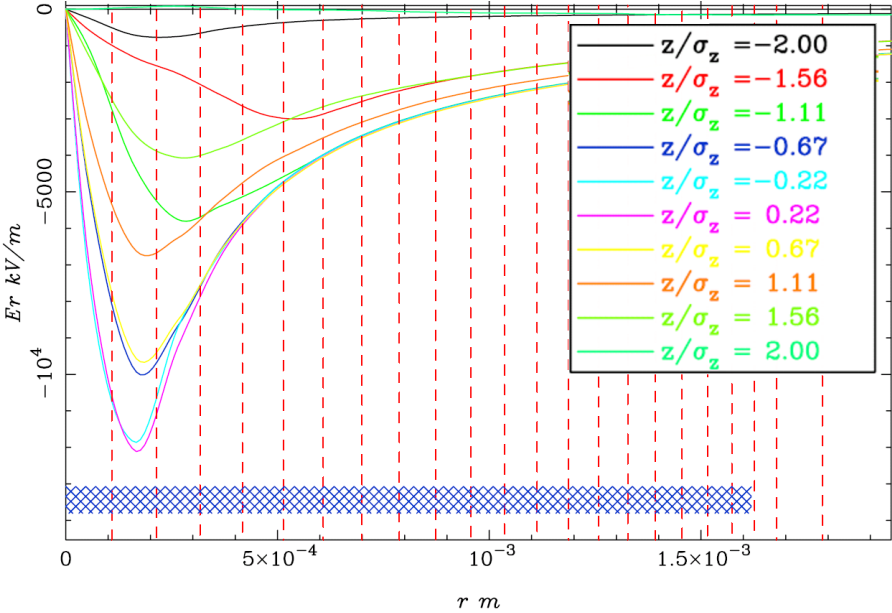


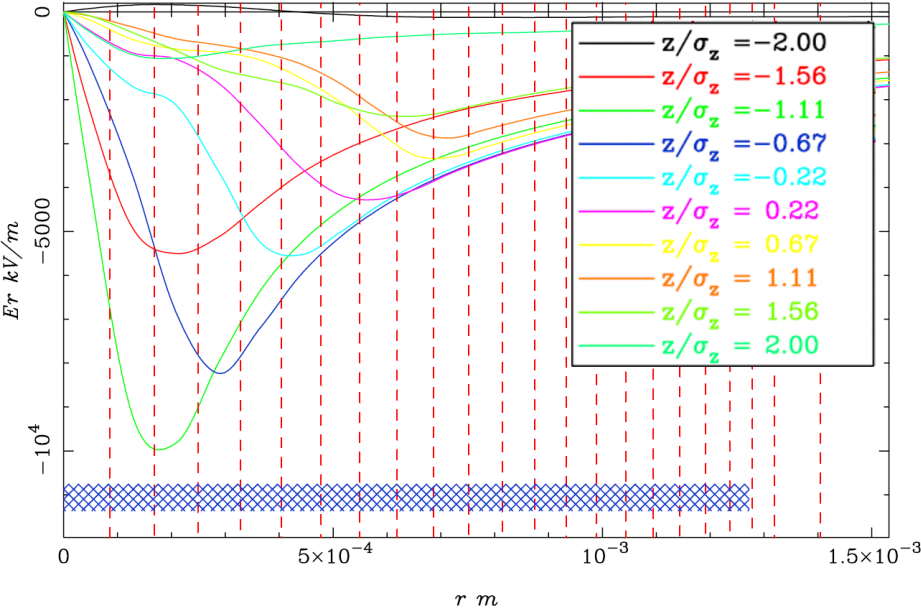
Figure 5.29: Simulated slice phase space ellipses for different rf phases. The solenoid field is tuned to achieve minimum projected emittance ϵ_{proj} at each phase. Φ_m denotes the rf phase of maximum energy gain.

tion to the projected beam emittance only when the injector is operated in the emittance compensation regime as shown with simulations in Fig. 5.29 (b). In this case the correlated part of the emittance is about to vanish and therefore the slice emittance starts to be the dominant emittance source.

The rf phase variation has a significant influence on the conditions for emittance compensation as one can conclude from the same set of graphs. This is accomplished through a modification in the longitudinal charge distribution along the bunch. The longitudinal charge distribution as well as the transverse space charge field varies along the bunch as it is presented in the plots of Fig. 5.30 and Fig. 5.31. Obviously for some operation conditions



(a) $\Phi - \Phi_m = -10^\circ$



(b) $\Phi - \Phi_m = +4^\circ$

Figure 5.30: The radial space charge electric field E_r is plotted vs. r for different rf phases and different bunch slices.

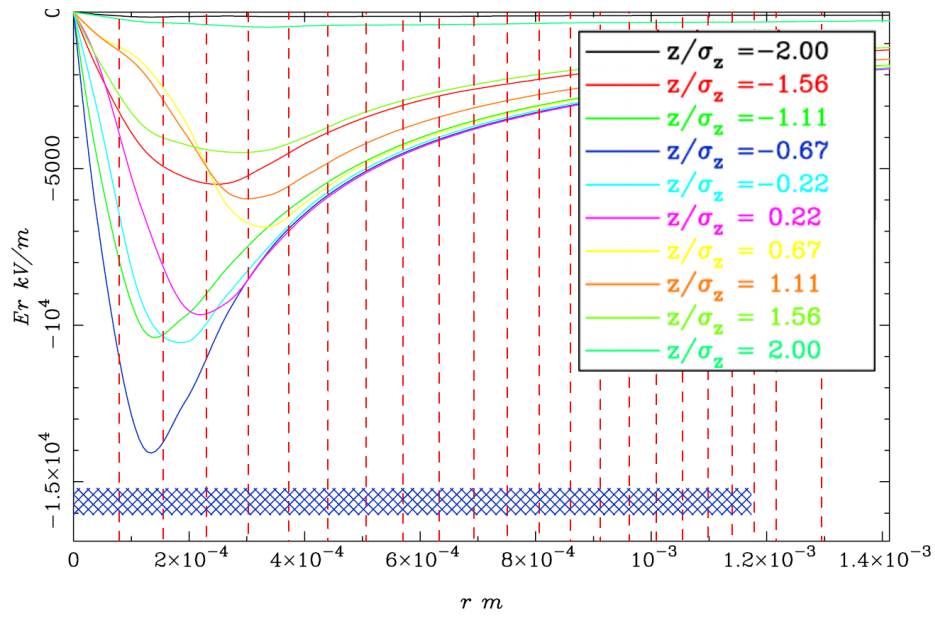
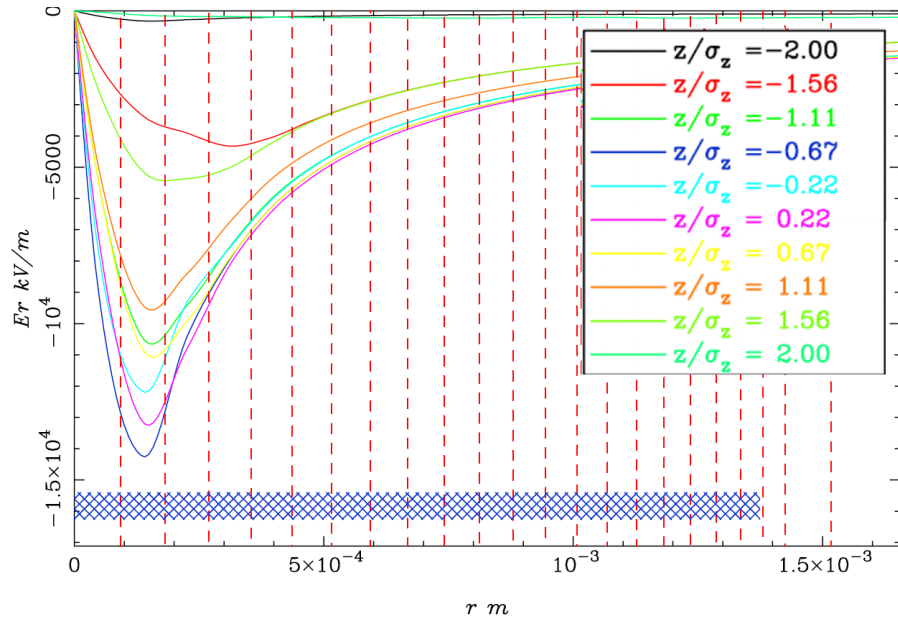
(a) $\Phi - \Phi_m = 0^\circ$ (b) $\Phi - \Phi_m = -4^\circ$

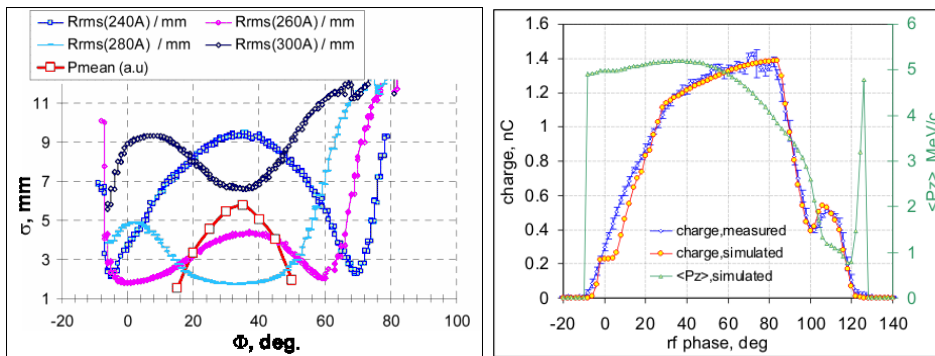
Figure 5.31: The radial space charge electric field E_r is plotted vs. r for different rf phases and different bunch slices.

the radial nonlinearities will be more pronounced as for instance in the cases plotted in Fig. 5.30, which are corresponding to the phase spaces in Fig 5.29 (a) and (d). The emittance correction will be most effective when the nonlinear field components are minimized as shown if Fig 5.31 (b) and Fig 5.29 (b).

5.4.3.2 Measurement results and numerical simulations

The influence of the rf phase on the transverse emittance was studied for both cavity prototypes №2 and №1. These investigations were part of the full characterization of the photoinjector. The corresponding gun operation parameters are as listed in Appendix B. The rf phase was varied in 5° steps around the phase of maximum mean energy gain Φ_m , which was determined by measuring the rms electron beam size vs. the rf phase as shown in Fig. 5.32(a). There Φ_m corresponds to the local extremum ($\sim 40^\circ$) of the beam spot size. The accuracy of the phase determination is about 2° [59]. Since the charge varies considerably with the rf phase, as plotted in Fig. 5.32 (b), the laser output power was tuned to 1 nC after each phase change. The charge and the phase stability were verified before each emittance measurement. The measurement results are summarized and compared with simulations in Fig.5.33 and Fig.5.34 for the two cavities №2 and №1 respectively. The input parameters used for the simulations are as described in Chapter 5.4.2.3 and Chapter 5.4.2.4.

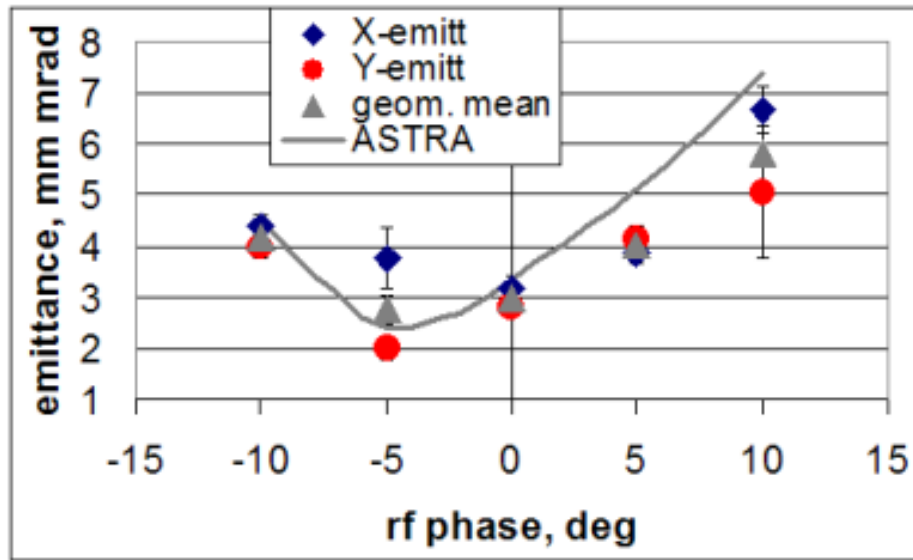
As expected from the discussion in the previous section 5.4.3.1 and from



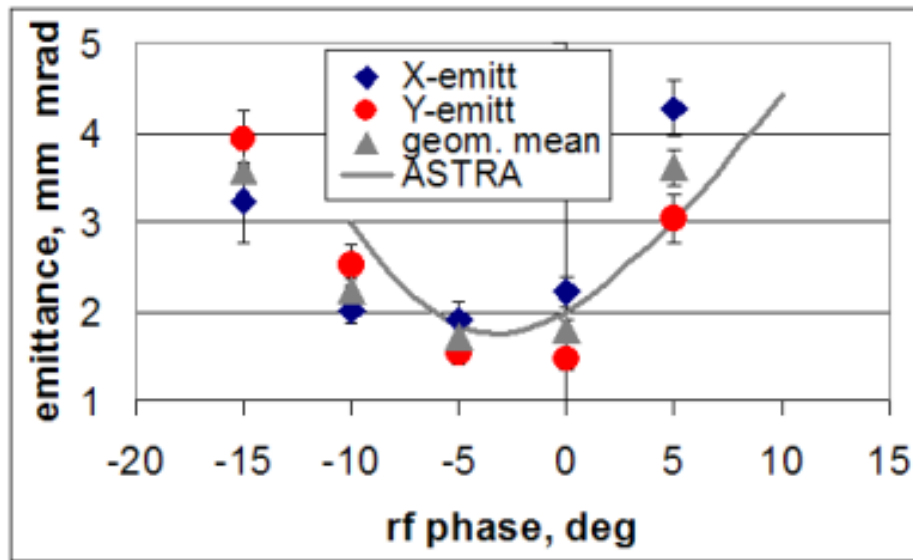
(a) RMS electron beam size variation with rf phase.

(b) Variation of the bunch charge with rf phase

Figure 5.32: The beam rms size and the bunch charge are scanned vs. rf phase.

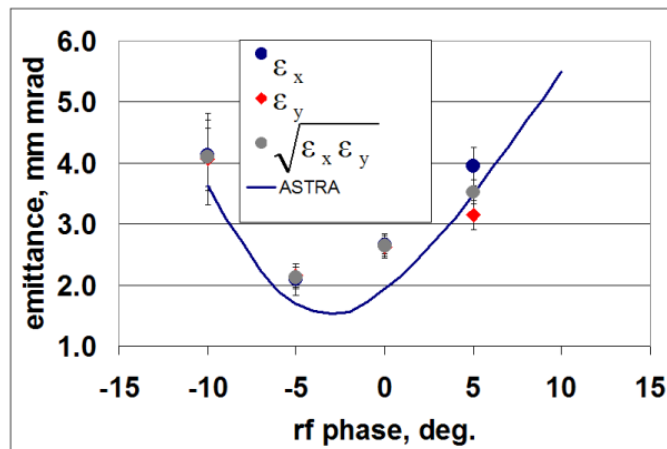


(a) $D=0.9$ mm

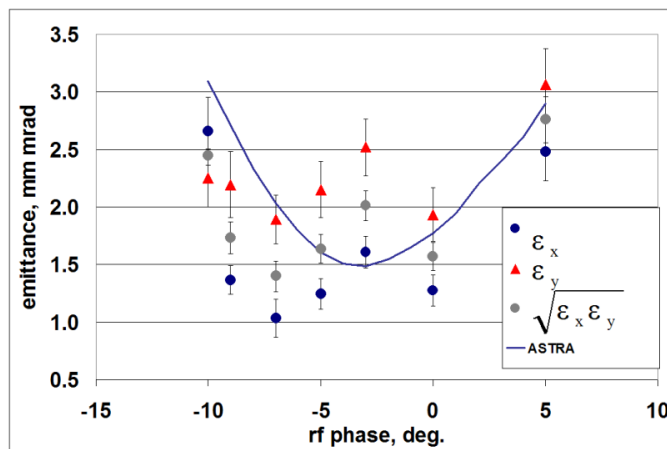


(b) $D=1.2$ mm

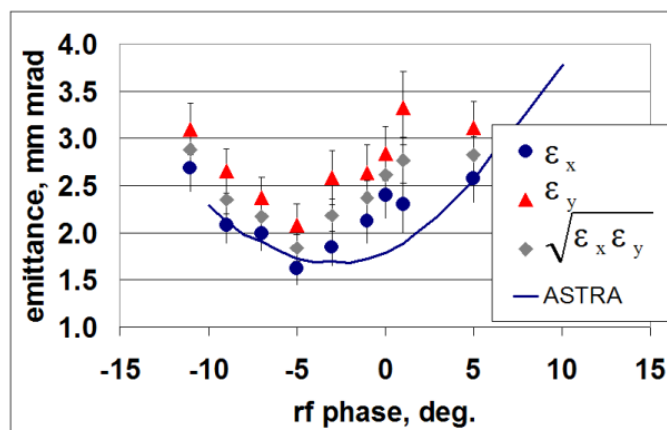
Figure 5.33: Smallest measured emittance as a function of the rf phase. The studies are performed with gun№2 at an accelerating gradient of about 42 MV/m. Two cases are considered: laser beam shaping aperture diameter $D=0.9$ mm (a) and $D=1.2$ mm (b).



(a) D=1.2 mm



(b) D=1.5 mm



(c) D=1.8 mm

Figure 5.34: Smallest measured emittance as a function of the rf phase. The studies are performed at an accelerating gradient of about 45 MV/m.

simulations, one observes a strong correlation between the emittance and the rf phase. From the experimental data and the simulations presented in Fig. 5.33 one can conclude that the emittance, at a bunch charge of 1 nC and accelerating gradient of about 42 MV/m, has a shallow minimum at about $\Phi - \Phi_m \approx -5^\circ \pm 2^\circ$ (the uncertainty is due to determination of Φ_m , see Fig.5.32(a)). An identical result follows from the studies performed with cavity №1 at about 45 MV/m (see Fig.5.34). Since the simulations take into account the nonlinear space charge field in the projected emittance calculation and given the good agreement with the experimental data, it is justified to conclude that by proper tuning of the rf phase one minimizes the nonlinear self field components and thus achieves operation conditions for maximal emittance correction.

In the present section the emittance was studied as a function of the launching phase of gun №1 and gun №2 at 1 nC. For the interpretation of the results it was taken for granted that the thermal emittance stays constant with the phase, which is a reasonable assumption as long as the space charge emittance growth is much higher than the thermal emittance. However, according to the low charge ($Q < 6$ pC) studies presented in Section 4 of this thesis, the thermal emittance ϵ_{th} grows with the electric field E at the photocathode at the moment of extraction. Through the relation $E = E_0 \sin(\Phi)$, the electric field and hence ϵ_{th} depend on the rf phase, which has to be considered for the production of ultra low emittance beams at high gradients.

5.4.4 Variation of the compensating magnetic field at the photocathode

If the photoelectrons are emitted from a region with non zero longitudinal magnetic field they attain an initial angular momentum $P_\theta(r_0) \propto \Psi_0$, which is an integral of motion proportional to the magnetic flux Ψ_0 enclosed by the extraction radius r_0 [66]. When Ψ_0 is nonzero, then the evolution of the transverse rms beam size of a relativistic electron bunch in a drift is governed by a modification of Eq. 5.2 [67]:

$$\sigma'' - \frac{\epsilon_n^2}{\sigma^3 \beta^2 \gamma^2} - \frac{P}{4\sigma} = \frac{1}{\sigma^3} \left(\frac{e\Phi_0}{2\pi\beta\gamma m_0 c} \right)^2 \quad (5.20)$$

The term on the RHS of Eq. 5.20 has a strong nonlinear dependence through the $1/\sigma^3$ factor, which determines the significant defocusing effect when the beam size is about its minimum. The additional radial momentum due to the nonzero magnetic field is equivalent (see Appendix A) to an emittance increase and therefore one should carefully compensate the magnetic field at the cathode. The solenoid field compensation at PIZ is done by means of a bucking coil located behind the cathode. The field of the bucking coil is opposite to the field of the main solenoid so that the field at the cathode position can be set to zero. The correlation between the currents of the bucking and the main solenoid, which is required to compensate the magnetic field at the position of the cathode and respectively to minimize the magnetic emittance growth is of major interest. It has been studied by magnetic measurements with a hall probe described in [64] and by investigating the rotation angle of the electron beamlets with the use of a He-Ne alignment laser. The results of the latter experiments are described below.

5.4.4.1 Measurements of zero field conditions with the use of He-Ne alignment laser

The idea of these investigations is to determine the dependence of the beamlet rotation angle on the bucking coil current and to determine a condition for which the angle reaches zero i.e. for which there is no residual angular momentum and hence no uncompensated magnetic field. As mentioned, the beamlet image is observed on a screen after the slit mask and the rotation angle has to be measured relative to the slit direction. Therefore prior to the measurements with electron beamlets it is necessary to determine the slit direction as a reference on the observation screen. In order to do this a light source - a He-Ne laser ($\lambda \approx 650$ nm) mounted at the rear window

of the diagnostics cross was used. The laser beam was fed into the vacuum pipe and then reflected on a mirror in the beamline towards the slit mask. When the laser light illuminates the slit it diffracts and creates a clearly visible interference pattern 1 m downstream on the observation screen, as presented in Fig 5.35. It has to be taken into account that the diffracted laser light spreads perpendicular to the slit direction and therefore the observed intensity distribution appears to be turned by 90° with respect to the slit orientation. The angular size of the first diffraction maximum is of the order of $\frac{2\lambda}{d} \approx 26$ mrad hence its spatial extent on the screen is about 20-30 mm, while the typical size in perpendicular transverse direction is of the order of 1 mm. The reference rotation angles α_0, β_0 were determined by the inclination of the principal axis of the light intensity distribution. The next step

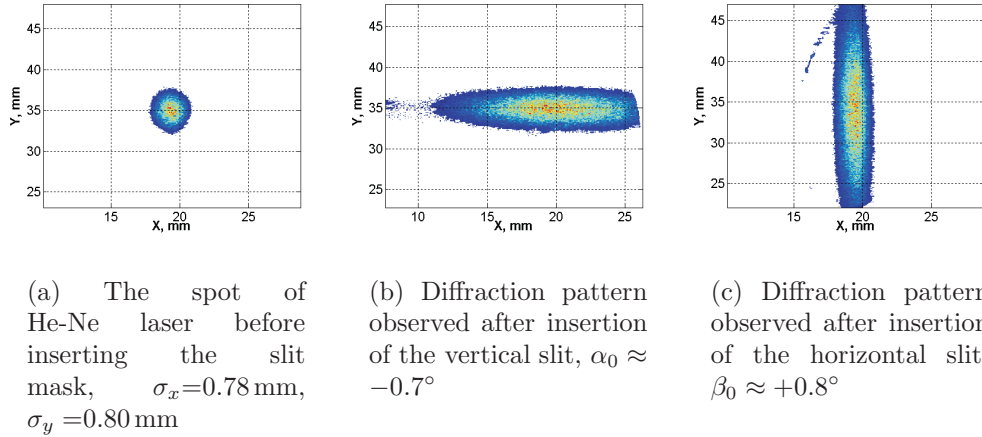


Figure 5.35: The diffraction pattern of the laser light observed on the screen about 1 m behind the slit mask.

for determining the zero magnetic field condition at the photocathode was to measure the rotation angles of the electron beamlets as a function of the bucking coil current. These measurements were successfully performed for the photoinjector operation conditions where the smallest transverse emittance was reached - respectively $\{305$ A, $-5^\circ\}$, $\{305$ A, $0^\circ\}$ with gun №2 and $\{324$ A, $-5^\circ\}$, $\{324$ A, $-7^\circ\}$ for gun №1. For the injector operation conditions specified above, the bucking coil current was scanned by 10 A steps in the range $\{0-50\}$ A. The dependence of the beamlet rotation angle $\delta\alpha = \alpha - \alpha_0$ for each I_{main} is given in Fig. 5.36 for the beamlets obtained from the X- slit and respectively $\delta\beta = \beta - \beta_0$ in Fig. 5.37 for the ones obtained from the Y-slit. Despite of the fact that different rf phases were used, the zero field conditions for a fixed main solenoid current should be the same i.e. one expects

that a straight line fit to the measured rotation angles $\delta\alpha = \delta\alpha(I_{\text{buck}})|_{I_{\text{main}},\Phi}$ intersect the abscissa in one and the same point for a given main solenoid current. The results of this analysis were put together in Table 5.1, where

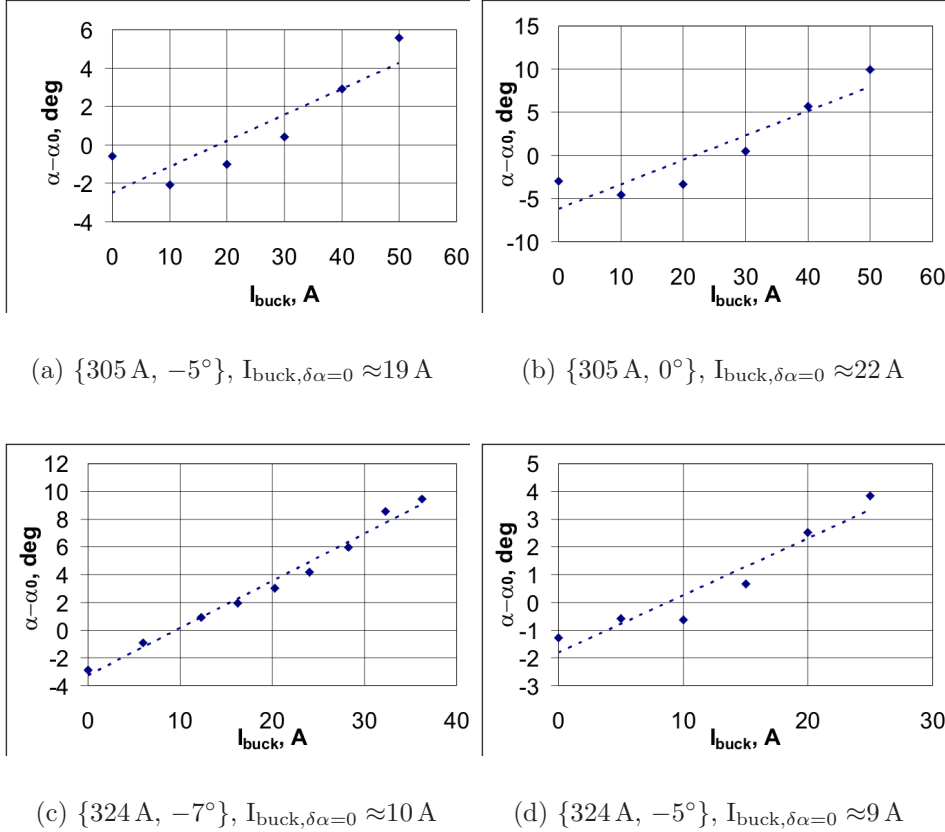


Figure 5.36: The dependence of the rotation angle of the electron beamlets on the bucking solenoid current is shown for various main solenoid and rf phase settings. The beamlets are obtained after inserting the X- slit.

Table 5.1: Final results for the correlation between main and bucking solenoid currents as determined by beamlets rotation angles.

I_{main}	$I_{\text{buck}}(\delta\alpha = 0, \delta\beta = 0)$	$\langle I_{\text{buck}} \rangle$
305 A, -5°	{19, 21} A	20 ± 2 A
305 A, 0°	{22, 17} A	20 ± 4 A
324 A, -7°	{10, 21} A	16 ± 8 A
324 A, -5°	{9, 19} A	14 ± 7 A
χ^2 fitting yields: $I_{\text{buck}} = 0.0633 \cdot I_{\text{main}}$		

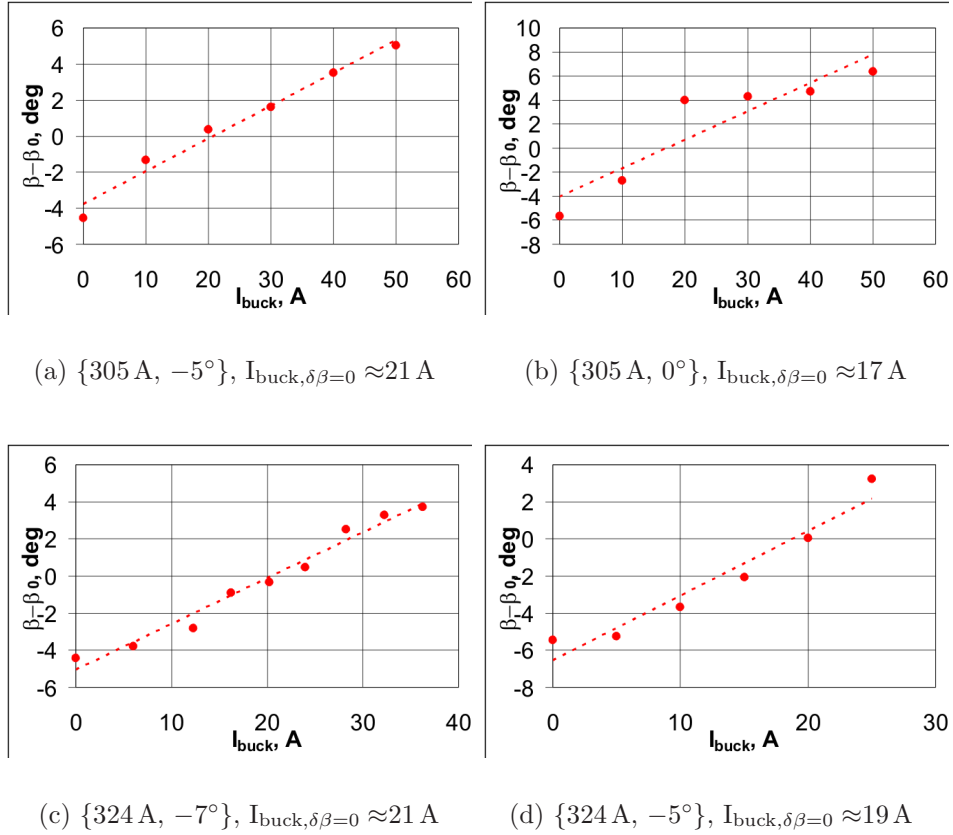


Figure 5.37: The dependence of the rotation angle of the electron beamlets on the bucking solenoid current is shown for various main solenoid settings. The beamlets are obtained after inserting the Y- slit.

the last column gives the mean value of the bucking coil currents needed to null $\delta\alpha$ and $\delta\beta$. The uncertainty is calculated as a standard deviation of the currents. The final correlation between I_{buck} and I_{main} has been determined assuming a direct proportional dependence and a χ^2 fit has been done. According to the analysis the condition to compensate the longitudinal magnetic field at the position of the cathode plane is $I_{\text{buck}} = 0.0633 \cdot I_{\text{main}}$, which is in a fair agreement with the result of the Hall probe measurements[64]: $I_{\text{buck}} = 0.0764 \cdot I_{\text{main}}$.

5.4.5 Variation of the electron bunch charge

5.4.5.1 Introduction

The optimization of the performance of a high gain FEL operating at very short wavelength requires the production of an electron beam of high quality to keep the overall length of the facility as well as the construction costs in reasonable limits. As it is derived in [68] the necessary undulator length is inversely proportional to the amplifier gain, hence one could reformulate the FEL performance optimization as a search for the conditions to maximize the undulator gain. The gain scales with the bunch charge Q as $\propto Q^{\frac{1}{3}}$, but on the other hand the increased charge leads to emittance growth due to stronger self field forces. The larger transverse emittance introduces an additional longitudinal velocity spread the same way as the longitudinal momentum spread does [68], [69] and thus drives a fraction of the electrons out of the amplifier bandwidth, which reduces the lasing part of the bunch and at the end decreases the output power. In order to find the exact balance between these two contrary effects one needs to investigate the dependence of the transverse emittance as a function of the bunch charge.

The scaling of the transverse emittance with the bunch charge has been theoretically studied in a number of papers (e.g. [55], [19], [70], [71]), where various physical models have been introduced. Kim [19] examines the space charge emittance growth of a bunched beam during the acceleration in the rf gun. Jones [55] complements the physical picture by introducing a model to describe the emittance evolution of a drifting electron bunch. In both papers the authors consider the emittance as induced solely by the transverse self field E_r and by integrating the equations of transverse motion they obtain an estimation for the space charge emittance growth in one and the same general form

$$\epsilon_{sc} \propto Q \cdot \mu(A) \quad (5.21)$$

Here $\mu(A)$ is a geometric factor depending on the charge distribution in the bunch and A is the bunch aspect ratio. However this linear dependence of the emittance on the bunch charge has been derived without taking into account neither the applied external magnetic fields nor the emittance compensation mechanism.

The scaling of the emittance with the bunch charge for a photoinjector, which like PITZ is operated in the emittance correction regime, can be estimated by applying the theory of the emittance compensation keeping in mind that the beam emittance is a quadratic sum of a number of contributions like space charge, rf field, thermal emittance,

$$\epsilon_n \approx \sqrt{\epsilon_{sc}^2 + \epsilon_{rf}^2 + \epsilon_{th}^2} \quad (5.22)$$

In order to estimate the space charge contribution one should recall that by setting the proper operation conditions it is possible to obtain at a position around the beam waist a constant phase space orientation for all longitudinal bunch slices and hence a vanishing correlated emittance. In this working mode the beam is characterized by a waist spot size σ_w and divergence σ'_w , which can be expressed as follows[53]:

$$\sigma_w \propto \sqrt{I}f(\alpha, k, A); \quad \sigma'_w \propto \sqrt{I}g(\alpha, k, A) \quad (5.23)$$

Here the strength of the accelerating field α , the aspect ratio A and the rf wave number k were already defined in Eq. 5.5 and f and g are functions only of A , k and α . Taking into account that at a beam waist the correlation $\langle xx' \rangle$ is zero, it follows from Eq. 5.23 that the space charge emittance will be proportional to the current I :

$$\epsilon_{sc} \propto \sigma_w \sigma'_w \propto I \quad (5.24)$$

On the other hand the beam current is inversely proportional to the bunch length σ_z :

$$I \propto \frac{Q}{\sigma_z} \quad (5.25)$$

At this point one has to take into account that the bunch length scales linearly with the charge[72]:

$$\sigma_z \approx \sigma_{z,0} + v \cdot Q \quad (5.26)$$

where v is a coefficient depending on rf gradient, rf phase and laser spot size. Replacement of Eq. 5.26 in Eq. 5.25 and Eq. 5.24 yields:

$$\epsilon_{sc} \propto \frac{Q}{\sigma_{z,0} + v \cdot Q} \quad (5.27)$$

The rf induced emittance growth ϵ_{rf} has been examined in [19], where the following relation was derived:

$$\epsilon_{rf} \propto \sigma_z^2 \sigma_x^2 \quad (5.28)$$

here σ_x and σ_z denote the bunch transverse and longitudinal dimensions at the second gun iris, which scales as[53] $\sigma_x \propto \sqrt{Q}$ and hence from the scaling law given by Eq. 5.26 it follows that:

$$\epsilon_{rf} \propto Q(\sigma_{z,0} + v \cdot Q)^2 \quad (5.29)$$

Replacing Eqs. 5.27, 5.29 in Eq. 5.22 and assuming that the thermal emittance does not depend on the charge one obtains the following general form of the emittance as a function of the bunch charge:

$$\epsilon_n \approx \sqrt{\epsilon_{th}^2 + a \frac{Q^2}{(\sigma_{z,0} + v \cdot Q)^2} + bQ^2(\sigma_{z,0} + v \cdot Q)^4} \quad (5.30)$$

Typically the graph of the function given by Eq. 5.30 is an S-shaped curve as the one shown in Fig. 5.38. Here the measured geometric mean emittance (details in the section below) has been fitted to the model introduced in Eq. 5.30. Thus one obtains the theoretical expectation ϵ_{fit} as well as its first derivative $\epsilon'_{fit} = d\epsilon_{fit}/dQ$. The derivative has a minimum at a charge of about 1 nC. Taking into account that:

$$\epsilon(Q) = \epsilon(0) + \int_0^Q \epsilon'(\xi) d\xi \quad (5.31)$$

it becomes evident that increasing the charge above the limit of about 1 nC would be at the expense of a rapid growth of the transverse emittance, which might oppose a possible FEL application of the electron source at higher charge.

5.4.5.2 Measurements and simulations

The experimental study of the dependence of transverse emittance on the bunch charge Q has been done for $Q = \{0.02, 0.1, 0.2, 0.4, 1.0, 2.0, 3.8\}$ nC with the slit scanning technique. The following measurement procedure was carried out: the rf phase was set to the phase of maximal mean energy gain Φ_m then the charge was adjusted to the desired value and afterwards the solenoid current was adjusted in order to minimize the emittance. During the measurements the rf gradient was kept at a constant value of about 42 MV/m and the laser spot size at $\sigma_x = 0.47$ mm, $\sigma_y = 0.54$ mm. Before each measurement the temporal laser profile was tuned to be as close as possible to a flat-top profile of about 20 ps FWHM and about 5 ps rise/fall time. The measurement results are put together with an ASTRA simulation in Fig. 5.39(a). The charge dependence shows the characteristic 'nose' in the low charge region up to 0.5 nC, where the transition from the emittance dominated to the space charge dominated regime takes place. A similar set of measurements was done at an rf phase $\Phi - \Phi_m = -5^\circ$ for $Q = \{0.4, 1.0, 2.0, 3.4\}$ nC. The experimental data are presented in Fig. 5.39(b). One has to stress that the presented measurements of the emittance as a function of the

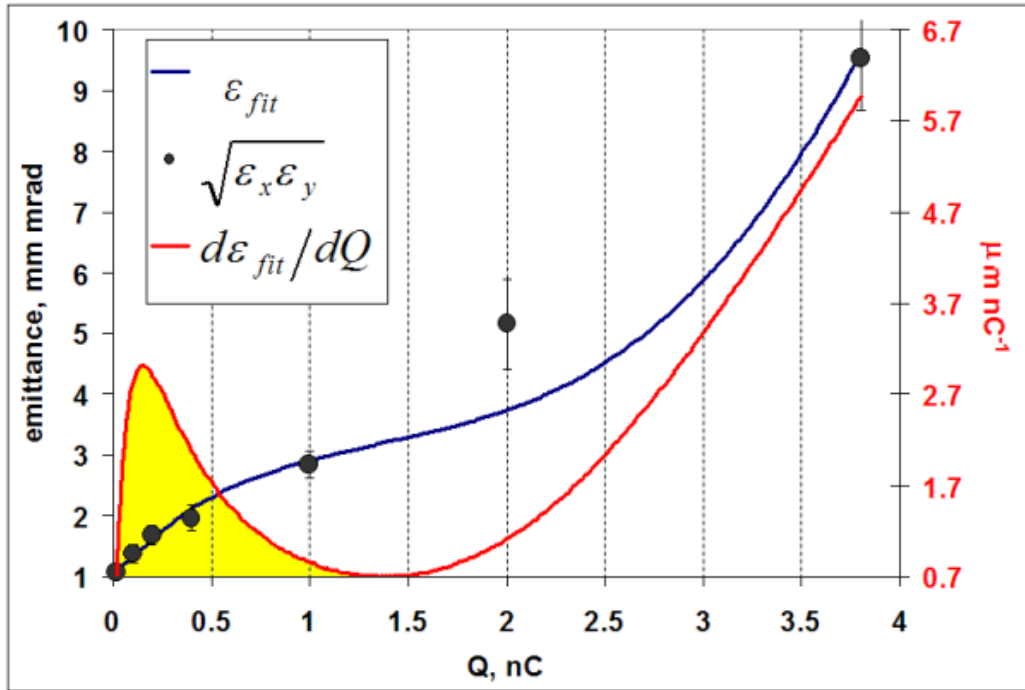
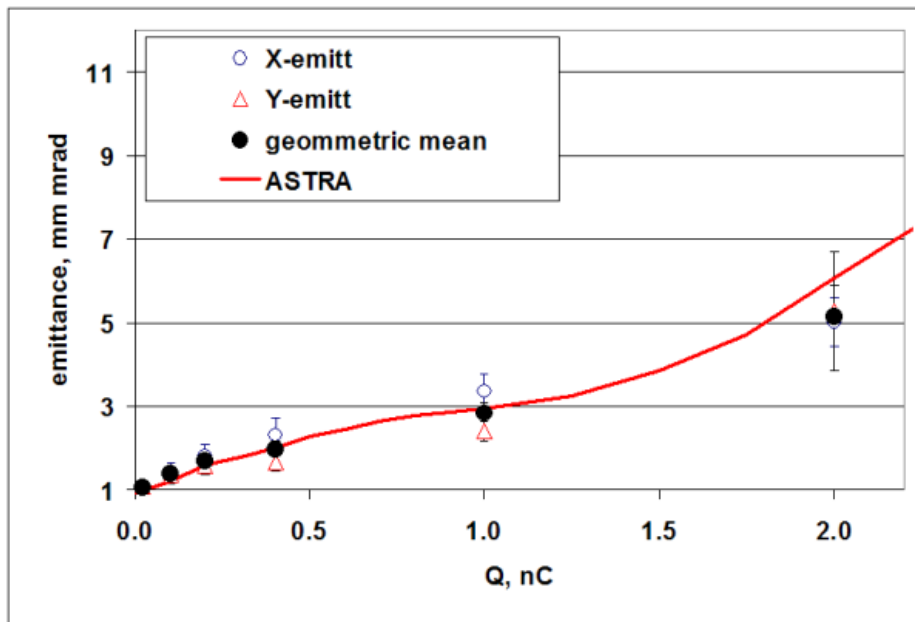
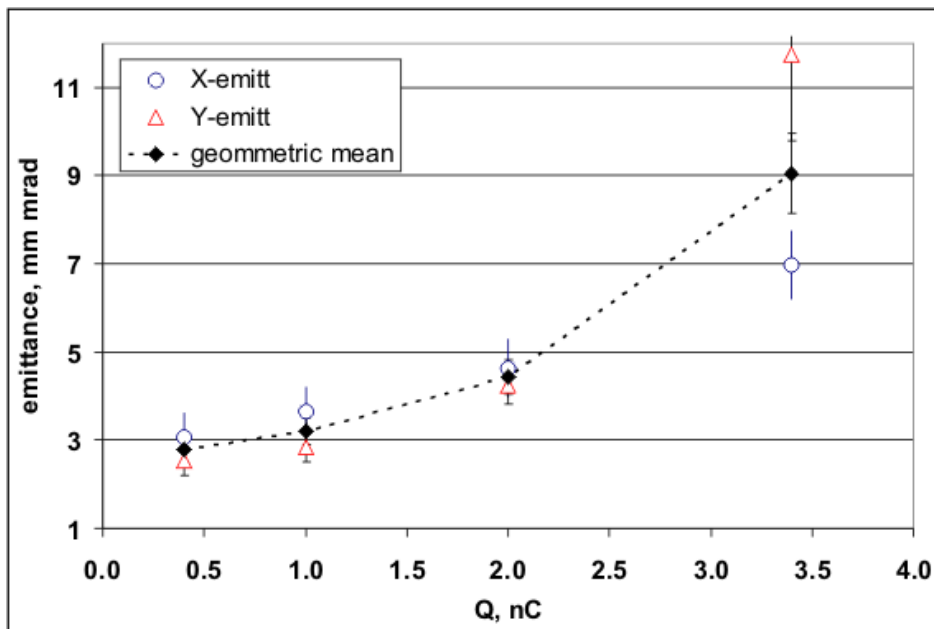


Figure 5.38: Measured geometric mean emittance $\sqrt{\epsilon_x \epsilon_y}$ and a best fit ϵ_{fit} , based on the model in Eq. 5.30, are shown together with the first derivative $d\epsilon_{fit}/dQ$.

bunch charge have been done at a fixed laser spot size and a constant laser pulse length. This means that a charge scaling of the injector parameters has not been done. For a complete study of the dependence of the minimum emittance on the bunch charge one should scale all gun parameters[71] and only then one can draw a conclusion which is the optimum charge for a certain application.



(a) $\Phi - \Phi_m = 0^\circ$.

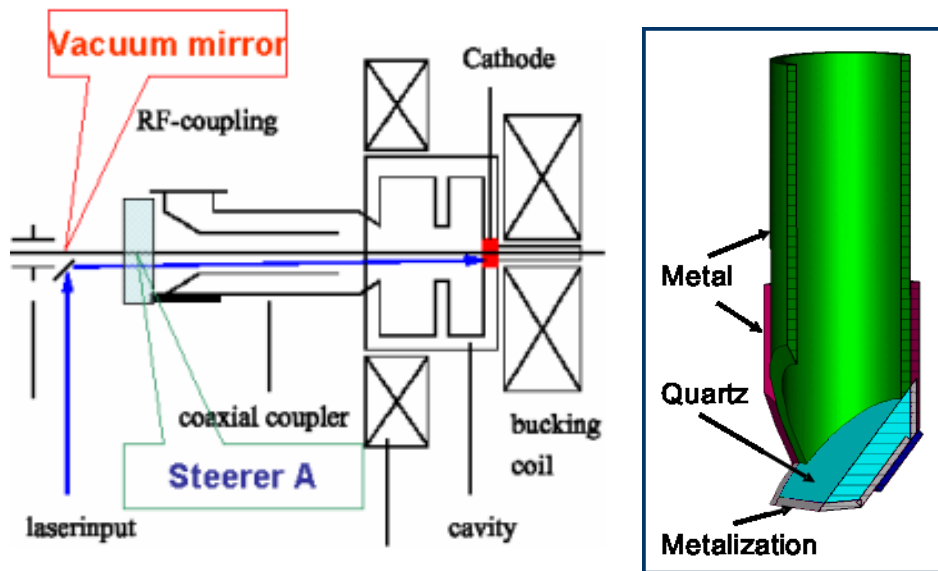


(b) $\Phi - \Phi_m = -5^\circ$.

Figure 5.39: Transverse emittance as a function of the bunch charge for different rf phases. The solenoid current was tuned to minimize the projected emittance.

5.5 Influence of the in-vacuum components

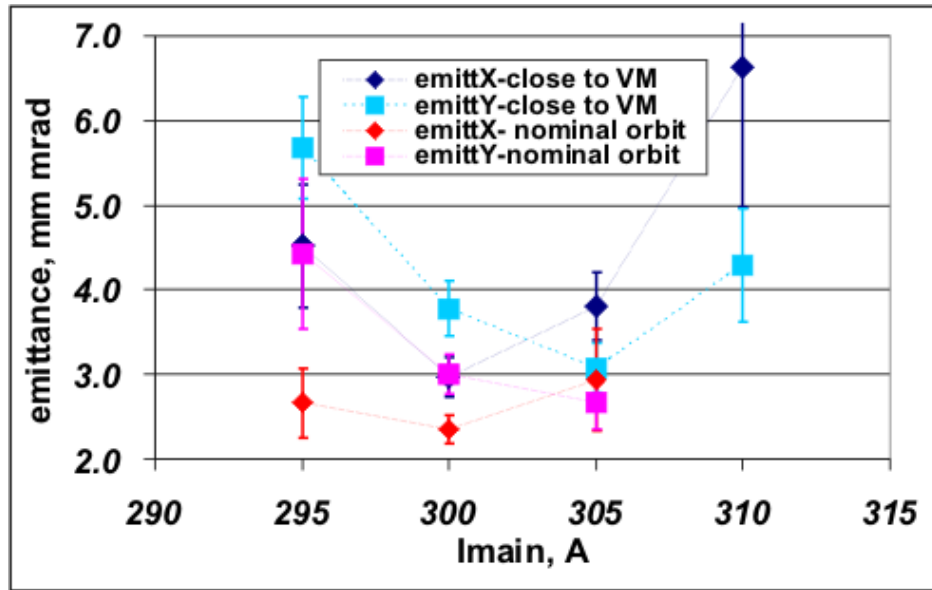
The PITZ experience shows that the impact of the vacuum components on the beam emittance should be studied and must be in the list of optimization items. According to the hardware installation at PITZ the driving laser beam is inserted into the vacuum pipe through a quartz window and then it is reflected towards the photo cathode on a mirror mounted inside the vacuum system - the so called vacuum mirror (VM) as depicted in Fig 5.40. During the injector operation it was observed that when the electron beam passes close to VM the beam shape changes and the transverse beam emittance increases. In order to quantify the emittance growth induced by the VM a series of emittance measurements have been done for various electron beam offsets relative to the VM. In Fig. 5.41(a), two solenoid scans are presented - for the first set of measurements, the electron beam has been horizontally shifted with respect to its design orbit i.e. the beam has been steered about 6 mm closer to the laser vacuum mirror than the nominal distance of 12 mm. This metallized glass mirror is being charged up by the beam and dark current and the resulting electromagnetic fields affect the beam quality. As demonstrated in the second set of measurements, an emittance reduction of 0.5 to 1.0 mm mrad was achieved by steering the beam away from the vacuum mirror. A detailed simulation study of this phenomena [73] agrees well with the presented measurements. An additional set of measurements was performed by scanning the current through the steerer A and keeping all the other operation parameters fixed. The results are shown in Fig. 5.41(b). The horizontal emittance depends more strongly than the vertical one on the distance to the mirror because the beam offset to the VM changes in x-direction by varying the steerer current. One has to note another important feature of this steerer scan: the emittance does not decrease monotonically with the distance to the vacuum mirror, but has a certain minimum at about 2.5 A. This approximately corresponds to the nominal beam orbit, since the mounting tolerances lead to an offset of VM. If one increases the steering current more it drives the electrons closer to the opposite side of the vacuum pipe and wake fields increase the beam emittance.



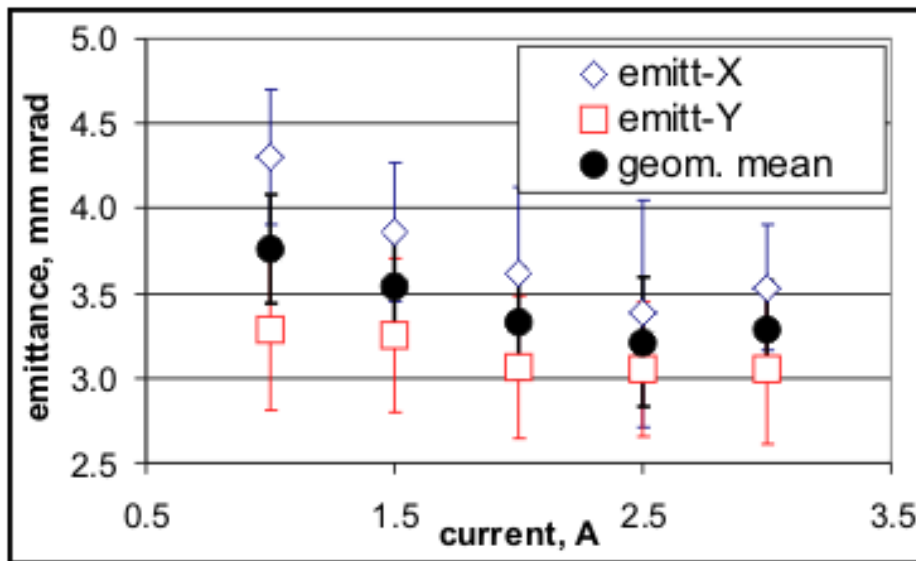
(a) The incoming UV laser beam is reflected towards the photo cathode on the vacuum mirror (VM). The steerer A has been used to control the electron beam offset with respect to VM

(b) MicroWave studio model of the vacuum mirror (courtesy of S. Setzer et. al. [73])

Figure 5.40: A schematic layout of the surroundings of the vacuum mirror is depicted in (a) and a sketch of the VM itself is shown in (b)



(a) Measurements with cavity prototype №2 demonstrating the impact of the laser vacuum mirror (VM) on the emittance. The bunch charge is 1.0 nC, the gun phase $\Phi - \Phi_m = -5^\circ$.



(b) Transverse emittance as a function of the current through a steerer magnet, measured with cavity prototype №1. A current of 1 A corresponds to a beam trajectory closer to VM and 3 A to a maximal distance. The bunch charge is 1.0 nC, the gun phase $\Phi - \Phi_m = 0^\circ$.

Figure 5.41: Measurements demonstrating the influence of the vacuum components on the transverse emittance. The photoinjector operation parameters are not yet optimized for minimum emittance

Summary

Transverse emittance studies were performed for various temporal profiles of the UV laser pulse. The pulses of flat top temporal profile generate about a factor of two smaller transverse emittance compared to the gaussian shape. A systematic measurement program was carried out in order to determine the optimal operation conditions of the photoinjector. The optimization strategy takes into account a number of injector parameters like rf phase, main and bucking solenoid current and laser spot size at the cathode. Two cavity prototypes were fully characterized - cavity №2, which was afterwards installed at the VUV-FEL at DESY in Hamburg and cavity №1. The optimum operation conditions for the two guns are summarized in Table 5.2. The

Table 5.2: Experimentally optimized parameter set for obtaining minimum emittance with gun cavity №1 and №2.

gun.№	E [MV/m]	σ_x, σ_y [mm]	I _{main} [A]	I _{buck} [A]	$\Phi - \Phi_m$ [°]	$\sqrt{\epsilon_x \epsilon_y}$ [μm]
1	45	0.57,0.59	324	24	-7	1.5
2	42	0.52,0.60	305	20	-5	1.7

correlation between the currents of the bucking and the main solenoid, which is required to compensate the magnetic field at the photocathode position and respectively to minimize the magnetic emittance has been determined by the means of a He-Ne alignment laser. During the rf gun optimization it turned out that the in-vacuum laser mirror has a significant impact on the electron beam quality due to mirror charging and wakefields generation. It was found that by steering the electron beam away from the internal mirror an emittance reduction of about 0.5-1.0 mm mrad was reached.

The thermal emittance studies were carried out for a very low charge of 2-3 pC, short laser pulses of σ_t about 3 ps and moderate accelerating gradients. According to simulations the space charge and rf field contributions to the emittance should be less than 5% at these operation conditions. The scaling of the thermal emittance with the laser spot rms size was investigated using

the single slit scanning technique as well as the solenoid scan method. The measurements were repeated with different cathodes.

The average kinetic energy of the emitted photoelectrons was estimated to be in the range 4.2-4.4 eV above the top of the valence band of the Cs₂Te photocathode, which corresponds to 0.9-1.1 eV relative to the vacuum level. The thermal emittance was measured as a function of the applied field at the cathode, where monotonic increase with electric field due to the Schottky effect was observed. The electron affinity at zero accelerating field was estimated to be 0.45 ± 0.10 eV for a cathode with QE of about 3%.

Conclusions and Outlook

The production of small emittance electron beams can be achieved only after extensive experimental studies to determine the optimum operation parameters. The numerical simulations and the analytical estimations give a very good hint in which parameter range one should search.

In order to further improve the beam quality towards the generation of ultra low emittance (<1 mm mrad) electron beams the following points have to be considered:

- Reduction of the rise/fall time r_t of the UV laser pulse. The final goal should be $r_t < 2$ ps [39].
- Increase of the gun gradient. After gun conditioning and with the available 10 MW klystron a gradient of about 60 MV/m should be possible.
- After the installation of a booster cavity, study the emittance evolution along the beamline.
- Studies on photocathode materials, cathode laser and emission process in order to minimize the thermal emittance.

Appendix A

Magnetic emittance formula

According to Busch's theorem[66], a particle emitted from a cathode region with nonzero longitudinal magnetic field B_z obtains a residual angular momentum p_θ proportional to the magnetic flux Ψ enclosed in a circle of radius r , where r is the particle's radial coordinate (considering a cylindrical coordinate system (r, θ, z) referenced to the beam axis). The residual angular momentum is then given by:

$$p_\theta = \gamma m_0 r v_\theta = \frac{e\Psi}{2\pi} = \frac{eB_z r^2}{2} \quad (5.32)$$

The horizontal velocity v_x is determined by the azimuthal velocity v_θ :

$$v_x = v_\theta \sin \theta = \frac{eB_z r}{2\gamma m_0} \sin \theta \quad (5.33)$$

then the horizontal momentum is given by:

$$p_x = \frac{eB_z r}{2} \sin \theta = \frac{eB_z}{2} y \quad (5.34)$$

Then the rms momentum $\sqrt{\langle p_x^2 \rangle}$ will be

$$\sqrt{\langle p_x^2 \rangle} = \frac{eB_z}{2} \sqrt{\langle y^2 \rangle} = \frac{eB_z}{2} \sigma_y \quad (5.35)$$

where σ_y is beam's vertical rms size. The normalized magnetic emittance is given by:

$$\epsilon_{magn} = \frac{1}{m_0 c} \sqrt{\langle x^2 \rangle \langle p_x^2 \rangle - \langle x p_x \rangle^2} \quad (5.36)$$

Since there is no correlation in phase space at the cathode i.e.

$$\langle x p_x \rangle = 0 \quad (5.37)$$

the magnetic emittance ϵ_{magn} is:

$$\epsilon_{magn} = \frac{e}{2m_0 c} B_z \sigma_x \sigma_y \quad (5.38)$$

Appendix B

Operation conditions for the characterization of gun cavity №2

For the points $\{I_{\text{main}}^*, \Phi^*\}$, an additional tuning with the compensating solenoid current I_{buck} was performed. Φ_m denotes the rf phase with maximal mean energy gain.

Table 5.3: Parameter set for the phase space study for $D=0.9$ mm

$D[\text{mm}]$	$\sigma_x, \sigma_y[\text{mm}]$	$\Phi - \Phi_m[^\circ]$	$I_{\text{main}}[\text{A}]$					$\beta\gamma$
0.9	0.43, 0.49	-10	295	300	305	310	315	9.20
		-5*	295	300*	305*	310*	315	9.22
		0*	295	300	305*	310	—	9.25
		+5	295	300	305	310	—	9.23
		+10	295	300	305	—	—	9.14

Table 5.4: Parameter set for the phase space study for $D=1.0$ mm

$D[\text{mm}]$	$\sigma_x, \sigma_y[\text{mm}]$	$\Phi - \Phi_m[^\circ]$	$I_{\text{main}}[\text{A}]$					$\beta\gamma$
1.0	0.48, 0.54	-5	295	300	305	310	—	9.21
		0	295	300	305	310	—	9.26

Table 5.5: Parameter set for the phase space study for $D=1.2$ mm

$D[\text{mm}]$	$\sigma_x, \sigma_y[\text{mm}]$	$\Phi - \Phi_m[^\circ]$	$I_{\text{main}}[\text{A}]$					$\beta\gamma$
1.2	0.51, 0.62	-15	295	300	305	—	—	9.13
		-10	295	300	305	310	—	9.17
		-5*	295*	300*	305*	310	—	9.21
		0*	295	300*	305*	—	—	9.22
		+5	295	300	305	—	—	9.21

Operation conditions for the characterization of gun cavity №1

Table 5.6: Parameter set for the phase space study for $D=1.2$ mm

D [mm]	σ_x, σ_y [mm]	$\Phi - \Phi_m$ [°]	I_{main} [A]					$\beta\gamma$
1.2	0.45, 0.47	-10	311	316	321	326	331	10.08
		-5	315	320	323	325	327	10.15
			330	332				
		0	315	320	325	330	335	10.16
+5	315	320	325	330	335	10.15		

Table 5.7: Parameter set for the phase space study for $D=1.5$ mm

D [mm]	σ_x, σ_y [mm]	$\Phi - \Phi_m$ [°]	I_{main} [A]			$\beta\gamma$
1.5	0.57, 0.59	-10	311	316	321	10.10
			325-327	331	336	
		-9	320	322	324	10.12
			326	328		
		-7*	322	324*	330	10.14
			326	328		
		-5*	310-311	315	316	10.17
320-324*	325		326*-332			
-3	322	324	326	10.18		
	328	330				
0	310-311	315-317	320-328	10.18		
	330-332	335-336				
5	311,315,316	320	321	10.16		
	325	326	330, 331			

Table 5.8: Parameter set for the phase space study for $D=1.8$ mm

D [mm]	σ_x, σ_y [mm]	$\Phi - \Phi_m$ [$^\circ$]	I_{main} [A]			$\beta\gamma$
1.8	0.67, 0.69	-5	321,322 326	324 327	325	10.16
		0	311,316 324,326,	317, 321 327	322 331,336	10.18
		5	311,316 324,326	317,321 328, 331	322 336	10.13
		10	311,316	326	331	10.04

Bibliography

- [1] F. R. Elder et. al. Radiation from Electrons in a Synchrotron. *Physical Review*, 71:829–830, 1947.
- [2] LCLS Conceptual Design Report. SLAC-R-593, SLAC, 2002.
- [3] R. Brinkmann. Accelerator layout of the XFEL. In *Proceedings Linear Accelerator Conference*, 16-20 August, 2004, Lübeck, Germany.
- [4] F. Stephan et al. Photo Injector Test Facility under construction at DESY Zeuthen. In *Proceedings Free Electron Laser Conference*, 13-18 Aug. 2000, Durham, North Carolina.
- [5] F. Stephan et al. Recent results and perspectives of the low emittance photo injector at PITZ. In *Proceedings Free Electron Laser Conference*, 29 Aug-3 Sep., 2004, Trieste, Italy.
- [6] D. Lipka. *Untersuchungen zum longitudinalen Phasenraum an einem Photoinjector für minimale Strahlemittanz*. PhD thesis, HUB, 2004.
- [7] J. Roensch et. al. Measurement of the Longitudinal Phase Space at the Photo Injector Test Facility at DESY in Zeuthen (PITZ). In *Proceedings Beam Diagnostics and Instrumentation for Particle Accelerators Conference*, 6 - 8 June, 2005, Lyon, France.
- [8] I. Will et al. A laser system for the TESLA photon collider based on an external ring resonator. *NIM*, A 472:79–85, 2001.
- [9] I. Will et al. The upgraded photocathode laser of the TESLA Test Facility. *NIM*, A 541:467–477, 2005.
- [10] I. Will. Spitzentechnologie für TESLA: Hochleistungslaser. TESLA-Licht der Zukunft, Tag der Wissenschaft, 2002.
- [11] J. P. Carneiro et. al. Behavior of the TTF2 RF Gun with long pulses and high repetition rates. TESLA-note, DESY, 2004.

-
- [12] K. Flöttmann. RF gun design for the TESLA VUV Free Electron Laser. *Nuclear Instruments and Methods*, A 393:93–95, 1997.
- [13] S. Schreiber et al. Commissioning of the VUV-FEL Injector at TTF. In *Proceedings European Particle Accelerator Conference*, 5-9 July, 2004, Luzern, Switzerland.
- [14] M. Reiser. *Theory and design of charged particle beams*. John Wiley and sons, New York, 1994.
- [15] K. Flöttmann. A Space Charge Tracking Algorithm. <http://www.desy.de/~mpyflo/>.
- [16] M. E. Hernandez. *Four dimensional trace space measurement*. PhD thesis, Stanford University, 2003.
- [17] J. Buon. Beam phase space and emittance. CERN 94-01, CERN, 1992.
- [18] J. Rosenzweig. *Fundamentals of beam physics*. Oxford, New York, 2003.
- [19] Kwang-Je Kim. RF and space charge effects if laser driven rf electron guns. *Nuclear Instruments and Methods*, A275:201–218, 1989.
- [20] E. R. Colby. *Design, Construction, and Testing of a Radiofrequency Electron Photoinjector, for the Next Generation Linear Collider*. PhD thesis, University of California Los Angeles, 1997.
- [21] B. E. Carlsten. New Photoelectric Injector Design for the Los Alamos XUV FEL Accelerator. *Nuclear Instruments and Methods*, A285:313–319, 1989.
- [22] D. C. Carey et. al. Third-Order TRANSPORT with MAD Input. A Computer Program for Designing Charged Particle Beam Transport Systems. SLAC-R-530, SLAC, 1998.
- [23] C. Limborg. A Modified Quadscan Technique for Emittance Measurement of Space Charge Dominated Beams. In *Proceedings Particle Accelerator Conference*, May, 2003, Portland, USA.
- [24] K. Allen et. al. Theory and technique of beam envelope simulation. LA-UR-02-4979, LANL, 2002.
- [25] K. Flöttmann. Some basic features of the beam emittance. *Phys. Rev. ST Accel. Beams*, 6, 2003.

- [26] K. Flöttmann. Pepper pot Design for Space Charge Dominated High Brightness Beams. TESLA-FEL 96-09, DESY, 1996.
- [27] Ph. Piot. Zeroth-order considerations for a single slit-based Emittance diagnostics at the PITZ facility, 2000.
- [28] Newport Corporation. Newport Resource catalogue, 2002.
- [29] J. Rosenzweig et. al. Design Considerations for the UCLA PBPL Slit-based Phase Space Measurement Systems, 1994.
- [30] J. Bähr et al. The Diagnostics System for the Photoinjector Test Facility at DESY Zeuthen. In *Proceedings European Particle Accelerator Conference*, 3-7 June, 2002, Paris, France.
- [31] V. Miltchev et al. Transverse Emittance Measurements at the Photo Injector Test Facility at DESY Zeuthen (PITZ). In *Proceedings Beam Diagnostics and Instrumentation for Particle Accelerators Conference*, 5-7 May, 2004, Mainz, Germany.
- [32] J. D. Lawson. *The Physics of Charge-Particle Beams*. Clarendon Press, Oxford, 1988.
- [33] Klaus Flöttmann. Note on the Thermal Emittance of Electrons Emitted by Cesium Telluride Photo Cathodes. TESLA-FEL report 1997-01, DESY, 1997.
- [34] P. Michelato et al. Thermal emittance estimation using a time-of-flight spectrometer. In *Proceedings European Particle Accelerator Conference*, 26-30 June, 2000, Vienna, Austria.
- [35] W. S. Graves et al. Measurement of thermal emittance for a copper photocathode. In *Proceedings Particle Accelerator Conference*, 18-22 June, 2001, Chicago, U.S.A.
- [36] D. Sertore et al. Cesium Telluride and Metals Photoelectron Thermal Emittance Measurements Using a Time-of-flight Spectrometer. In *Proceedings European Particle Accelerator Conference*, 5-9 July, 2004, Lucerne, Switzerland.
- [37] J. E. Clendenin et. al. Reduction of thermal emittance of rf guns. SLAC-PUB-8284, SLAC, 1999.

- [38] Z. Yusof et. al. Schottky-Enabled Photoemission in a rf Accelerator Photoinjector: Possible Generation of Ultralow Transverse Thermal-Emittance Electron Beam. *Physical Review Letters*, 93:114801–114801–4, 2004.
- [39] M. Ferrario et al. Conceptual Design of the XFEL Photoinjector. TESLA-FEL note, 2001-03, DESY, 2001.
- [40] W. E. Spicer. Photoemissive, Photoconductive, and Optical Absorption Studies of Alkali-Antimony Compounds. *Physical Review*, 112:114–122, 1958.
- [41] R. A. Powel et. al. Photoemission Studies of Cesium Telluride. *Phys. Rev. B*, 8:3987–3995, 1973.
- [42] H. Trautner. *Spectral Response of Cesium Telluride and Rubidium Telluride Photocathodes for the Production of Highly Charged Electron Bunches*. PhD thesis, Johannes Gutenberg - Universität in Mainz.
- [43] J-H. Han et al. Conditioning and high power test of the rf guns at PITZ. In *Proceedings European Particle Accelerator Conference*, 5-9 July, 2004, Lucerne, Switzerland.
- [44] J.W. Wang. RF Properties of Periodic Accelerating Structures for Linear Colliders. SLAC-Report-339, SLAC, 1989.
- [45] R. Bossart et. al. A 3 GHz gun for high beam intensity. CLIC-Note-297, CERN, 1995.
- [46] G. Suberlucq. Development and Production of Photo Cathodes for the CLIC Test Facility. In *Proceedings Free Electron Laser Conference*, August, 1996, Rome, Italy.
- [47] S. M. Sze. *Physics of semiconductor devices*. John Willey, New York, 1981.
- [48] A. Buzulutskov et. al. Field enhancement of the photoelectric and secondary electron emission from CsI. *Journal Applied Physics*, 77:2138–2145, 1995.
- [49] J-H. Han et al. Emission mechanisms in a photocathode rf gun. In *Proceedings Particle Accelerator Conference*, 16-20 May, 2005, Knoxville, Tennessee, U.S.A.

- [50] C. I. Coleman. Field-enhancement of photoemission from cesium telluride. *Applied Optics*, 17:1789–1796, 1978.
- [51] P. Michelato. Photocathodes for RF photoinjectors. *Nuclear Instruments and Methods, A* 393:455–459, 1997.
- [52] N. Horing R. Enderlein. *Fundamentals of Semiconductor Physics and Devices*. World Scientific, Singapore, 1997.
- [53] J. Rosenzweig L. Serafini. Envelope analysis of intense relativistic quasilaminar beams in rf photoinjectors: A theory of emittance compensation. *Physical Review E*, 55:7565–7590, 1997.
- [54] J. Yang. Experimental studies of photocathode rf gun with laser pulse shaping, 2002. Sumitomo heavy industries and Femtosecond research association.
- [55] E. Jones et. al. Space charge induced emittance growth in the transport of high brightness electron beams. In *Proceedings Particle Accelerator Conference*, 16-19 March 1987, Washington, U.S.A.
- [56] D. A. Reis. *Emittance measurements from a laser driven electron injector*. PhD thesis, Stanford University, 1999.
- [57] V. Miltchev et al. Transverse emittance measurements at the photo injector test facility at DESY Zeuthen. In *Proceedings Free Electron Laser Conference*, 29 Aug-3 Sep., 2004, Trieste, Italy.
- [58] I. Bohnet et. al. Magnetic Field Investigations of the Solenoid Arrangement for PITZ. PITZ-note, 08 October, DESY, 2002.
- [59] M. Krasilnikov. Beam-Based Procedures for RF Gun. In *Proceedings Particle Accelerator Conference*, May 16-20, 2005, Knoxville, Tennessee, USA.
- [60] S. Schreiber et. al. Measurement of Space Charge Effects and Laser Pulse Length in the TTF RF Gun using the Phase Scan Technique. In *Proceedings Free Electron Laser Conference*, August 23-28, 1999 Hamburg, Germany.
- [61] M. Krasilnikov et al. Optimizing the PITZ electron source for the VUV-FEL. In *Proceedings European Particle Accelerator Conference*, 5-9 July, 2004, Luzern, Switzerland.

-
- [62] F. Zhou et. al. Experimental characterization of emittance growth induced by the nonuniform transverse laser distribution in a photoinjector. *Physical Review Special Topics - Accelerators and beams*, 5, 2002.
- [63] J. Bähr et al. High power rf conditioning and measurement of longitudinal emittance at PITZ. In *Proceedings Free Electron Laser Conference*, 29 Aug-3 Sep., 2004, Trieste, Italy.
- [64] L. Staykov et. al. Solenoid measurements at the Photo Injector Test Facility at DESY Zeuthen. PITZ-note, DESY, 2005.
- [65] M. Krasilnikov et al. Characterization of the Electron Source at the Photo Injector Test Facility at DESY Zeuthen. In *Proceedings Free Electron Laser Conference*, Sept, 2003, Tsukuba, Japan.
- [66] Jr. Stanley Humphries. *Principles of Charged Particle Acceleration*. John Wiley and sons, New York, 1999.
- [67] Y.-E Sun et al. Generation of angular-momentum-dominated electron beams from a photoinjector. *Phys. Rev. ST Accel. Beams*, 7, 2004.
- [68] J. Rossbach. LINAC based Free-Electron Laser. TESLA-FEL report 2004-08, DESY, 2004.
- [69] S. Reiche. Compensation of FEL gain reduction by emittance effects in a strong focussing lattice. In *Proceedings Free Electron Laser Conference*, August 23-28, 1999 Hamburg, Germany.
- [70] J. Rosenzweig et. al. Optimal scaled photoinjector designs for FEL applications. In *Proceedings Particle Accelerator Conference*, 1999, New York, U.S.A.
- [71] J. Rosenzweig et. al. Charge and wavelength scaling of rf photoinjectors: A design tool. In *Proceedings Particle Accelerator Conference*, 1995, New York, U.S.A.
- [72] D. Dowell et. al. Longitudinal Measurements at the SLAC Gun Test Facility. SLAC-PUB 9541, SLAC, 2002.
- [73] S. Setzer et al. Influence of Beam Tube Obstacles on the Emittance of the PITZ Photoinjector. In *Proceedings European Particle Accelerator Conference*, 5-9 July, 2004, Luzern, Switzerland.

Acknowledgments

I would like to thank to all my colleagues at PITZ and DESY for their help. It was a pleasure for me to work with them. I cordially thank my supervisor at PITZ Frank Stephan for his guidance and support. I specially thank Ivan Tsakov for his support in all situations. I am indebted to Klaus Flöttmann for the encouragement and for the many valuable advices. I thank Mikhail Krasilnikov for the countless stimulating discussions; Dieter Richter for the good work together and for the help with Latex. I am thankful to Philippe Piot for the discussions on the thermal emittance studies and to Jean-Paul Carneiro for many interesting discussions on emittance diagnostics. I thank Stefan Weisse for providing the image acquisition software and Karen Abrahamyan for the hard work on the motion control software. Finally, I thank again Frank, Klaus and Mikhail for the careful proof-reading of my thesis.

Erklärung

Hiermit versichere ich, die Dissertation selbstständig verfasst und ohne unerlaubte Hilfe angefertigt zu haben. Ich habe mich anderwärts nicht um einen Doktorgrad beworben und besitze einen entsprechenden Doktorgrad nicht. Ich erkläre die Kenntnisnahme der dem Verfahren zugrunde liegenden Promotionsordnung der Mathematisch-Naturwissenschaftlichen Fakultät I der Humboldt-Universität zu Berlin an.

Velizar Miltchev, den 4.5.2006